JSCSEN 91(2)99-212(2026)

ISSN 1820-7421(Online)

Journal of the Serbian Chemical Society

Electronic version

VOLUME 91

No 2

BELGRADE 2026

Available on line at

www.shd.org.rs/JSCS/

The full search of JSCS is available through

DOAJ DIRECTORY OF OPEN ACCESS JOURNALS

www.doaj.org

The **Journal of the Serbian Chemical Society** (formerly Glasnik Hemijskog društva Beograd), one volume (12 issues) per year, publishes articles from the fields of chemistry. The **Journal** is financially supported by the **Ministry of Education, Science and Technological Development of the Republic of Serbia.**
Articles published in the **Journal** are indexed in **Clarivate Analytics products: Science Citation Index-Expanded™** – accessed *via* **Web of Science®** and **Journal Citation Reports®**.
Impact Factor announced for the year 2024: **0.700; 5-year Impact Factor**: **0.900**.
Articles appearing in the **Journal** are also abstracted by: **Scopus, Chemical Abstracts Plus (CAplus℠), Directory of Open Access Journals, Referativnii Zhurnal (VINITI), RSC Analytical Abstracts, EuroPub, Pro Quest** and **Asian Digital Library.**

Publisher:	**Serbian Chemical Society**, Karnegijeva 4/III, P. O. Box 36, 1120 Belgrade 35, Serbia tel./fax: +381–11–3370–467, E-mails: **Society** – shd@shd.org.rs; **Journal** – jscs@shd.org.rs Home Pages: **Society** – http://www.shd.org.rs/, **Journal** – http://www.shd.org.rs/JSCS/
Internet Service:	Contents, Abstracts and full papers (from Vol. 64, No. 1, 1999) are available in the electronic form at the Web Site of the **Journal** (http://www.shd.org.rs/JSCS/).
Former Editors:	**Nikola A. Pušin** (1930–1947), **Aleksandar M. Leko** (1948–1954), **Panta S. Tutundžić** (1955**–**1961), **Miloš K. Mladenović** (1962–1964), **Đorđe M. Dimitrijević** (1965–1969), **Aleksandar R. Despić** (1969–1975), **Slobodan V. Ribnikar** (1975–1985), **Dragutin M. Dražić** (1986–2006).
Editor-in-Chief:	BRANISLAV Ž. **NIKOLIĆ**, Serbian Chemical Society (E-mail: jscs-ed@shd.org.rs)
Deputy Editor:	DUŠAN **SLADIĆ**, Faculty of Chemistry, University of Belgrade
Sub editors:	
Organic Chemistry	DEJAN **OPSENICA**, Institute of Chemistry, Technology and Metallurgy, University of Belgrade JÁNOS **CSANÁDI**, Faculty of Science, University of Novi Sad
Biochemistry and Biotechnology	OLGICA **NEDIĆ**, INEP – Institute for the Application of Nuclear Energy, University of Belgrade
Inorganic Chemistry	BILJANA **GLIŠIĆ**, Faculty of Science, University of Kragujevac
Theoretical Chemistry	MATIJA **ZLATAR**, Institute of Chemistry, Technology and Metallurgy, University of Belgrade MILOŠ **MILIČIĆ**, Faculty of Chemistry, University of Belgrade
Physical Chemistry	LJILJANA **DAMJANOVIĆ-VASILIĆ**, Faculty of Physical Chemistry, University of Belgrade
Electrochemistry	SNEŽANA **GOJKOVIĆ**, Faculty of Technology and Metallurgy, University of Belgrade
Analytical Chemistry	RADA **BAOŠIĆ**, Faculty of Chemistry, University of Belgrade
Polymers	BRANKO **DUNJIĆ**, Faculty of Technology and Metallurgy, University of Belgrade
Thermodynamics	MIRJANA **KIJEVČANIN**, Faculty of Technology and Metallurgy, University of Belgrade
Chemical Engineering	TATJANA **KALUĐEROVIĆ RADOIČIĆ**, Faculty of Technology and Metallurgy, University of Belgrade
Materials	RADA **PETROVIĆ**, Faculty of Technology and Metallurgy, University of Belgrade
Metallic Materials and Metallurgy	ANA **KOSTOV**, Mining and Metallurgy Institute Bor, University of Belgrade
Environmental and Geochemistry	VESNA **ANTIĆ**, Faculty of Agriculture, University of Belgrade
History of and Education in Chemistry	DRAGICA **TRIVIĆ**, Faculty of Chemistry, University of Belgrade
English Language Editors:	VLATKA **VAJS**, Serbian Chemical Society MIROSLAV **PAVLOVIĆ**, Institute of Chemistry, Technology and Metallurgy, University of Belgrade
Technical Editors:	VLADIMIR **PANIĆ**, Institute of Chemistry, Technology and Metallurgy, University of Belgrade, MARIO **ZLATOVIĆ**, Faculty of Chemistry, University of Belgrade
Journal Manager & Web Master:	MARIO **ZLATOVIĆ**, Faculty of Chemistry, University of Belgrade
Office:	VERA **ĆUŠIĆ**, Serbian Chemical Society

Editorial Board
From abroad: **R. Adžić**, Brookhaven National Laboratory (USA); **A. Casini**, University of Groningen (The Netherlands); **G. Cobb**, Baylor University (USA); **D. Douglas**, University of British Columbia (Canada); **G. Inzelt**, Etvos Lorand University (Hungary); **J. Kenny**, University of Perugia (Italy); **Ya. I. Korenman**, Voronezh Academy of Technology (Russian Federation); **M. D. Lechner**, University of Osnabrueck (Germany); **S. Macura**, Mayo Clinic (USA); **M. Spiteller**, INFU, Technical University Dortmund (Germany); **M. Stratakis**, University of Crete (Grecce); **M. Swart**, University de Girona (Cataluna, Spain); **G. Vunjak-Novaković**, Columbia University (USA); **P. Worsfold**, University of Plymouth (UK); **J. Zagal**, Universidad de Santiago de Chile (Chile).
From Serbia: **B. Abramović**, **V. Antić**, **R. Baošić**, **V. Beškoski**, **J. Csanadi**, **Lj. Damjanović-Vasilić**, **A. Dekanski**, **V. Dondur**, **B. Dunjić**, **M. Đuran, B. Glišić, S. Gojković**, **I. Gutman**, **B. Jovančićević**, **I. Juranić**, **T. Kaluđerović Radiočić**, **L. Katsikas**, **M. Kijevčanin**, **A. Kostov**, **V. Leovac**, **S. Milonjić**, **V.B. Mišković-Stanković**, **O. Nedić**, **B. Nikolić**, **D. Opsenica**, **V. Panić**, **M. Pavlović**, **M. Petkovska**, **R. Petrović**, **I. Popović**, **B. Radak**, **S. Ražić**, **D. Sladić**, **S. Sovilj**, **S. Šerbanović**, **B. Šolaja**, **Ž. Tešić**, **D. Trivić**, **V. Vajs, M. Zlatović**.

Subscription: The annual subscription rate is **150.00 €** including postage (surface mail) and handling. For Society members from abroad rate is **50.00 €**. For the proforma invoice with the instruction for bank payment contact the Society Office (E-mail: shd@shd.org.rs) or see JSCS Web Site: http://www.shd.org.rs/JSCS/, option Subscription.
Godišnja pretplata: Za članove SHD: **2.500,00 RSD**, za penzionere i studente: **1000,00 RSD**, a za ostale: **3.500,00 RSD**:za organizacije i ustanove: **16.000,00 RSD**. Uplate se vrše na tekući račun Društva: **205-13815-62**, poziv na broj **320**, sa naznakom "pretplata za JSCS".

Nota: Radovi čiji su svi autori članovi SHD prioritetno se publikuju.
Odlukom Odbora za hemiju Republičkog fonda za nauku Srbije, br. 66788/1 od 22.11.1990. godine, koja je kasnije potvrđena odlukom Saveta Fonda, časopis je uvršten u kategoriju međunarodnih časopisa (**M-23**). Takođe, aktom Ministarstva za nauku i tehnologiju Republike Srbije, 413-00-247/2000-01 od 15.06.2000. godine, ovaj časopis je proglašen za publikaciju od posebnog interesa za nauku. **Impact Factor** časopisa objavljen za 2024. godinu je **0,700**, a petogodišnji **Impact Factor 0,900**.

Journal of the Serbian Chemical Society
JSCS-info@shd.org.rs • www.shd.org.rs/JSCS

J. Serb. Chem. Soc. Vol. 91, No. 2 (2026)

CONTENTS*

Biochemistry and Bioengineering

G. T. Đelić, *M. B. Pavlović*, *Z. B. Simić*, *J. M. Tubić Vukajlović*, *D. V. Grujičić*, *M. Z. Radović Jakovljević* and *O. M. Milošević-Đorđević*: The accumulation of metals in *Onobrychis viciifolia* Scop., their distribution in plant parts and the impact on the content of phenols and flavonoids, as well as antioxidant and genotoxic activity. 99

Inorganic Chemistry

A. Tavman, *D. Gurbuz*, *M. Hacioglu*, *A. Cinarli*, *O. Sahin* and *A. S. Birteksoz Tan*: Spectral characterization and antimicrobial activity studies of 5,6-dichloro-1*H*-benzimidazol-2-yl-(4'/5'/6'-substituted)-phenols (**HL$_1$**–**HL$_{20}$**) and Co(II), Ni(II), Cu(II), Zn(II) and Pd(II) complexes of **HL$_1$** 113

Theoretical Chemistry

A. M. Đurđević Đelmaš, *D. P. Trajković*, *K. Milčić* and *M. K. Milčić*: Molecular dynamics-based methodological approach to clarify perfluorooctanoic acid binding on human serum albumin 129

Electrohemistry

E. Keskin, *M. Kiran* and *Y. Yardim*: A simple and feasible determination of the selective estrogen receptor modulator raloxifene in pharmaceutical formulation using pretreated boron-doped diamond electrode 145

Polymers

H. Sebaihi, *W. Bensalah*, *K. Badis* and *M. Haouaria*: A comparative study of ketoprofen-loaded microparticles prepared using emulsion-congealing and solvent evaporation techniques 161

Materials

N. Akter, *Md. R. Repon*, *A. D. Pranta*, *Md. Ruhul Amin*, *N. Yunusov* and *S. M. Otajonov*: Exploring the distinct physico-mechanical characteristics of bio-polymer based chambray fabric 181

Environmental

N. T. Vu, *A. P. Nguyen*, *H. S. Nguyen*, *V. A. Pham*, *D. T. Vu* and *Q. M. Le*: Composite materials based on biochar from coffee husk origin and nano zero-valent type Fe/Cu: Potential for treatment of water sources contaminated with As(V)..... 195

Published by the Serbian Chemical Society
Karnegijeva 4/III, P.O. Box 36, 11120 Belgrade, Serbia
Printed by the Faculty of Technology and Metallurgy
Karnegijeva 4, P.O. Box 35-03, 11120 Belgrade, Serbia

* For colored figures in this issue please see electronic version at the Journal Home Page: http://www.shd.org.rs/JSCS/

Journal of the Serbian Chemical Society
JSCS@tmf.bg.ac.rs • www.shd.org.rs/JSCS
J. Serb. Chem. Soc. *91* (2) 99–112 (2026)
JSCS–5480
Original scientific paper
Published 12 February, 2026

The accumulation of metals in *Onobrychis viciifolia* Scop., their distribution in plant parts and the impact on the content of phenols and flavonoids, as well as antioxidant and genotoxic activity

GORICA T. ĐELIĆ[1], MILICA B. PAVLOVIĆ[1], ZORAN B. SIMIĆ[2], JOVANA M. TUBIĆ VUKAJLOVIĆ[1], DARKO V. GRUJIČIĆ[1], MARINA Z. RADOVIĆ JAKOVLJEVIĆ[1]* and OLIVERA M. MILOŠEVIĆ-ĐORĐEVIĆ[1,3]

[1]*University of Kragujevac, Faculty of Science, Department of Biology and Ecology, Radoja Domanovica 12, Kragujevac, Serbia,* [2]*University of Kragujevac, Faculty of Science, Department of Chemistry, Radoja Domanovica 12, Kragujevac, Serbia and* [3]*University of Kragujevac, Faculty of Medical Sciences, Department of Genetics, Svetozara Markovića 69, Kragujevac, Serbia*

(Received 27 August, revised 16 October, accepted 3 December 2025)

Abstract: This research investigated the potentially toxic elements (PTE) content and biological activities of *Onobrychis viciifolia* Scop. collected from a tailing site and an uncontaminated locality. Concentrations of Mn, Ni, Ca, Mg, Fe, Zn, Cr, Pb, and Cu were determined in soil and plant parts (roots, aerial parts, and inflorescences) using the wet digestion method, followed by atomic absorption spectrophotometric analysis. Bioaccumulation (*BCF*) and translocation (*TF*) factors were calculated to assess PTE uptake and distribution. Total phenolic and flavonoid contents were determined spectrophotometrically. Antioxidant activity was evaluated using the DPPH radical scavenging assay. DNA damage in human lymphocytes treated with plant extracts was assessed using the comet assay. Results revealed significantly higher concentrations of PTE in soil and plant material from the contaminated site compared to the uncontaminated locality. Plants from the contaminated soil exhibited increased bioaccumulation and translocation of PTE. Moreover, the biological activity of the extracts, including antioxidant capacity and genotoxic effects, was influenced by the exposure of plants to PTE, which affected the synthesis of secondary metabolites. Extracts from plants growing in tailing site showed stronger activity compared to those from the uncontaminated locality. This study highlights the adaptive responses of *O. viciifolia* to PTE-induced stress and provides insights into its potential applications in environmental monitoring and phytopharmacology.

* Corresponding author. E-mail: marina.jakovljevic@pmf.kg.ac.rs
https://doi.org/10.2298/JSC250827089D

Keywords: potentially toxic elements; plant; extracts; DPPH radical scavenging assay; comet assay.

INTRODUCTION

The genus *Onobrychis* Mill. comprises about 170 species with a cosmopolitan distribution.[1] *Onobrychis viciifolia* is a perennial forage plant which characterised a high nutritional value and good quality of coarse fodder, and it is very adaptable to different climatic and soil conditions. Despite its production-quality properties, its occurrence and use in the agroecological conditions of Serbia is limited and it is mainly known as a honey-bearing species.[2] *O. viciifolia* shows tolerance to high concentrations of potentially toxic elements (PTE) in the soil and can thrive under such conditions.[3] For environmental protection, it is crucial to understand how PTE concentrations in soil can be controlled to remain below the toxicity threshold for plants.[4] Plant tolerance to PTE by exclusion involves two modes of action: preventing the uptake of metals and metalloids by limiting their passage from the soil to the root, or accumulating PTE in the root while preventing their transport to the aerial parts of the plant.[5] The uptake of PTE into the plant parts depends on the movement of PTE from the soil to the plant roots (bioconcentration factor), as well as on the transport of the elements (translocation factor) from the roots, whereby they are transported to the aerial part and inflorescences.[6] According to the literature, *O. viciifolia* has antimicrobial,[7] antibacterial,[8] anti-inflammatory,[9] antioxidant[10] and many other activities.

In the present study, the biological activities (genotoxic and antioxidant) and the total phenolic content (TPC) and total flavonoid content (TFC) were evaluated in methanolic extracts obtained from the root, inflorescence, and aerial parts of *O. viciifolia*. In addition, the concentrations of PTE (Mn, Ni, Ca, Mg, Fe, Zn, Cr, Pb, and Cu) were determined in plant tissues and in the soils collected from two locations: an uncontaminated site (Gornji Milanovac) and a tailing site (Žitkovac, Kosovska Mitrovica former Pb–Zn mining tailings).

EXPERIMENTAL

Chemicals

Gallic acid, rutin hydrate and 2,2-diphenyl-1-picrylhydrazyl (DPPH), Histopaque-1077, Roswell Park Memorial Institute (RPMI) medium, phosphate-buffered saline (PBS), Tris-HCl buffer and ethidium bromide reagent were bought from Sigma Chemicals Co. Folin–Ciocalteu phenol reagent and aluminium chloride hexahydrate were obtained from Fluka Chemie AG, Buchs, Switzerland. Low-melting-point agarose was purchased from AppliChem GmbH (Darmstadt, Germany). Triton X-100 was obtained from Fisher Scientific (Geel, Belgium). Sodium chloride, ethylenediaminetetraacetic acid (EDTA) and dimethyl sulfoxide (DMSO) were purchased from Centrohem (Stara Pazova, Serbia). Electrophoresis equipment (PowerPac Basic) was supplied by Bio-Rad (Hercules, CA, USA).

Plant material

The plants in the flowering phase and soil materials were collected from tailings at Žitkovac (tailing site), 4 km away from Kosovska Mitrovica (42.924052 N; 20.830233 E) in 2018 on 20 June and from an uncontaminated locality (Gornji Milanovac, Brusnica village, 44.002512 N; 20.432371 E) in 2020 on 30 June. Voucher specimen of *O. viciifolia* deposited in the Herbarium of the University of Kragujevac, Faculty of Science, Department of Biology and Ecology, No. 31/018.

Analysis of potentially toxic elements in samples of plant and soil

The content of PTE (manganese, nickel, calcium, magnesium, iron , zinc, chromium, lead and copper) was determined in the soil and in each plant part of *O. viciifolia* collected from both localities. Metals were analysed using the wet digestion method according to Tóth *et al.*[11], in the Laboratory for Analytical Chemistry, Faculty of Science, University of Kragujevac. For each analysis, five replicate samples (soil, roots, aerial part and inflorescence) were prepared, and the average value and standard deviation were calculated. The measurements of PTE content were carried out using an atomic absorption spectrophotometer (Perkin Elmer 3300). After the results were obtained, the bioaccumulation (BCF) and translocation factors (TF) were determined.[12] The BCF was used to determine the PTE accumulation from the soil to the roots, and the TF was used to calculate the ratio of PTE concentrations in the aerial part, inflorescence and roots.[13]

Root, aerial part and inflorescence were air-dried and 50 g of ground material from each plant part was extracted with 250 mL of methanol. After 24 h, the plant material was filtered, made up of 250 mL methanol and the extraction was repeated three times. After the extraction was completed, the extracts were evaporated in a vacuum evaporator (Soxtherm S 306, Gerhardt, Germany). The dry extract was stored at –18 °C until it was used in the tests. For testing purposes, the extract was dissolved in PBS.

Determination of total phenolic content of the extracts

The concentration of TPC in the sample's methanol solutions was determined using the spectrophotometric method (at λmax = 725 nm) by Wootton-Beard *et al.*[14] The reactant blend was made from methanolic dilutions (roots, aerial part and inflorescences), and Folin–Ciocalteu reagent and then incubated. After that, sodium carbonate was added to the mixture. Gallic acid (GA) was used to create the standard curve, which showed a linear regression $r^2 > 0.99$. The TPC is expressed in gallic acid equivalents per gram of plant extract.

Determination of flavonoid content of the extracts

The concentration of flavonoids in the methanol solutions of the samples was determined according to the spectrophotometric method (at λmax = 430 nm) of Quettier-Deleu *et al.*[15] The reagent mixture was prepared from methanolic dilutions (roots, aerial part and inflorescences), and aluminum chloride, after which they were incubated. Rutin (RU) was used to create the standard curve, which showed a linear regression $r^2 > 0.99$. The flavonoid content is expressed in rutin equivalents per gram of plant extract.

Determination of the antioxidant activity of the extracts

The free radical scavenging activity in the sample's methanol solutions was determined using the spectrophotometric method (at λmax = 517 nm) by Takao *et al.*[16] First, a dilution series of methanol solution samples was made, with concentrations of 15.62, 31.25, 62.5, 125, 250 and 500 μg/mL. The reagent mixture was prepared from diluted solutions (roots, aerial part

and inflorescences) and DPPH, which were then incubated. Ascorbic acid was used as a standard. The antioxidant activity is expressed as a concentration that inhibits 50 % of the activity (IC_{50} values in μg/mL).

Measurement of DNA damage

The whole blood was taken by venipuncture from three donors, non-smokers, priorly unexposed to any known genotoxic agents. The study was approved by the Ethics Committee of the Clinical Centre of Kragujevac (01/18/4927), before the start of the study. Written informed consent was obtained from all the patients according to the guidelines of the World Medical Association (Declaration of Helsinki).

To assess the level of DNA damage of peripheral blood lymphocytes in the treatment with different parts *O. viciifolia* plant, single-cell gel electrophoresis (comet assay) was used as described by Singh *et al.*[17] with some modifications given by Collins *et al*. [18] Lymphocytes were isolated from the whole peripheral blood using Histopague-1077 and treated for 30 min at 37 °C in phosphate buffered saline solution with methanolic extract of *O. viciifolia* root, inflorescence or aerial part at concentrations of 125, 250, 500 and 1000 μg/mL. Untreated lymphocytes were used as a negative control, while a positive control was lymphocytes treated with hydrogen peroxide at a final concentration of 10 μg/mL. The cell suspension was mixed with 1 % low-melting-point agarose for slide embedding. The slides were kept on ice for a few seconds to solidify the agarose. The coverslips were then removed and the slides were placed in a lysis solution (2.5 M NaCl, 100 mM EDTA, 10 mM Tris, 1 % Triton X-100 and 10 % dimethyl sulfoxide) for 2 h in the dark at 4 °C.

The alkaline denaturation was performed in an electrophoresis buffer solution (10 M NaOH, 200 mM EDTA, pH > 13) in a horizontal position and the slides were electrophoresed for 30 min at 25 V and 300 mA. The slides were washed in neutralizing Tris-HCl buffer (0.4 M Tris, pH 7.5) and stained with 50 μL ethidium bromide (20 μg/mL). One hundred randomly selected cells from each slide (50 cells from each of the two gel replicates) were visually analysed using a Nikon E50i fluorescence microscope at 400× magnification. Each cell was classified into five classes, from 0 (undamaged class cells) to 4 (the most severely damaged one).

The level of DNA damage, expressed as genetic damage index (*GDI*), was calculated for all 100 cells using the Eq. (1) described by Pitarque *et al*.[19] The level of DNA damage, expressed as the *GDI*, is:

$$GDI = \frac{Class1 + 2 \times Class2 + 3 \times Class3 + 4 \times Class4}{Class0 + Class1 + Class2 + Class3 + Class4} \quad (1)$$

Data analysis

The statistical analyses were performed using the SPSS package (IBM SPSS Statistics 21). The results are expressed as mean ± standard deviation (*SD*). *GDI* was evaluated by one-way analysis of variance (ANOVA), with a Tukey post hoc test for comparisons of different treatments v*ersus* negative controls. The relationship between the tested extract concentrations and the *GDI* was determined using the Pearson correlation coefficient. A statistically significant difference in *GDI* between the uncontaminated locality and tailing site was determined by Student's *t*-test. Levels of significance were $p < 0.05$, $p < 0.01$ and $p < 0.001$. To determine the existence of differences between PTE in the soil by localities, PTE, TPC, TFC and antioxidant activity, in plants from different localities, and differences between localities by plants, Tukey's tests were used ($p < 0.05$). In addition, a multivariate statistical method (PCA) was used to investigate the relationship between chemical elements in plant parts and different localities.

RESULTS AND DISCUSSION

Based on the concentrations of PTE in the soil at the tailing site, the analysed PTE (Table I) can be ranked as follows: Fe > Mg > Ca > Mn > Pb > Cr > Ni > Zn > Cu. In contrast, the ranking in uncontaminated soil is as follows: Fe > Ca > Mg > Mn > Ni > Cr > Zn > Pb > Cu.

TABLE I. The content of potentially toxic elements (PTE) in the examined soil samples (mg/kg); different uppercase letter (A, B, C,...) within a column indicates significant differences between PTE at the same locality ($p < 0.05$, ANOVA with Tukey's test). Different lowercase letters (a, b) within a row indicate significant differences in the content of the same PTE between the two localities ($p < 0.05$, ANOVA with Tukey's test)

PTE	Tailing site	Uncontaminated locality
Mn	2685.58±16.0 Aa	676.24±5.8 Ab
Ni	199±0.97 Ba	38.74±0.56 Bb
Ca	3649.76±31.20 Ca	4837.16±32.95 Cb
Mg	4540.54±23.4 Da	2236.86±36.41 Db
Fe	77363.08±682.37 Ea	24332.84±19.58 Eb
Zn	176.24±0.78 Fa	25.48±0.42 Fb
Cr	453.36±1.36 Ga	27.64±0.14 Gb
Pb	873.66±2.057 Ha	11.38±0.07 Hb
Cu	113.88±0.8 Ia	10.44±0.28 Ib

All metals (with the exception of Ca) have significantly higher concentrations at the tailing site. The most abundant PTE at the tailing site is Fe, with a concentration 3.18 times greater than in the uncontaminated soil. Also, an exceptionally high Pb concentration was observed at the tailing site, where it is 76.7 times higher than at an uncontaminated locality. For Ca and Mg, the differences between the two sites are smaller. PTE such as Pb, Cr and Zn exhibit particularly high disparities between the sites.

A comparative analysis of the PTE content in different plant parts from a tailing site and an uncontaminated site is shown in Table II. At the tailing site, the order of PTE concentration in the roots was: Ca > Mg > Fe > Ni > Mn > Zn > Cu > Cr > Pb. In the aerial parts, Ca, Mg, Cr, Fe and Zn were predominant, while in the inflorescences, Ca was dominant, followed by Mg, Zn and Fe. A particularly high Pb concentration was observed at the contaminated site, where the levels in the aerial parts (17.6 mg/kg) and roots (6.16 mg/kg) exceeded the permissible limits, ranging from 2 to 10 mg/kg, according to the regulations of the FAO/WHO.[20] Additionally, the Cr content in the aerial parts from the tailing area was significantly above the permissible levels (132.88 mg/kg compared to the allowed range of 5–20 mg/kg). At the uncontaminated site, the most abundant elements in the roots were Ca, Fe and Mg (Ca > Mg >Fe > Mn > Zn > Ni > Cu > Cr > Pb). The aerial parts primarily contained Ca, Mg, and Fe, while the inflorescences followed a similar pattern, with Ca and Mg being dominant. The concentrations of all PTE

at uncontaminated locality were within or below the recommended safety levels, while Pb was below the detection limit. Mn and Cr showed higher concentrations in the roots of the plants from the uncontaminated site compared to the tailing area.

TABLE II. The content of investigated potentially toxic elements (mg/kg) in root, aerial part and inflorescence of *O. viciifolia*; different uppercase letter (A, B, C,…) within a row indicates significant differences between plant parts (root, aerial part, inflorescence) at the same locality ($p < 0.05$, ANOVA with Tukey's test). Different lowercase letters (a, b) within a column indicate significant differences between the two localities (tailing site *vs.* uncontaminated) for the same plant organ ($p < 0.05$, ANOVA with Tukey's test); *n.d. = not detected

PTE	Tailing site			Uncontaminated		
	Root	Aerial part	Inflorescence	Root	Aerial part	Inflorescence
Mn	27.36 ± 1.28^{Ad}	81.92 ± 0.51^{Bc}	77.18 ± 0.29^{Bb}	34.52 ± 0.56^{Aa}	23.94 ± 0.63^{Ba}	23.38 ± 0.49^{b}
Ni	49.4 ± 0.28^{Ad}	12.42 ± 0.33^{Bd}	30.58 ± 0.42^{Cd}	8.67 ± 0.45^{Aa}	9.82 ± 0.14^{Ba}	13.56 ± 0.07^{b}
Ca	11892 ± 62.25^{Aa}	14772 ± 42.99^{Ba}	13856 ± 44.61^{Ba}	7802 ± 21.49^{Aa}	8142 ± 34.08^{Ba}	6258 ± 3.81
Mg	4161 ± 35.21^{Ab}	$6\,087\pm27.77^{Ba}$	7177 ± 37.56^{Ca}	2386 ± 9.26^{Aa}	2229 ± 24.53^{Ba}	1851 ± 38.18^{a}
Fe	447.36 ± 1.44^{Ac}	334.88 ± 38.77^{Bb}	304.82 ± 1.01^{Ca}	1399 ± 30.82^{Aa}	87.98 ± 3.81^{Ba}	424.1 ± 0.28^{a}
Zn	22.22 ± 0.23^{Ad}	41.28 ± 0.41^{Bc}	61.24 ± 0.36^{Cc}	18.56 ± 0.35^{Aa}	17.04 ± 0.56^{Ba}	35.78 ± 0.35^{b}
Cr	7.45 ± 0.04^{Ad}	132.88 ± 0.67^{Bc}	16.54 ± 0.34^{Cd}	9.86 ± 0.09^{Aa}	2.23 ± 0.05^{Ba}	2.28 ± 0.01^{b}
Pb	6.16 ± 0.03^{Ad}	17.6 ± 0.34^{Bd}	5.54 ± 0.03^{Ce}	*n.d.	*n.d.	*n.d.
Cu	9.86 ± 0.03^{Ad}	17.22 ± 0.31^{Bd}	5.30 ± 0.02^{Ce}	7.49 ± 0.15^{Aa}	3.87 ± 0.07^{Ba}	24.54 ± 0.08^{b}

Elevated concentrations of PTE, primarily Cd and Pb, in all plant parts collected from the tailing site compared to the uncontaminated locality, indicate a strong anthropogenic influence and long-term contamination of the soil with toxic metal compounds.[12,21] Furthermore, essential metals such as Ca, Mg and Fe, were present at both sites, they showed significant differences in concentration, which could be linked to alterations in the plant's biochemical regulation under PTE stress.[22,23]

The presentation of the principal component analysis (PCA) in plant parts and localities is presented in Fig. S-1 of the Supplementary material to this paper. The two main components (factor 1 and factor 2) for plant samples are represented with a variation of 69.02 %. The first two factors clearly show the differences in the amount of elements tailing site and the uncontaminated locality around the parts of the plant where PTE accumulate. Elements, such as Mn, Ni, Ca, Mg, Fe, Zn, Cr, Pb and Cu, are included in factor 2. High amounts of the mentioned elements are characteristic of the tailing site, which are grouped on the positive side of the PCA axis and most affect the separation of the plant population. The amounts of Mn, Ni, Ca, Fe, Zn and Cr have negative values around a factor 1, for the uncontaminated locality in the plant samples.

The results of the bioaccumulation and translocation factors (*BCF* and *TF*) for PTE in plant parts of *O. viciifolia* are presented in Fig. 1. The highest *BCF* in individuals of *O. viciifolia* from the tailings site was recorded for Ca, exceeding a

value of 3.5, indicating a high capacity of the plant to accumulate this element in its roots. Moderate accumulation was observed for Mg and Fe, with *BCF* values close to or slightly above 1. Other elements (Mn, Ni, Zn, Cr, Pb, Cu) exhibited low *BCF* values, below 1, suggesting limited accumulation of these metals by the plant. For plants from the uncontaminated site, *BCF* values for all elements were less pronounced compared to the tailings site. However, the highest accumulation was still recorded for Ca, but with a slightly lower value (around 2.5). Significant translocation from the roots to the aerial parts and inflorescences was observed for Cu in the plants collected from the tailing site, with *TF* values above 3. A higher *TF* value was also observed for Zn. In the plants of the uncontaminated site, the highest *TF* was also observed for Cu, albeit with lower values compared to the tailings site. The translocation of Ca and Mg from the roots to the aerial parts and inflorescences was more moderate compared to the tailings site.

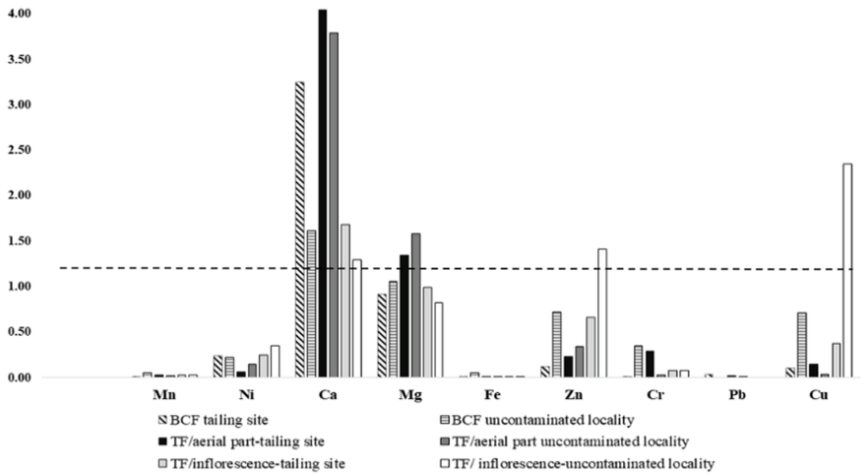

Fig. 1. Bioconcentration factor (B*CF*) and translocation factor (*TF*) of potentially toxic elements in *O. viciifolia*, which grows on the tailing site and an uncontaminated locality.

High *BCF* and *TF* factors at the tailing site indicate effective mechanisms for the uptake and transport of PTE from the roots to the aerial parts, aligning with previous studies suggesting that plants from contaminated sites adaptively enhance metal accumulation.[24] For example, a high *BCF* for calcium could reflect its role in stabilising cell membranes and acting as a signaling molecule under stress conditions, while a high *TF* for copper and zinc could be associated with their roles in antioxidant enzymes and plant metabolism.

The results of *TPC* and *TFC* revealed significant differences in the accumulation of phenolic compounds between plant parts and locations, indicating adaptive responses of the plant to environmental stress conditions (Table III).

TABLE III. Total phenolic and flavonoid content in the different parts of *O. viciifolia*; different capital letters (A, B, C) indicate significant differences among plant parts within the same locality. The same lowercase letters (a, b, c) indicate significant differences between localities for the same plant part, according to ANOVA with Tukey's test ($p < 0.05$)

Locality	Root	Aerial part	Inflorescence
Total phenolic content, mg GAE/g extracts			
Tailing site	80.22 ± 2.77^{Bb}	137.83 ± 1.45^{Aa}	47.72 ± 3.71^{Cc}
Uncontaminated locality	64.88 ± 0.25^{Ba}	86.16 ± 2.96^{Ab}	55.38 ± 0.41^{Ca}
Total flavonoid content, mg RUE/g extracts			
Tailing site	10.11 ± 0.39^{Cc}	66.64 ± 1.87^{Aa}	27.52 ± 1.49^{Bb}
Uncontaminated locality	20.33 ± 0.32^{Cb}	25.41 ± 0.52^{Bc}	28.52 ± 2.18^{Aa}

At the tailing site, the *TPC* in the roots was 80.22±2.77 mg GAE/g, which was significantly higher compared to the uncontaminated locality (64.88±0.25 mg GAE/g). The aerial parts of *O. viciifolia* showed the highest *TPC* value of all plant parts analysed (137.83±1.45 mg GAE/g for the tailing site and 86.16±2.96 mg GAE/g for the uncontaminated locality). The TPC in the inflorescences was lower compared to the roots and aerial parts at both localities.

At the tailing site, the flavonoid content in the roots was 10.11±0.39 mg RUE/g, significantly lower than at the uncontaminated site (20.33±0.32 mg RUE/g). The aerial parts of the plant exhibited the most significant difference in flavonoid content between the two sites. At the tailing site, the flavonoid content in the aerial parts reached 66.64±1.87 mg RUE/g, which is significantly higher than at the uncontaminated site, where it was 25.41±0.52 mg RUE/g. The flavonoid content in the inflorescences was similar at both sites, with slightly higher values at the uncontaminated site (Table III).

The elevated levels of *TPC* and *TFC* in the plants from the tailing site indicate a robust activation response to oxidative stress induced by heavy metals. Phenolic compounds are well-known for their ability to neutralize reactive oxygen species (ROS) and thereby protect cells from oxidative damage.[25] Interestingly, flavonoids were recorded in higher concentrations in the aerial parts of plants from the tailing site, while their content in the roots was reduced. This may indicate a redistribution of secondary metabolites in response to local stress or the inhibition of flavonoid biosynthesis in the roots due to the toxic effect of metals.[26]

A comparative analysis of the flavonoid, phenol and heavy metal content in *O. viciifolia* shows the plant's complex adaptation strategies to environmental stress conditions. At the tailing site, the plant increases the synthesis of flavonoids and phenols to combat oxidative stress caused by PTE contamination. However, the high metal accumulation limits their safety of use. Plants from uncontaminated localities, with a balanced content of secondary metabolites and a low metal content, are more suitable for phytotherapy and the food industry.

Despite the use of *O. viciifolia* in traditional medicine, these results present a dual message. Increased concentrations of phenols and flavonoids may enhance the medicinal properties of the plant, including antioxidant, anti-inflammatory and antimicrobial effects.[25] However, the presence of elevated levels of PTE, especially in the aerial parts used for phytopreparations, poses a serious health risk. Additionally, the ability of *O. viciifolia* to accumulate metals could be beneficial for phytoremediation of polluted areas, but plants growing in such environments must not be used as food or medicine.

The results of antioxidant activity for the root from tailing site was 13.66±0.89 μg/mL, representing significantly better activity compared to the root from the uncontaminated locality (32.75±1.68 μg/mL). The aerial parts of the plant demonstrated moderate antioxidant activity, with significant differences between localities. The inflorescences showed the lowest antioxidant activity compared to the root and aerial parts (Table IV). At the uncontaminated locality, antioxidant activity was more balanced among different plant parts, with inflorescences showing significantly higher activity compared to the tailing site.

TABLE IV. Antioxidant activity of the different parts of *O. viciifolia* (IC_{50} / μg mL^{-1}); different capital letters (A, B, C) indicate significant differences among plant parts within the same locality. The same lowercase letters (a, b, c) indicate significant differences between localities for the same plant part, according to ANOVA with Tukey's test ($p < 0.05$)

Locality	Root 1	Aerial part	Inflorescence
Tailing site	13.66 ± 0.89^{Cc}	74.4 ± 1.57^{Bb}	109.6 ± 3.15^{Aa}
Uncontaminated locality	32.75 ± 1.68^{Ca}	65.4 ± 0.96^{Bb}	77.72 ± 1.57^{Ab}

The genotoxicity of plants from the Fabaceae family has been tested,[27,28] but to our knowledge, similar studies have not yet been conducted on the genus *Onobrychis*, so our results represent a novelty in this field of research. The results of analysis of DNA damage level in treatment with different parts of *O. viciifolia* extracts from uncontaminated locality and tailing site are shown in Fig. 2. All tested concentrations (125–1000 μg/mL) of extracts from root, inflorescence and aerial part of *O. viciifolia* extracts from the uncontaminated locality significantly increased the *GDI* (from 1.16±0.09 to 1.78±0.17 for the root; from 0.91±0.08 to 1.93±0.24 for the inflorescence; from 1.44±0.05 to 2.27±0.07 for the aerial part) in comparison to the negative control (ANOVA, Tukey *post hoc* test, $p < 0.05$). A strong positive correlation between concentrations of the extracts and *GDI* was obtained (Pearson: $r = 0.787$, $p = 0.001$ for the root; $r = 0.931$, $p = 0.000$ for the inflorescence; $r = 0.785$, $p = 0.001$ for the aerial part). All tested extracts of *O. viciifolia* from the tailing site significantly increased the *GDI* in all concentrations compared to the negative control (ANOVA, Tukey *post hoc* test, $p < 0.05$). The highest tested concentration of extracts (1000 μg/mL) increased the *GDI* by 8.2 times for root (2.63±0.19), 8.3 times (2.67±0.10) for inflorescence and 9.9 times

(3.16±0.04) for aerial part, in comparison to the negative control (0.32±0.08). Pearson correlation coefficient revealed a significant association between *GDI* and the tested concentrations of extracts ($r = 0.838$, $p = 0.000$ for root; $r = 0.891$, $p = 0.000$ for inflorescence; $r = 0.756$, $p = 0.001$ for aerial part). Plants from both the uncontaminated locality and tailing site showed a genotoxic effect. All extracts obtained of different plant parts from the tailing site had a significantly higher *GDI*, compared to the same plant parts extracts from the uncontaminated locality ($p < 0.05$). The highest genotoxic effect was observed in the treatment with the extract of the aerial plant part from the tailing site at all tested concentrations. The extract of the inflorescence of the plant from the uncontaminated locality exhibited the lowest *GDI* at all tested concentrations, except at the concentration of 1000 μg/mL, where an insignificantly higher *GDI* was observed for the root extract (1.93±0.24 *vs*. 1.78±0.17).

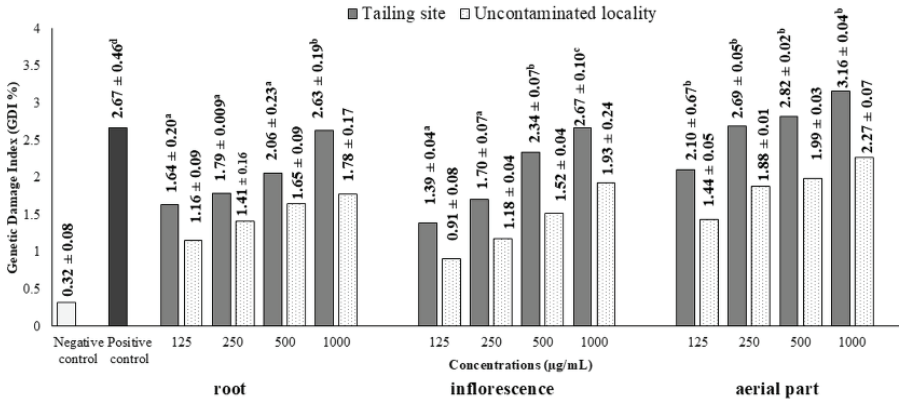

Fig. 2. Comparative results of the level of DNA damage in lymphocytes treated with methanolic *O. viciifolia* extracts from two localities. The results are expressed as mean ± *SD*, $n = 3$; $^{a}p < 0.05$; $^{b}p < 0.01$; $^{c}p < 0.001$, $^{d}p < 0.0005$ statistically significant difference of *GDI* between localities (Student's *t*-test).

The observed genotoxic activity of the methanol extracts of the plants from both localities could be influenced by the exposure of plants to PTE, which affected the synthesis of secondary metabolites. The PTE analysis showed that the plants contained a higher amount of Ni, Zn and Cr compared to the other identified metals, and these amounts were several times higher in the tailings than in the uncontaminated locality. In addition, the high Pb concentration was only detected in various plant parts of the tailings. Previous studies have shown that Ni can induce DNA damage through direct DNA binding and ROS stimulation.[29,30] Low concentrations of Pb also induce genotoxicity.[31] It is also known that Cr has a genotoxic effect and causes chromosomal damage and the formation of oxidized DNA adducts as well as the formation of DNA and protein/amino acid cross-links.

One of the possible mechanisms is the reduction of glutathione, which could generate free radical species such as hydrogen peroxide that produce high levels of oxidative stress and cause DNA damage.[32,33] In addition, Dutta *et al.*[34] showed that high concentrations of heavy metals can trigger genotoxic activities by directly attacking the thiol groups of proteins, leading to disruption of protein structure and function.

CONCLUSION

The results of this study revealed significant differences in phenolic and flavonoid contents, as well as in antioxidant and genotoxic activities, between plants collected from a tailing site and an uncontaminated locality. *O. viciifolia* from the tailing site exhibited pronounced adaptive mechanisms, including increased synthesis of phenolics and flavonoids, which contributed to enhanced antioxidant activity under stressful conditions. These adaptive responses were particularly prominent in the roots and aerial parts of the plants, highlighting their significant role in mitigating oxidative stress induced by potentially toxic elements. Conversely, the plants from the uncontaminated site displayed a more balanced chemical profile, with a lower accumulation of potentially toxic elements and a stable content of bioactive compounds, making them more suitable for medicinal and nutritional applications. Plants from both sites (uncontaminated and tailing site) demonstrated genotoxic effects, with the level of genotoxicity correlating with the concentration of analysed elements in the soil. Further research is needed to isolate bioactive compounds and evaluate their pharmacological safety.

SUPPLEMENTARY MATERIAL

Additional data and information are available electronically at the pages of journal website: https://www.shd-pub.org.rs/index.php/JSCS/article/view/13515, or from the corresponding author on request.

Acknowledgement. This investigation was supported by the Ministry of Science, Technological Development and Innovation of the Republic of Serbia (Agreement No. 451-03-137/ /2025-03/200122 and 451-03-136/2025-03/ 200122).

ИЗВОД

АКУМУЛАЦИЈА МЕТАЛА У БИЉЦИ *Onobrychis viciifolia* SCOP., ЊИХОВА РАСПОДЕЛА У БИЉНИМ ОРГАНИМА И УТИЦАЈ НА САДРЖАЈ ФЕНОЛА И ФЛАВОНОИДА, КАО И НА АНТИОКСИДАТИВНУ И ГЕНОТОКСИЧНУ АКТИВНОСТ

ГОРИЦА Т. ЂЕЛИЋ[1], МИЛИЦА Б. ПАВЛОВИЋ[1], ЗОРАН Б. СИМИЋ[2], ЈОВАНА М. ТУБИЋ ВУКАЈЛОВИЋ[1], ДАРКО В. ГРУЈИЧИЋ[1], МАРИНА З. РАДОВИЋ ЈАКОВЉЕВИЋ[1] и ОЛИВЕРА М. МИЛОШЕВИЋ-ЂОРЂЕВИЋ[1,3]

[1]Универзитет у Крагујевцу, Природно–математички факултет, Институт за биологију и екологију, Радоја Домановића 12, Крагујевац, [2]Универзитет у Крагујевцу, Природно–математички факултет, Институт за хемију, Радоја Домановића 12, Крагујевац и [3]Универзитет у Крагујевцу, Факултет медицинских наука, Катедра за генетику, Светозара Марковића 69, Крагујевац

Ово истраживање је испитивало садржај потенцијално токсичних елемената (ПТЕ) и биолошке активности биљке *Onobrychis viciifolia* Scop. прикупљене са јаловишта и неконтаминираног локалитета. Концентрације Mn, Ni, Ca, Mg, Fe, Zn, Cr, Pb и Cu одређене су у земљишту и биљним деловима (корену, надземним деловима и цвасти) применом методе мокрог спаљивања, а затим атомском апсорпционом спектрофотометријом. Рачунати су фактори биоакумулације (*BCF*) и транслокације (*TF*) ради процене усвајања и расподеле метала. Укупни садржај фенола и флавоноида одређиван је спектрофотометријски. Антиоксидативна активност процењивана је помоћу DPPH теста за неутрализацију слободних радикала. Оштећење ДНК у хуманим лимфоцитима третирано биљним екстрактима испитано је комет тестом. Резултати су показали значајно више концентрације ПТЕ у земљишту и биљним деловима са контаминираног локалитета у поређењу са неконтаминираним. Биљке са контаминираног земљишта показале су повећану биоакумулацију и транслокацију ПТЕ. Поред тога, биолошка активност екстраката, укључујући антиоксидативни капацитет и генотоксичне ефекте, била је под утицајем изложености биљака ПТЕ, што је утицало на синтезу секундарних метаболита. Екстракти биљака са јаловишта испољили су јачу активност у поређењу са биљкама са неконтаминираног локалитета. Ово истраживање истиче адаптивне одговоре *O. viciifolia* на стрес изазван ПТЕ и пружа увид у њене потенцијалне примене у еколошком мониторингу и фитофармакологији.

(Примљено 27. августа, ревидирано 16. октобра, прихваћено 3. децембра 2025)

REFERENCES

1. M. Zarrabian, A. N. Dehkordi, M. H. Ehtemam, M. M. Majidi, *BioRxiv* **42** (2022) 342 (https://doi.org/10.1101/2022.05.02.490301)
2. I. Mueller-Harvey, G. Bee, F. Dohme-Meier, H. Hoste, M. Karonen, R. Kölliker, A. Lüscher, V. Niderkorn, W. F. Pellikaan, J.-P. Salminen, L. Skøt, L. M. J. Smith, S. M. Thamsborg, P. Totterdell, I. Wilkinson, A. R. Williams, B. N. Azuhnwi, N. Baert, A. Grosse Brinkhaus, G. Copani, O. Desrues, C. Drake, M. Engström, C. Fryganas, M. Girard, N. T. Huyen, K. Kempf, C. Malisch, M. Mora-Ortiz, J. Quijada, A. Ramsay, H. M. Ropiak, G. C. Waghorn, *Crop Sci.* **59** (2019) 861 (https://doi.org/10.2135/cropsci2017.06.0369)
3. A. Pricop, M. Smaranda, L. Benoni, M. Florica, D. Neculai, N. F. Isabelle, P. Dumitru, *Anim. Sci. Biotechnol.* **44** (2011) 229 (https://spasb.ro/index.php/public_html/article/view/1928)
4. J. Briffa, E. Sinagra, R. Blundell, *Heliyon* **6** (2020) e04691 (https://doi.org/10.1016/j.heliyon.2020.e04691)
5. L. Skuza, I. Szućko-Kociuba, E. Filip, I. Bożek, *Int. J. Mol. Sci.* **23** (2022) 9335 (https://doi.org/10.3390/ijms23169335)

6. A. Yan, Y. Wang, S. N. Tan, M. L. Mohd Yusof, S. Ghosh, Z. Chen, *Front. Plant Sci.* **11** (2020) 359 (https://doi.org/10.3389/fpls.2020.00359)
7. B. Butkutė, A. Padarauskas, J. Cesevičienė, A. Pavilonis, L. Taujenis, N. Lemežienė, *J. Food Sci. Techol.* **54** (2017) 2661 (https://doi.org/10.1007/s13197-017-2703-8)
8. L. A. Mărghitaş, C. Paşca, D. S. Dezmirean, O. Bobis, V. Bonta, R. Mărgăoan, N. L. Fit, *Buil. Univ. Agri. Sci. Vet. Med. Cluj-Napoca. Anim. Sci. Biotechnol.* **73** (2016) 261 (https://doi.org/10.15835/buasvmcn-asb:12295)
9. M. Komáromyová, D. Petrič, K. Kucková, D. Batťányi, M. Babják, M. U. Dolinska, A. Königová, D. Barčák, E. Dvorožňáková, K. Čobanová, Z. Váradyová, M. Várady, *Pathogens* **11** (2022) 301 (https://doi.org/10.3390/pathogens11030301)
10. P. J. Rufino-Moya, J. R. Bertolín, M. Blanco, S. Lobón, M. Joy, *J. Sci. Food Agric.* **102** (2022) 4736 (https://doi.org/10.1002/jsfa.11834)
11. G. Tóth, T. Hermann, M. R. Da Silva, L. Montanarella, *Environ. Int.* **88** (2016) 299 (https://doi.org/10.1016/j.envint.2015.12.017)
12. A. Kabata-Pendias, *Trace Elements in Soils and Plants*, CRC Press, Taylor and Francis Group, Boca Raton, FL, 2010 (https://doi.org/10.1201/b10158)
13. S. Gupta, S. Nayek, R. N. Saha, S. Satpati, *Environ. Geol.* **55** (2008) 731 (https://doi.org/10.1007/s00254-007-1025-y)
14. P. C. Wootton-Beard, A. Moran, L. Ryan, *Food Res. Int.* **44** (2011) 217 (https://doi.org/10.1016/j.foodres.2010.10.033)
15. C. Quettier-Deleu, B. Gressier, J. Vasseur, T. Dine, C. Brunet, M. Luyckx, M. Cazin, J. C. Cazin, F. Bailleul, F. Trotin, *J. Ethnopharmacol.* **72** (2000) 35 (https://doi.org/10.1016/s0378-8741(00)00196-3)
16. T. Takao, F. Kitatani, N. Watanabe, A. Yagi, K. Sakata, *Biosci. Biotechnol. Biochem.* **58** (1994) 1780 (https://doi.org/10.1271/bbb.58.1780)
17. N. P. Singh, M. T. McCoy, R. R. Tice, E. L. Schneider, *Exp. Cell Res.* **175** (1988) 184 (https://doi.org/10.1016/0014-4827(88)90265-0)
18. A. Collins, P. Moller, G. Gajski, S. Vodenková, A. Abdulwahed, D. Anderson, E. E. Bankoglu, S. Bonassi, E. Boutet-Robinet, G. Brunborg, C. Chao, M. S. Cooke, C. Costa, S. Costa, A. Dhawan, J. de Lapuente, C. Del Bo', J. Dubus, M. Dusinska, S. J. Duthie, N. El Yamani, B. Engelward, I. Gaivão, L. Giovannelli, R. Godschalk, S. Guilherme, K. B. Gutzkow, K. Habas, A. Hernández, O. Herrero, M. Isidori, A. N. Jha, S. Knasmüller, I. M. Kooter, G. Koppen, M. Kruszewski, C. Ladeira, B. Laffon, M. Larramendy, L. Le Hégarat, A. Lewies, A. Lewinska, G. E. Liwszyc, A. López de Cerain, M. Manjanatha, R. Marcos, M. Milić, V. Moraes de Andrade, M. Moretti, D. Muruzabal, M. Novak, R. Oliveira, A.-K. Olsen, N. Owiti, M. Pacheco, A. K. Pandey, S. Pfuhler, B. Pourrut, K. Reisinger, E. Rojas, E. Rundén-Pran, J. Sanz-Serrano, S. Shaposhnikov, V. Sipinen, K. Smeets, H. Stopper, J. P. Teixeira, V. Valdiglesias, M. Valverde, F. van Acker, F.-J. van Schooten, M. Vasquez, J. F. Wentzel, M. Wnuk, A. Wouters, B. Žegura, T. Zikmund, S. A. S. Langie, A. Azqueta, *Nat. Protoc.* **18** (2023) 929 (https://doi.org/10.1038/s41596-022-00754-y)
19. M. Pitarque, A. Vaglenov, M. Nosko, A. Hirvonen, H. Norppa, A. Creus, R. Marcos, *Mutat. Res*. **441** (1999) 115 (https://doi.org/10.1016/s1383-5718(99)00042-x)
20. FAO/WHO, *Joint FAO/WHO Food Standards Programme Codex Alimentarius Commission. Working document for information and use in discussions related to contaminants and toxins in the GSCTFF*, Rome, Italy, 2011, https://www.fao.org/fao-who-codexalimentarius (Date of accession: 26.07.2024)

21. R. Sun, Y. Gao, Y. Yang, *Chemosphere* **291** (2022) 132792 (https://doi.org/10.1016/j.chemosphere.2021.132792)
22. G. E. Kroh, M. Pilon, *Int. J. Mol. Sci.* **21** (2020) 3395 (https://doi.org/10.3390/ijms21093395)
23. X. Weng, H. Li, C. Ren, Y. Zhou, W. Zhu, S. Zhang, L. Liu, *Front. Plant Sci.* **13** (2022) 887098 (https://doi.org/10.3389/fpls.2022.887098)
24. L. Córdoba-Tovar, S. Marrugo-Madrid, L. P. Castro, E.E. Tapia-Contreras, J. Marrugo--Negrete, S. Díez, *Environ. Sci. Pollut. Res. Int.* **32** (2025) 3795 (https://doi.org/10.1007/s11356-024-35853-8).
25. R. Karamian, M. Asadbegy, *Pharm. Sci.* **22** (2016) 112 (https://doi.org/10.15171/PS.2016.18)
26. M. Jańczak-Pieniążek, J. Cichoński, P. Michalik, G. Chrzanowski, *Molecules* **28** (2022) 241 (https://doi.org/10.3390/molecules28010241)
27. T. O. R. Falcoski, N. M. Lima, G. Navegante, R. B. Serafim, J. M. Sorbo, V. Valente, V. N. C. Santos, R. A. Santos, D. H. Silva, C. P. Soares, *Nat. Prod. Res.* **35** (2021) 676 (https://doi.org/10.1080/14786419.2019.1590711)
28. P. Mussali-Galante, S. Gómez-Arroyo, A. Rodríguez-Solís, L. Valencia-Cuevas, A. R. Flores-Márquez, M. L. Castrejón-Godínez, A. I. Murillo-Herrera, E. Tovar-Sánchez, *Environ. Sci. Pollut. Res.* **31** (2024) 47116 (https://doi.org/10.1007/s11356-024-34239-0)
29. S. Di Bucchianico, A. R. Gliga, E. Åkerlund, S. Skoglund, I. O. Wallinder, B. Fadeel, H. L. Karlsson, *Part. Fibre Toxicol.* **15** (2018) 32 (https://doi.org/10.1186/s12989-018-0268-y)
30. H. Guo, H. Liu, H. Wu, H. Cui, J. Fang, Z. Zuo, J. Deng, Y. Li, X. Wung, L. Zhao, *Int. J. Mol. Sci.* **20** (2019) 4690 (https://doi.org/10.3390/ijms20194690)
31. C. Lang, J. Tang, G. Zhang, Y. Meng, W. W. Au, Z. Xia, T. Wang, *Ecotoxicol. Environ. Saf.* **283** (2024) 116796 (https://doi.org/10.1016/j.ecoenv.2024.116796)
32. T. L. DesMarais, M. Costa, *Curr. Opin. Toxicol.* **14** (2019) 1 (https://doi.org/10.1016/j.cotox.2019.05.003)
33. V. Singh, K. Abhishek, S. N. Rai, S. K. Sing, E. Vamanu, A. Kumar, *Green Chem. Lett. Rev.* **16** (2023) 2267079 (https://doi.org/10.1080/17518253.2023.2267079)
34. S. Dutta, M. Mitra, P. Agarwal, K. Mahapatra, S. De, U. Set, S. Roy, *Plant Signal. Behav.* **13** (2018) 146004813 (https://doi.org/10.1080/15592324.2018.1460048).

Journal of the Serbian Chemical Society
JSCS@tmf.bg.ac.rs • www.shd.org.rs/JSCS
J. Serb. Chem. Soc. 91 (2) S53 (2026) *Supplementary material*

SUPPLEMENTARY MATERIAL TO

The accumulation of metals in *Onobrychis viciifolia* Scop., their distribution in plant parts and the impact on the content of phenols and flavonoids, as well as antioxidant and genotoxic activity

GORICA T. ĐELIĆ[1], MILICA B. PAVLOVIĆ[1], ZORAN B. SIMIĆ[2], JOVANA M. TUBIĆ VUKAJLOVIĆ[1], DARKO V. GRUJIČIĆ[1], MARINA Z. RADOVIĆ JAKOVLJEVIĆ[1]* and OLIVERA M. MILOŠEVIĆ-ĐORĐEVIĆ[1,3]

[1]*University of Kragujevac, Faculty of Science, Department of Biology and Ecology, Radoja Domanovica 12, Kragujevac, Serbia,* [2]*University of Kragujevac, Faculty of Science, Department of Chemistry, Radoja Domanovica 12, Kragujevac, Serbia and* [3]*University of Kragujevac, Faculty of Medical Sciences, Department of Genetics, Svetozara Markovića 69, Kragujevac, Serbia*

J. Serb. Chem. Soc. 91 (2) (2026) 99–112

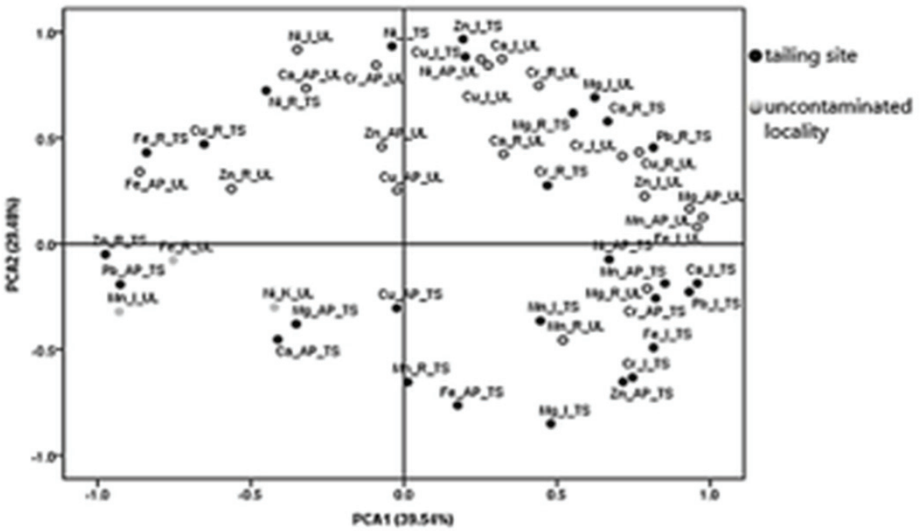

Fig. S-1. Presentation of principal component analysis (PCA) in plant parts and localities, *R-root, AP-aerial part, I-Inflorescence, TS-tailing site, UL-uncontaminated locality.

* Corresponding author. E-mail: marina.jakovljevic@pmf.kg.ac.rs

Journal of the Serbian Chemical Society
JSCS@tmf.bg.ac.rs • www.shd.org.rs/JSCS
J. Serb. Chem. Soc. *91* (2) 113–127 (2026)
JSCS–5481
Original scientific paper
Published 8 February, 2026

Spectral characterization and antimicrobial activity studies of 5,6-dichloro-1*H*-benzimidazol-2-yl-(4'/5'/6'-substituted)-phenols (HL_1–HL_{20}) and Co(II), Ni(II), Cu(II), Zn(II) and Pd(II) complexes of HL_1

AYDIN TAVMAN[1]*, DEMET GURBUZ[2], MAYRAM HACIOGLU[3], ADEM CINARLI[2], ONUR SAHIN[4] and A. SEHER BIRTEKSOZ TAN[3]

[1]Istanbul University-Cerrahpaşa, Faculty of Engineering, Department of Chemistry, Inorganic Chemistry Division, 34320 Avcilar, Istanbul, Türkiye, [2]Istanbul University-Cerrahpaşa, Faculty of Engineering, Department of Chemistry, Organic Chemistry Division, 34320 Avcilar, Istanbul, Türkiye, [3]Istanbul University, Faculty of Pharmacy, Department of Pharmaceutical Microbiology, 34452 Beyazit, Istanbul, Türkiye and [4]Sinop University, Faculty of Health Sciences, Department of Occupational Health and Safety, 57000 Sinop, Türkiye

(Received 6 August, revised 12 October, accepted 29 October 2025)

Abstract: 5,6-Dichloro-1*H*-benzimidazol-2-yl-(4'/5'/6'-substituted)-phenols (**HL_1**–**HL_{20}**) and MCl_2 complexes (M: Co, Ni, Cu, Zn, Pd) of **HL_1** were synthesized and characterized by various physicochemical and spectroscopic methods such as elemental analysis, thermogravimetric analysis, FTIR, NMR and fluorescence spectroscopy. The structures of the complexes were also confirmed by performing molar conductivity and magnetic moment measurements. **HL_1** acted as a bidentate, monobasic chelating ligand with NO donor sites in all the complexes. It was found that all complexes have non-electrolytic properties and the M:L ratios are 1:1 in the Zn(II) complex and 1:2 in the other complexes. Crystal structure of **HL_{18}** was also investigated. The presence of both intra- and inter-molecular hydrogen bonding was observed in both molecules. According to the fluorescence spectral data, the substituents at the 4-position made the fluorescence emission shifted to the lower wavelengths (redshift) compared to **HL_1**, while the substituents at the 3- and 5-positions caused a blue shift effect. The Zn(II) complex showed a greater redshift effect compared to the other complexes. In addition, antimicrobial activity of the compounds was evaluated against six bacteria and three fungi. It was observed that **HL_1** and its mono substituted derivatives (**HL_1**–**HL_{11}**) show selective activity especially against Gram-positive bacteria, *Staphylococcus aureus* and *Staphylococcus epidermidis*. Zn(II) complex showed relatively higher activity against Gram-positive bacteria differently from the other complexes.

* Corresponding author. E-mail: atavman@iuc.edu.tr
https://doi.org/10.2298/JSC250806078T

Keywords: benzimidazolylphenol; halogen; transition metal complexes; antibacterial; antifungal.

INTRODUCTION

It is known that many benzimidazole derivatives play a role in the field of pharmacology as the active ingredient of many drugs. For example, 4-{5-[bis(2--chloroethyl)amino]-1-methyl-2-bezimidazolyl}butyric acid hydrochloride, also known as bendamustine and used as a chemotherapy agent, is one of them.[1,2] Perhaps the well-known one is omeprazole, 5-methoxy-2-(4-methoxy-3,5-dimethylpyridin-2-yl-methylsulphinyl)-1*H*-benzimidazole, an antisecretory agent.[3] Other important benzimidazole derivatives used as drugs include thiabendazole,[4,5] albendazole, mebendazole, flubendazole,[6,7] astemizole[8] and fenbendazole.[9]

Many researchers in different parts of the world continue their research on benzimidazole derivatives because they have a wide range of biological activities, especially antimicrobial, antiviral, antifungal, anti-inflammatory, proton pump and pancreatic lipase inhibitor, hormone modulator, antihypertensive, antidiabetic, antidepressant, anticoagulant, *etc*.[10–14] Also, it is known that there is a 5,6-dimethylbenzimidazole moiety that coordinated to a Co(II) ion through the imidazole C=N nitrogen atom in vitamin B12.[15]

Benzimidazole derivatives containing phenol groups, benzimidazolylphenols, are one of the current and widespread research topics, and their results have application potential in many areas. One of the most important features of these compounds is that they form strong chelate complexes with a two-ring structure by coordinating to metals through phenolic OH oxygen and C=N nitrogen atoms. In addition, many studies have been published examining the photophysical properties of these compounds and their complexes with strong fluorescent characteristics.[16,17]

We reported that many benzimidazolyl-phenol derivatives and some of their transition metal complexes exhibited antibacterial and antifungal effect in our previous studies.[18] For example, 2-(5-nitro-1*H*-benzimidazol-2-yl)-bromophenol and its Zn(II), Fe(III) and Cu(II) complexes showed considerable antibacterial activity on *Staphylococcus aureus* and *Staphylococcus epidermidis*.[19,20] It is observed that the Cl, Br and NO_2 groups in some 5-methoxy-2-(5-substituted-1*H*-benzimidazol--2-yl)-phenols increase the antimicrobial activity toward *S. aureus*, *Enterococcus faecalis* and *Candida albicans*.[21]

In this study, twenty benzimidazolylphenol derivatives, eighteen of them are new, 5,6-dichloro-1*H*-benzimidazol-2-yl-(4'/5'/6'-substituted)-phenols (**HL_1**–**HL_{20}**, Scheme 1) were synthesized and characterized. The compounds except for **HL_1** and **HL_4** are reported for the first time in this study. The compound 2-(5,6-dichloro-1*H*-benzimidazol-2-yl)phenol (**HL_1**) and its Mn(III), Fe(II), Co(II) and Ni(II) complexes were reported in the literature.[22–24] Additionally, the anticancer

effect of a group of compounds, including **HL$_1$**, was examined, and it was reported that **HL$_1$** showed very weak anticancer activity against A549, MDA-MB-231 and PC3 cell lines (IC_{50} value >100 μg mL^{-1} for all three cell types).[25] The anticancer activity of **HL$_4$** was also investigated, but no significant effect was observed.[26] We also prepared and characterized the MCl_2 complexes (M: Co, Ni, Cu, Zn, Pd) of **HL$_1$**. In addition, antimicrobial activities of the compounds were tested towards six bacteria and three fungi. The structural characteristics and antimicrobial activity of the compounds were investigated and compared.

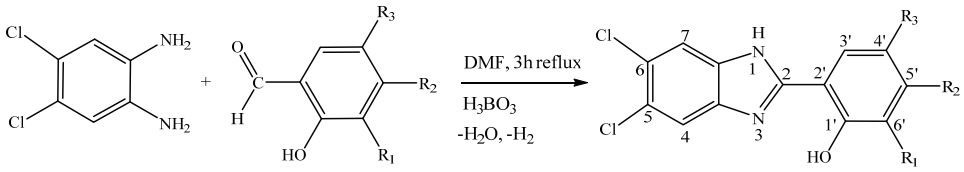

R$_1$=R$_2$=R$_3$=H (**HL$_1$**) R$_1$=R$_2$=H, R$_3$=F (**HL$_2$**)
R$_1$=R$_2$=H, R$_3$=Br (**HL$_3$**) R$_1$=R$_2$=H, R$_3$=Cl (**HL$_4$**)
R$_1$=R$_2$=H, R$_3$=I (**HL$_5$**) R$_1$=Cl, R$_2$=R$_3$=H (**HL$_6$**)
R$_1$=OCH$_3$, R$_2$=R$_3$=H (**HL$_7$**) R$_1$=H, R$_2$=OCH$_3$, R$_3$=H (**HL$_8$**)
R$_1$=R$_2$=H, R$_3$=OCH$_3$ (**HL$_9$**) R$_1$=R$_2$=H, R$_3$=CH$_3$ (**HL$_{10}$**)
R$_1$=CH$_3$, R$_2$=R$_3$=H (**HL$_{11}$**) R$_1$=Br, R$_2$=H, R$_3$=Cl (**HL$_{12}$**)
R$_1$=F, R$_2$=H, R$_3$=Br (**HL$_{13}$**) R$_1$=Cl, R$_2$=H, R$_3$=F (**HL$_{14}$**)
R$_1$=Cl, R$_2$=H, R$_3$=Cl (**HL$_{15}$**) R$_1$=Br, R$_2$=H, R$_3$=Br (**HL$_{16}$**)
R$_1$=I, R$_2$=H, R$_3$=I (**HL$_{17}$**) R$_1$=OCH$_3$, R$_2$=H, R$_3$=Cl (**HL$_{18}$**)
R$_1$=OCH$_3$, R$_2$=H, R$_3$=Br (**HL$_{19}$**) R$_1$=Br, R$_2$=OCH$_3$, R$_3$=Br (**HL$_{20}$**)

Scheme 1. Synthesis scheme and chemical structures of 5,6-dichloro-1*H*-benzimidazol-2-yl--(4'/5'/6'-substituted)-phenols in the study.

EXPERIMENTAL

Chemistry and apparatus

All chemicals and solvents were of reagent grade and they were used without further purification. Information on the chemicals and equipment used is provided as supporting information.

*Synthesis of 5,6-dichloro-1*H*-benzimidazol-2-yl-(4'/5'/6'-substituted)-phenols (**HL$_1$**–**HL$_{20}$**)*

A modified method developed by us, by utilizing two different methods available in the literature, was applied in the synthesis of benzimidazolylphenol derivatives.[27,28] An appropriate aldehyde (0.003 mol) and 4,5-dichlorobenzene-1,2-diamine (0.003 mol, 0.531 g) and 0.150 g H_3BO_3 as catalyst were dissolved in 20 mL DMF, and refluxed for 3 h. The reaction mixture was left to cool at room temperature and then poured into 250 mL of water, after which a precipitate formed. It was filtered, then dried and crystallized from ethanol. The compounds were obtained in yields ranging from 65 to 94 %. Physicochemical and spectroscopic data for **HL$_1$**––**HL$_{20}$** are given in the supplementary file.

Synthesis of the complex compounds

Appropriate metal salt solutions (7.5×10^{-4} mol of $CoCl_2\cdot6H_2O$, $NiCl_2\cdot6H_2O$, $CuCl_2\cdot2H_2O$ in 10 mL ethanol, K_2PdCl_4 (obtained by dissolving 1 mmol $PdCl_2$ (0.177 g) and 2 mmol KCl

(0.15 g) in 10 mL MeOH+H_2O mixture (6:4 volume ratio)) and $ZnCl_2 \cdot 6H_2O$ in 10 mL of ethyl-acetate was added to a solution of the **HL_1** (0.210 g, 7.5×10^{-4} mol) in appropriate solvent (15 mL), and refluxed for 3 h. The resulting precipitates were filtered off after cooling the reaction mixture, washed with a very small amount of methanol and water and kept at room temperature to dry.

Spectral and analytical data of the complexes are given in Supplementary material to this paper.

Determination of antimicrobial activity

Antibacterial activity of samples was studied *in vitro* with microbroth dilution technique against *Staphylococcus aureus* ATCC 29213 (meticillin susceptible *Staphylococcus aureus*, MSSA), *Enterococcus facealis* ATCC 29212, *Escherichia coli* ATCC 25922, *Klebsiella pneumonia* ATCC 4352, *Pseudomonas aeruginosa* ATCC 27853, *Staphylococcus epidermidis* ATCC 12228. Antifungal activity was assayed *in vitro* against *Candida albicans* ATCC 10231, *Candida parapsilosis* ATCC 22019 and *Candida tropicalis* ATCC 750. The evaluation of antibacterial and antifungal activity was done using micro broth dilution technique according to the Clinical Laboratory Standards Institute (CLSI) guidance[29,30] as detailed in previous studies.[21]

The samples were evaluated for their antibacterial and antifungal potency against members of Gram-negative bacteria, Gram-positive bacteria, and Candida spp. As reference compounds, ciprofloxacin for antibacterial assays, and Amphotericin B for antifungal assays were preferred.

X-Ray diffraction analysis

Suitable crystals of **HL_{18}** were selected for data collection which was performed on a D8-QUEST diffractometer equipped with a graphite-monochromatic MoK_α radiation at 296 K. The structure was solved by direct methods using SHELXS-2013[31] and refined by full-matrix least-squares methods on F^2 using SHELXL-2013.[32] All non-hydrogen atoms were refined with anisotropic parameters. The following procedures were implemented in our analysis. Data collection: Bruker APEX2;[33] program used for molecular graphics were as follows: Mercury programs;[34] software used to prepare material for publication: WinGX.[35]

RESULTS AND DISCUSSION

Crystal structure of ***HL_{18}***

Crystal data and structure refinement parameters related **HL_{18}** are given in Table I. Some important data on bond distances and bond angles are shown in Table S-I of the Supplementary material, and hydrogen bond parameters are shown in Table II. Molecular structure of **HL_{18}** is shown in Fig. 1, and the molecular planes and intermolecular hydrogen bonds in Fig. S-1 of the Supplementary material.

HL_{18} crystallized in the monoclinic system. The C–O bond length of 1.353 Å, indicate that the bond has a typical phenolic C–O length. It is clearly seen that there is an intramolecular hydrogen bond with N2···H1A distance 1.86 Å. There is also intermolecular hydrogen bond in the molecule. There appears to be four different intermolecular hydrogen bonds in **HL_{18}**: C14–H14A···O1 (2.36 Å), N2–H2A···Cl3 (2.21 Å), O1–H1···Cl3 (2.24 Å) and O2–H2B···Cl3 (2.23 Å). These hydrogen bonds affect the solubility and stability of the molecule.

TABLE I. Crystal data and structure refinement parameters

Empirical formula	$C_{14}H_9Cl_3N_2O_2$
Formula weight	343.58
Crystal system	Monoclinic
Space group	*C2/c*
a / Å	27.298 (4)
b / Å	7.3699 (9)
c / Å	14.1238 (18)
β / °	100.596 (4)
V / Å^3	2793.1 (6)
iZ	8
D_c / g cm^{-3}	1.634
μ / mm^{-1}	0.66
θ range, °	2.9-26.5
Measured refls.	28774
Independent refls.	3224
R_{int}	0.058
S	1.05
R1/*wR2*	0.049/0.107
$\Delta\rho_{max}/\Delta\rho_{min}$	0.26/–0.25
CCDC	2194768

TABLE II. Hydrogen-bond parameters; symmetry codes: (*i*) −*x*, *y*+1/2, −*z*+1/2; (*ii*) −x+1, *y*+1/2, −*z*+1/2

D–H···A	D–H, Å	H···A, Å	D···A, Å	D–H···A, °
O1—H1A···N2	0.82	1.86	2.594	148
C14—H14A···O1	0.97	2.36	3.108 (4)	134
N2—H2A···Cl3^{i}	0.86	2.21	3.063 (3)	176
O1—H1···Cl3	0.82	2.24	3.047 (3)	166
O2—H2B···Cl3^{ii}	0.82	2.23	3.045 (3)	173

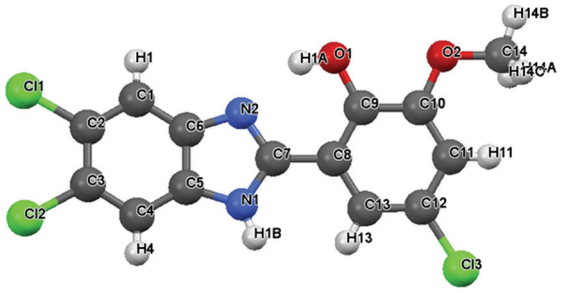

Fig. 1. Molecular structure of **HL$_{18}$** showing the atom numbering scheme.

General properties

In this study, twenty 5,6-dichlorobenzimidazolyl-phenol derivatives were obtained, eighteen of which are reported here for the first time. In addition, five

related transition metal complexes were obtained by allowing **HL_1** to react with Co(II), Ni(II), Cu(II), Zn(II) and Pd(II) ions at a mole ratio of 1:2 metal:ligand. This ratio is 1:1 in the Zn(II) complex obtained and 1:2 in the others. Despite many attempts, no single crystal sample suitable for X-ray study could be obtained from the complexes.

The molar conductivity values of all complexes in DMF are below 50 S m^2 mol^{-1}, and these values indicate non-ionic structures according to Geary.[36]

The magnetic moment value of the Ni(II) complex was found to be 2.05 μ_B, which is lower than the 2.83 μ_B expected for octahedral or tetrahedral geometries, which are paramagnetic structures that the d^8 ion with two unpaired electrons may have. Such low values are generally thought to be due to the distorted geometry between the tetrahedral and square planar systems, called quasi-tetrahedral.[37] The magnetic moment value found as 3.47 μ_B for the Co(II) complex can be considered as evidence that the five-coordinated d^7 complex is in a high-spin structure (three unpaired electrons). The geometry of the central ion may be octahedral. The magnetic moment value of the Cu(II) complex at room temperature was found to be 1.62 μ_B, indicating the formation of a monomeric complex. Although this value is lower than the theoretical value of 1.71 μ_B for the Cu(II) ion with d^9 electronic configuration, it remains within acceptable limits due to the influence of various factors.

FT-IR spectra

FT-IR spectral data are given in the Supplementary material (for **HL_1**–**HL_{20}**). In the IR spectra of most of the benzimidazolyphenol derivatives, strong or medium bands are seen in the range of 3243–3420 cm^{-1}. These bands are related to the combination of ν(O–H) and ν(N–H) frequencies and arises from the formation of intramolecular hydrogen bonding between C=N nitrogen and OH hydrogen atoms.[38,39] This band observed at 3333 cm^{-1} in **HL_1** disappeared as a result of the coordination of phenolic oxygen atom with the formation of the complexes.[40]

The stretching and out-of-plane bending modes (ν(C–H) and δ(C–H)) of the aromatic rings are detected at the 3117–3042 cm^{-1} and 870–800 cm^{-1} wavenumber regions, respectively, for all the compounds. The stretching frequencies of the aromatic C=C and the imidazole C=N groups are identified at the ranges of 1577––1609 cm^{-1} and 1614–1657 cm^{-1}, respectively, as expected. In the spectra of **HL_1**, the medium band at 1256 cm^{-1} can be assigned to ν(C–O) of the phenolic group and it shifted to the range of 1233–1246 cm^{-1} in the complexes as a result of the phenolic oxygen atom coordination. The bands of ν(C–O) were determined in the range of 1182–1273 cm^{-1} in the spectra of other benzimidazolylphenol derivatives (**HL_2**–**HL_{20}**).

The C–Cl stretching vibrations are seen at the range of 710–796 cm^{-1} as medium bands in all of the compounds.[41] In the iodine-containing compounds, **HL_5** and **HL_{17}**, the C–I vibrations bond can be detected around 550 cm^{-1}; in the bromine-containing compounds, **HL_3**, **HL_{13}**, **HL_{16}**, **HL_{19}** and **HL_{20}**, the medium bands between 550 and 600 cm^{-1} can be attributed to ν(C–Br). The ν(C–F) is expected to give a band above 1000 cm^{-1} in derivatives containing fluorine atom (**HL_2**, **HL_{13}** and **HL_{14}**); however it is difficult to detect the band of this bond due to interference with the vibrations of other bonds.[42]

The emergence of new bands of medium intensity around 503 cm^{-1} can be assigned to the ν(M–OC) vibration frequencies resulting from phenolic oxygen atom coordination.[43] It was evaluated that the new bands appearing in the complexes between 443–462 cm^{-1} belong to the stretching vibration mode of the M←N bond formed as a result of the coordination of the C=N nitrogen atom.[44] The coordination of the C=N nitrogen atom can also be associated with the shift of the 1639 cm^{-1} band of the ligand to the lower wavenumbers in the IR spectra of the complexes to 1602–1620 cm^{-1} range. The broad bands with medium characteristics between 3365 and 3225 cm^{-1} in the complexes mightily support the presence of the H_2O molecules.

It is known that the keto-enol structure is found in benzimidazolylphenol type compounds.[16] According to the IR spectral data, **HL_3**, **HL_4**, **HL_{12}**–**HL_{15}**, **HL_{17}** and **HL_{20}** compounds also have keto form in the solid state (Fig. 2). In other words, these compounds exist as a mixture of the keto and enol form. The weak or medium bands at 1662–1723 cm^{-1} range are considered to arise from the C=O bond in the keto form of the compounds in the solid state.

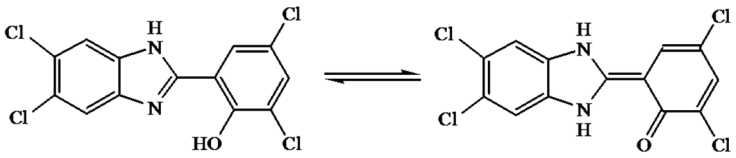

Fig. 2. Keto-enol tautomer structures of **HL_{15}**.

NMR spectra

^{1}H-NMR spectral data of **HL_1**–**HL_{20}** and the diamagnetic complexes are given in the Supplementary material. In the ^{1}H-NMR spectra of the compounds, signals of the NH and OH protons were detected at the 13.88–11.64 ppm range, and aromatic ring protons appeared in the range of 7.0 to 8.5 ppm. In ^{1}H-NMR spectra, whether salicylic OH protons are removed or not can be evaluated in relation to whether complexation occurs via the oxygen atom. Indeed, the absence of OH proton in both Zn(II) and Pd(II) complexes of **HL_1** shows that phenolic proton is removed and the oxygen atom is coordinated. While the chemical shift

values of the ligand protons in Pd(II) complex were detected at significantly higher ppm values (downfield shift), the shifts in Zn(II) complex were observed to be weaker compared to the Pd(II) complex, albeit in the same direction.

Although the keto form of some benzimidazolylphenols is dominant in the solid state according to IR data, the detection of OH protons shows that the enol structure is dominant in DMSO (or organic solvents) in the NMR spectra of all benzimidazolylphenol derivatives.

Thermogravimetric analysis (TGA)

Thermal analysis data of the complexes are given in the Supplementary material to this paper. The samples were heated from room temperature up to 800 °C in air atmosphere. Thermogravimetric analysis values provide important clues, especially explaining the status of H_2O molecules. It is known that lattice H_2O molecules removed up to 100 °C and coordinated H_2O molecules up to 200 °C. The 5.7 % mass loss seen in thermal analysis of the Co(II) complex around 150 °C can be considered as an indication of presence of two moles of coordinated H_2O considering the fact that two moles of H_2O in the complex corresponds to a theoretical mass of 5.5 %. The mass losses of 5.8 and 5.4 % in Ni(II) and Pd(II) complexes up to 100 °C, respectively, can be explained by the presence of two moles of lattice H_2O in both complexes (theoretical values are 5.5 and 5.15 % for Ni(II) and Pd(II) complexes, respectively). In addition, the absence of significant mass loss in these complexes between 100 and 200 °C (0.2 and 0.3 %, respectively for Ni(II) and Pd(II) complexes) can be attributed to the absence of coordinated H_2O molecules. In the Zn(II) complex, the mass losses of 8.6 % up to 100 °C and 4.3 % between 100 and 200 °C are evaluated to be related to two moles lattice and one mole coordinated H_2O molecules, respectively.

According to TGA data, the Zn(II) complex begins to decompose above 200 °C and the others above 300 °C. The different thermal behavior of the Zn(II) complex may be related to its different M:L ratio from the others with a ratio of 1:1. The fact that a greater mass loss occurs in the Zn(II) complex above 200 °C, unlike the others, can be interpreted that the chlorine atom starts leaving as HCl complex around this temperature and is completely removed up to 300 °C (totally 25.1 % mass loss).

It is possible to suggest that above 500 °C all complexes are completely decomposed and metal oxide forms begin to form. The mass ratios remaining from the complexes after complete dissociation are consistent with the theoretical mass ratios calculated for metal oxides.

Fluorescence spectra

The emission maximum data of the compounds are given in the Supplementary material. It was observed that $\mathbf{HL_1}$ emits strong fluorescence at 466 nm.

Among the compounds, the highest emission spectrum wavelength belongs to **HL$_9$** (4-methoxy derivative), which has dual fluorescence characteristic, with a value of 508 nm. **HL$_9$** also emits strongly at 389 nm. The lowest emission spectrum wavelength belongs to **HL$_8$** (5-methoxy derivative) with a value of 452 nm (Fig. 3). **HL$_6$**, which has a chlorine substitution at 2-position on the phenol ring, is another compound that exhibits a lower emission wavelength (blueshift) according to **HL$_1$**, with a value of 463 nm. A redshift effect is observed in all compounds except **HL$_6$** and **HL$_8$**. Based on these observations, it can be concluded that substitutions generally cause redshift.

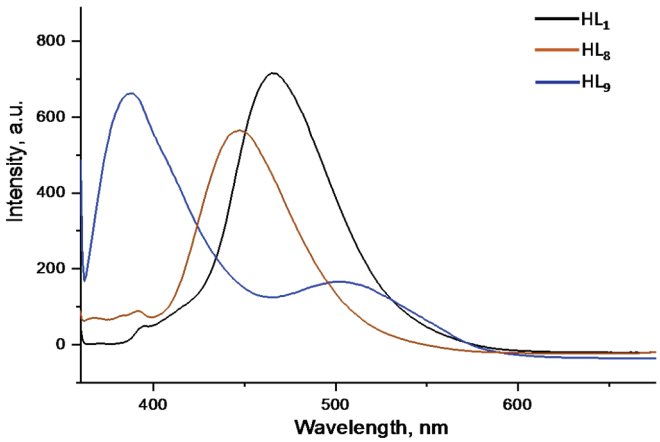

Fig. 3. Comparative fluorescence spectra of **HL$_1$** and its derivatives with the lowest and highest emission wavelength values.

While there is no significant shift in the complexes relative to the ligand, there is a significant decrease (or quenching effect) in the fluorescence intensity. The Zn(II) complex, which emits light at 450 nm, differs from the others by showing a red shift. It is also worth noting that the decrease in fluorescence intensity in the Cu(II) complex is greater than the others (Fig. 4).

Considering all the analytical, physicochemical and spectroscopic data described above, the proposed structures in Fig. 5 can be suggested for the complexes.

Antimicrobial activity

The results of the in vitro antibacterial and antifungal activities of the compounds and the values of the antibiotic and antifungal drugs given for comparison are presented in Table III as minimum inhibitory concentration (*MIC*).

When the Table III is examined, it is noted that the first eleven compounds (**HL$_1$** to **HL$_{11}$**) show higher activity when compared to the other compounds and selective activity against some microorganisms. The common feature of these compounds is that they are all mono substituted derivatives of **HL$_1$**. It can be said

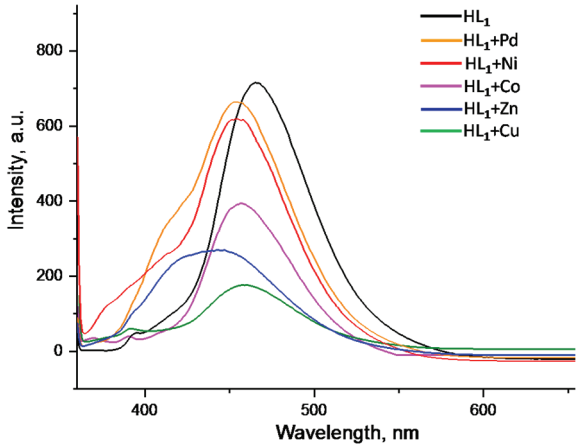

Fig. 4. The comparative fluorescence spectra of **HL_1** and its complexes.

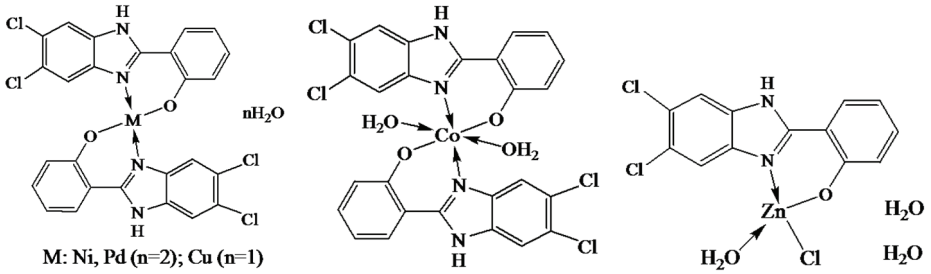

Fig. 5. Suggested coordinations for the complexes in the study.

that all mono substituted derivatives show selective activity especially against Gram-positive bacteria, *S. aureus* and *S. epidermidis*. The activity of **HL_7** (6′--methoxy derivative) against *S. epidermidis* is remarkable with 9.75 μg mL^{-1}. However, another noteworthy finding is that disubstituted derivatives of **HL_1** (**HL_{12}** to **HL_{20}**) are also moderately or weakly effective against all microorganisms (non-selective general activity).

TABLE III. *In vitro* antimicrobial activity of the compounds (*MIC* / μg mL^{-1}); *Sa* – *Staphylococcus aureus* ATCC 29213; *Se* – *Staphylococcus epidermidis* ATCC 12228; *Ec* – *Escherichia coli* ATCC 25922; *Kp* – *Klebsiella pneumoniae* ATCC 4352; *Pa* – *Pseudomonas aeruginosa* ATCC 27853; *Pm* – *Proteus mirabilis* ATCC 14153; *Ca* – *Candida albicans* ATCC 10231; *Cp* – *Candida parapsilosis* ATCC 22019; *Ct* – *Candida tropicalis* ATCC 750; references: ciprofloxacin and amphotericin B were used for bacteria and fungi, respectively

Compound	Microorganism								
	Sa[a]	*Se*[a]	*Ec*[b]	*Kp*[b]	*Pa*[b]	*Pm*[b]	*Ca*	*Cp*	*Ct*
HL_1	**19.5**	**39**	78	625	–[c]	312	–	625	625
HL_2	**19.5**	156	312	156	–	312	–	**39**	625
HL_3	**19.5**	156	312	625	–	312	–	156	625

TABLE III. Continued

Compound	Microorganism								
	Sa[a]	*Se*[a]	*Ec*[b]	*Kp*[b]	*Pa*[b]	*Pm*[b]	*Ca*	*Cp*	*Ct*
HL_4	**39**	**39**	625	156	–	625	–	312	312
HL_5	156	312	625	625	625	312	625	1250	1250
HL_6	78	156	156	156	–	156	**39**	156	312
HL_7	156	**9.75**	312	625	–	312	–	312	312
HL_8	156	156	312	312	–	625	–	312	625
HL_9	156	78	156	625	–	312	–	625	625
HL_{10}	**19.5**	78	312	156	–	625	–	312	625
HL_{11}	**39**	**19.5**	156	312	–	312	–	156	625
HL_{12}	156	312	625	625	1250	625	1250	1250	1250
HL_{13}	312	156	625	625	625	625	1250	1250	625
HL_{14}	312	156	1250	625	1250	625	1250	625	625
HL_{16}	156	312	1250	625	1250	312	1250	625	625
HL_{16}	312	156	1250	1250	1250	312	1250	1250	625
HL_{17}	156	156	625	625	1250	312	625	625	1250
HL_{18}	312	312	625	625	1250	625	1250	1250	1250
HL_{19}	156	156	625	625	1250	625	625	625	1250
HL_{20}	312	156	625	1250	1250	625	625	1250	1250
HL_1+Co(II)	625	312	1250	625	625	625	625	625	1250
HL_1+Ni(II)	312	312	1250	1250	1250	312	1250	1250	1250
HL_1+Cu(II)	312	312	1250	625	1250	312	625	1250	625
HL_1+Zn(II)	156	156	2500	1250	1250	312	1250	625	1250
HL_1+Pd(II)	625	156	625	1250	625	312	1250	625	1250
References	0.25	0.0625	0.0156	0.0078	1.0	0.0156	0.5	1.0	1.0

[a]Gram-positive; [b]Gram-negative; [c]no antimicrobial effect at 5000 μg mL^{-1} and lower dilutions

In our previous studies, it was determined that various benzimidazole derivatives exhibited selective activity, particularly against Gram-positive bacteria and some fungal species.[18,45] It was observed that benzimidazolyphenol derivatives containing methoxy and nitro/bromine/chlorine groups were distinguished from others by their activity against Gram-positive bacteria such as *S. aureus* and also *C. albicans*.[41]

No significant antimicrobial activity was detected in the complexes according to the ligand. The only striking feature is that the complexes showed slightly higher antifungal activity against *C. albicans*, where the ligand showed no activity. It can be assumed that the complexes form stable chelates with the ligands at an 1:2 M:L ratio, thus limiting the activity of the ligands and therefore lowering the activity compared to the ligand. The relatively high activity of the Zn(II) complex, with a 1:1 M:L ratio, against Gram-positive bacteria may be attributable to its structural feature. A possible mechanism is that the Zn(II) complex, thought to bind one mole of water, releases water upon contact with bacteria and binds to their proteins.

CONCLUSION

In this study, 2-(5,6-dichloro-1*H*-benzimidazol-2-yl)phenol (**HL_1**) and its nineteen derivatives with different substituents on the phenol ring were obtained and their structural properties were investigated. Structure of **HL_{18}** was investigated by X-ray single crystal spectroscopy, also. Additionally, M(II) complexes (M: Co, Ni, Cu, Zn and Pd) of **HL_1** were obtained and various physicochemical and spectroscopic properties were investigated. It was found that all complexes have non-electrolytic properties and the M:L ratios are 1:1 in the Zn(II) complex and 1:2 in the other complexes. Fluorescence spectral studies show that in all compounds except HL_6 and HL_8, the substitution results in a shift of the fluorescence emission to lower wavelengths (redshift) compared to **HL_1**. The zinc(II) complex showed a greater redshift effect compared to the other complexes. After characterization, antibacterial and antifungal activity of all the compounds was evaluated against six bacteria and three fungi. Compounds **HL_1** to **HL_{11}** (**HL_1** and its monosubstituted derivatives) show better compared to the other compounds and selective activity against some microorganisms. Another noteworthy result is that the complexes of **HL_1** show weak activity against *C. albicans*, against which **HL_1** itself is inactive. It was observed that the Zn(II) complex showed relatively higher activity against *S. aureus* and *S. epidermidis* (Gram-positive bacteria) compared to the other complexes.

SUPPLEMENTARY MATERIAL

Additional data and information are available electronically at the pages of journal website: https://www.shd-pub.org.rs/index.php/JSCS/article/view/13486, or from the corresponding author on request.

Acknowledgement. This work was supported by Scientific Research Projects Coordination Unit of Istanbul University-Cerrahpasa, Project number: 24777.

ИЗВОД

СПЕКТРАЛНА КАРАКТЕРИЗАЦИЈА И ИСПИТИВАЊЕ АНТИМИКРОБНЕ АКТИВНОСТИ 5,6-ДИХЛОРО-1*H*-БЕНЗИМИДАЗОЛ-2-ИЛ-(4'/5'/6'-СУПСТИТУИСАНИХ)ФЕНОЛА (**HL_1**–**HL_{20}**) И Co(II), Ni(II), Cu(II), Zn(II) И Pd(II) КОМПЛЕКСА СА **HL_1**

AYDIN TAVMAN[1], DEMET GURBUZ[2], MAYRAM HACIOGLU[3], ADEM CINARLI[2], ONUR SAHIN[4] и A. SEHER BIRTEKSOZ TAN[3]

[1]Istanbul University-Cerrahpaşa, Faculty of Engineering, Department of Chemistry, Inorganic Chemistry Division, 34320 Avcilar, Istanbul, Türkiye, [2]Istanbul University-Cerrahpaşa, Faculty of Engineering, Department of Chemistry, Organic Chemistry Division, 34320 Avcilar, Istanbul, Türkiye, [3]Istanbul University, Faculty of Pharmacy, Department of Pharmaceutical Microbiology, 34452 Beyazit, Istanbul, Türkiye и [4]Sinop University, Faculty of Health Sciences, Department of Occupational Health and Safety, 57000 Sinop, Türkiye

5,6-Дихлоро-1*H*-бензимидазол-2-ил-(4'/5'/6'-супституисани)феноли (**HL_1**–**HL_{20}**) и MCl_2 комплекси (M: Co, Ni, Cu, Zn, Pd) са **HL_1** синтетисани су и окарактерисани разли-

читим физичко–хемијским и спектроскопским методама, као што су елементална анализа, термогравиметријска анализа, FTIR, NMR и флуоресцентна спектроскопија. Структуре комплекса потврђене су и мерењем моларне проводљивости и магнетног момента. **HL₁** једињење се координовало као бидентатни, монобазни хелатни лиганд са NO донорским атомима у свим комплексима. Утврђено је да су сви комплекси неелектролити, при чему је однос метала и лиганда (M:L) 1:1 у Zn(II) комплексу и 1:2 у осталим комплексима. Кристална структура **HL₁₈** је, такође, испитивана, при чему је у оба молекула уочено присуство интра- и интермолекулских водоничних веза. На основу података добијених флуоресцентном спектроскопијом, супституенти у положају 4 изазвали су померање максимума емисије ка нижим таласним дужинама (црвено померање) у поређењу са **HL₁**, док су супституенти у положају 3 и 5 узроковали плаво померање. Zn(II) комплекс је показао израженије црвено померање у односу на друге комплексе. Поред тога, антимикробна активност једињења је испитивана према шест бактеријских и три гљивичне врсте. Примећено је да **HL₁** и његови моносупституисани деривати (**HL₁**–**HL₁₁**) показују селективну активност, посебно према Грам-позитивним бактеријама *S. aureus* и *S. epidermidis*. Zn(II) комплекс је показао релативно већу активност према Грам-позитивним бактеријама у поређењу са осталим комплексима.

(Примљено 6. августа, ревидирано 12. октобра, прихваћено 29. октобра 2025)

REFERENCES

1. M. Rasschaert, D. Schrijvers, J. van den Brande, J. Dyck, J. Bosmans, K. Merkle, J. B. Vermorken, *Br. J. Cancer* **96** (2007) 1692 (https://doi.org/10.1038/sj.bjc.6603776)
2. M. Montillo, F. Ricci, A. Tedeschi, E. Vismara, E. Morra, *Expert Rev. Hematol.* **3** (2010) 131 (https://doi.org/10.1586/ehm.10.7)
3. C. S. P. Sastry, P. Y. Naidu, S. S. N. Murty, *Talanta* **44** (1997) 1211 (https://doi.org/10.1016/S0039-9140(97)83117-7)
4. C. Delescluse, M. P. Piechock, N. Ledirac, R. H. Hines, R. Li, X. Gidrol, R. Rahmani, *Biochem. Pharmacol.* **61** (2001) 399 (https://doi.org/10.1016/S0006-2952(00)00562-1)
5. K. K. Mothilal, C. Karunakaran, A. Rajendran, R. Murugesan, *J. Inorg. Biochem.* **98** (2004) 322 (https://doi.org/10.1016/j.jinorgbio.2003.10.017)
6. E. J. Cardoso, A. F. Luna, J. P. Urizar, *Acta Tropica* **92** (2004) 237 (https://doi.org/10.1016/j.actatropica.2004.08.003)
7. M. Savlik, P. Polaskova, B. Szotakova, J. Lamka, L. Skalova, *Res. Vet. Sci.* **79** (2005) 139 (https://doi.org/10.1016/j.rvsc.2004.10.007)
8. R. G. Almeida, J. C. Florio, H. S. Spinosa, M. M. Bernardi, *Neurotoxicol. Teratol.* **24** (2002) 255 (https://doi.org/10.1016/S0892-0362(02)00203-9)
9. J. Gronvold, T. S. Svendsen, H. O. Kraglund, J. Bresciani, J. Monrad, *Vet. Parasitol.* **124** (2004) 91 (https://doi.org/10.1016/j.vetpar.2004.06.003)
10. B. Pathare, T. Bansode, *Results Chem.* **3** (2021) 100200 (https://doi.org/10.1016/j.rechem.2021.100200)
11. S. R. Brishty, M. J. Hossain, M. U. Khandaker, M. R. I. Faruque, H. Osman, S. M. A. Rahman, *Front. Pharmacol.* **12** (2021) 762807 (https://doi.org/10.3389/fphar.2021.762807)
12. G. R. Morais, E. Palma, F. Marques, L. Gano, M. C. Oliveira, A. Abrunhosa, H. V. Miranda, A. Paulo, T. F. Outeiro, I. Santos, *J. Heterocycl. Chem.* **54** (2015) 255 (https://doi.org/10.1002/jhet.2575)
13. R. Sharma, A. Bali, B. Chandhari, *Bioorg. Med. Chem. Lett.* **27** (2017) 3007 (https://doi.org/10.1016/j.bmcl.2017.05.017)

14. A. S. Alpan, S. Parlar, L. Carlino, A. H. Tarikogullari, V. Alptüzün, H. S. Güneş, *Bioorg. Med. Chem.* **21** (2013) 4928 (https://doi.org/10.1016/j.bmc.2013.06.065)
15. R. Bonnett, *Chem. Rev.* **63** (1963) 573 (https://doi.org/10.1021/cr60226a002)
16. W. Y. Zhu, K. Liu, X. Zhang, *Sens. Diagn.* **2** (2023) 665 (https://doi.org/10.1039/D3SD00020F)
17. R. Sathyanarayana, V. Kumar, G. H. Pujar, B. Poojary, M. K. Shankar, S. Yallappa, *J. Photochem. Photobiol., A* **402** (2020) 112751 (https://doi.org/10.1016/j.jphotochem.2020.112751)
18. A. Tavman, D. Gürbüz, A. A. Karaçelik, D. N. Çolak, D. Efe, A. Cinarli, *Rev. Roum. Chim.* **69** (2024) 201 (https://doi.org/10.33224/rrch.2024.69.3-4.10)
19. A. Tavman, I. Boz, A. S. Birteksöz, *Spectrochim. Acta, A* **77** (2010) 199 (https://doi.org/10.1016/j.saa.2010.05.008)
20. A. Tavman, I. Boz, A. S. Birteksöz, A. Cinarli, *J. Coord. Chem.* **63** (2010) 1398 (https://doi.org/10.1080/00958971003789835)
21. A. Tavman, D. Gürbüz, S. Oksüz, A. Cinarli, *Mor. J. Chem.* **6** (2018) 328 (https://doi.org/10.48317/IMIST.PRSM/morjchem-v6i2.7909)
22. L. Wang, C. X. Zhang, J. Q. Zhao, *Chinese J. Struct. Chem.* **33** (2014) 1479 (https://caod.oriprobe.com/articles/43884889/Synthesis__Structure_and_Catalytic_Activity_of_a_M.htm)
23. M. Haghverdi, A. Tadjarodi, N. Bahri-Laleh, M. N. Haghighi, *J. Coord. Chem.* **71** (2018)1180 (https://doi.org/10.1080/00958972.2018.1446527)
24. M. Haghverdi, A. Tadjarodi, N. Bahri-Laleh, M. N. Haghighi, *Appl. Organomet. Chem.* **32** (2018) e4015 (https://doi.org/10.1002/aoc.4015)
25. T. K. C. Huynh, T. H. A. Nguyen, T. C. T. Nguyen, T. K. D. Hoang, *RSC Adv.* **10** (2020) 20543 (https://doi.org/10.1039/D0RA02282A)
26. M. M. Karpinska, J. Matysiak, A. Niewiadomy, *Arch. Pharm. Res.* **34** (2011) 1639 (https://doi.org/10.1007/s12272-011-1008-0)
27. H. F. Ridley, G. W. Spickett, G. M. Timmis, *J. Het. Chem.* **2** (1965) 453 (https://doi.org/10.1002/jhet.5570020424)
28. Z. Karimi-Jaberi, M. Amir, *J. Chem.* **9** (2012) 167 (https://doi.org/10.1155/2012/793978)
29. *M27-A3: Reference Method for Broth Dilution Antifungal Susceptibility Testing of Yeasts*, Approved Standard, 3rd ed., Clinical and Laboratory Standards Institute, Wayne, PA, 2012
30. *M100-Ed.31: Performance Standards for Antimicrobial,* Clinical and Laboratory Standards Institute, Wayne, PA, 2021
31. G. M. Sheldrick, *Acta Cryst., A* **64** (2008) 112 (https://doi.org/10.1107/S0108767307043930)
32. G. M. Sheldrick, *Acta Cryst., C* **71** (2015) 3 (https://doi.org/10.1107/S2053229614024218)
33. APEX2, Bruker AXS Inc., Madison, WI, 2013
34. C. F. Macrae, I. J. Bruno, J. A. Chisholm, P. R. Edgington, P. McCabe, E. Pidcock, L. Rodriguez-Monge, R. Taylor, J. van de Streek, P. A. Wood, *J. Appl. Cryst.* **41** (2008) 466 (https://doi.org/10.1107/S0021889807067908)
35. L. J. Farrugia, *J. Appl. Cryst.* **45** (2012) 849 (https://doi.org/10.1107/S0021889812029111)
36. W. Geary, *Coord. Chem. Rev.* **7** (1971) 81 (https://doi.org/10.1016/S0010-8545(00)80009-0)

37. D. Lomjanský, C. Rajnák, J. Titis, J. Monco, L. Smolko, R. Boča, *Inorg. Chim. Acta* **483** (2018) 352 (https://doi.org/10.1016/j.ica.2018.08.029)
38. A. Tavman, *Spectrochim. Acta, A* **63** (2006) 343 (https://doi.org/10.1016/j.saa.2005.05.020)
39. D. Kanamori, Y. Yamada, A. Onoda, T. A. Okamura, S. Adachi, H. Yamamoto, N. Ueyama, *Inorg. Chim. Acta* **358** (2005) 331 (https://doi.org/10.1016/j.ica.2004.09.014)
40. V. M. Leovac, L. S. Jovanović, V. S. Čečljević, L. J. Bjwlica, V. B. Arion, N. V. Gerbelu, *Polyhedron* **13** (1994) 3005 (https://doi.org/10.1016/S0277-5387(00)83421-X)
41. N. Sundaraganesan, C. Meganathan, B. Anand, C. Lapouge, *Spectrochim. Acta, A* **66** (2007) 773 (https://doi.org/10.1016/j.saa.2006.04.025)
42. D. Mahadevan, S. Periandy, M. Karabacak, S. Ramalingam, *Spectrochim. Acta, A* **82** (2011) 481 (https://doi.org/10.1016/j.saa.2011.07.082)
43. P. E. Kazin, M. A. Pogosova, L. A. Trusov, I. V. Kolesnik, O. V. Magdysyuk, R. E. Dinnebier, *J. Solid State Chem.* **237** (2016) 349 (https://doi.org/10.1016/j.jssc.2016.03.004)
44. K. Nakamoto, *Infrared and Raman Spectra of Inorganic and Coordination Compounds, Part B*, 5th ed., John Wiley & Sons, New York, 1997
45. A. *Tavman*, A. Z. Elmal, D. Gürbüz, M. Hacioglu, A. S. Birteksöz Tan, A. Cinarli, *Rev. Roum. Chim.* **68** (2023) 49 (https://doi.org/10.33224/rrch.2023.68.1-2.05).

Journal of the Serbian Chemical Society
JSCS@tmf.bg.ac.rs • www.shd.org.rs/JSCS
J. Serb. Chem. Soc. 90 (2) S54–S60 (2025) *Supplementary material*

SUPPLEMENTARY MATERIAL TO

Spectral characterization and antimicrobial activity studies of 5,6-dichloro-1*H*-benzimidazol-2-yl-(4'/5'/6'-substituted)-phenols (HL_1–HL_{20}) and Co(II), Ni(II), Cu(II), Zn(II) and Pd(II) complexes of HL_1

AYDIN TAVMAN[1]*, DEMET GURBUZ[2], MAYRAM HACIOGLU[3], ADEM CINARLI[2], ONUR SAHIN[4] and A. SEHER BIRTEKSOZ TAN[3]

[1]Istanbul University-Cerrahpaşa, Faculty of Engineering, Department of Chemistry, Inorganic Chemistry Division, 34320 Avcilar, Istanbul, Türkiye, [2]Istanbul University-Cerrahpaşa, Faculty of Engineering, Department of Chemistry, Organic Chemistry Division, 34320 Avcilar, Istanbul, Türkiye, [3]Istanbul University, Faculty of Pharmacy, Department of Pharmaceutical Microbiology, 34452 Beyazit, Istanbul, Türkiye, and [4]Sinop University, Faculty of Health Sciences, Department of Occupational Health and Safety, 57000 Sinop, Türkiye

J. Serb. Chem. Soc. 90 (2) (2025) 113–127

EXPERIMENTAL

Chemistry and apparatus

All chemicals and solvents were of reagent grade and they were used without further purification.

Analytical data were obtained with a Thermo Finnigan Flash EA 1112 analyzer. Melting points were determined using a Buchi M-560 melting-point apparatus. Molar conductivity of the complexes was measured on a WTW Cond315i conductivity meter in DMF at 25 °C. Magnetic measurements: MK1 Sherwood Scientific apparatus (at room temperature by Gouy's method). NMR spectra were run on a Varian Unity Inova 500 NMR spectrometer. FT-IR spectra were recorded on a Bruker Optics Vertex 70 spectrometer using Attenuated Total Reflection (ATR) techniques between 400 and 4000 cm^{-1}. The Electron Spray Ionization-Mass Spectrometry (ESI-MS) analysis was carried out in positive ion modes using a Thermo Finnigan LCQ Advantage MAX LC/MS/MS. Fluorescence spectra were performed on a Shimadzu RF-5301 PC Spectrofluorophotometer in EtOH (c = ~1×10^{-4} mol L^{-1}).

$[Co(\mathbf{L_1})_2(H_2O)_2]$: Light brown solid. Yield: 71 %; dec. p.: 168 °C; Combustion analysis for $C_{26}H_{18}Cl_4N_4O_4Co$ (FW: 651.19): Calculated. C 47.95, H 2.79, N 8.60; found C 48.42, H 3.04, N 8.48. Magnetic moment, μ_{eff}: 3.47μ_B. Λ_M (DMF, 25 °C, S m^2 mol^{-1}): 21.3. IR (ATR, cm^{-1}): 3225m,br ν(H_2O+NH), 3107m ν$(CH)_{ar.}$,1607m ν(C=N), 1599m ν(C=C), 1485m, 1453m, 1372m, 1245m ν(C–O), 1098m, 960m, 864m δ$(CH)_{ar.}$, 813m, 751s ν(C–Cl), 677m, 578m, 545m, 502m ν(Co–O), 462m ν(Co←N), 428m. TGA (t / °C: weight loss, %): 100: 1.1; 150: 5.7; 200: 6.7; 300: 19.4; 400: 53.1; 500: 85.2; 600: 87.5; 700: 89.1; 800: 89.1 (Theoretical value of CoO: 11.5 %). Fluorescence spectra (EtOH, c = 1×10^{-4} mol L^{-1}, λ_{max}/ nm): 469m.

* Corresponding author. E-mail: atavman@iuc.edu.tr

[Ni($\mathbf{L_1}$)$_2$]·2H$_2$O: Light brown solid. Yield: 73 %; dec. p.: 165 °C; Combustion analysis for $C_{26}H_{18}Cl_4N_4O_4Ni$ (FW: 650.95): Calculated. C 47.97, H 2.79, N 8.61; found C 48.33, H 2.96, N 8.44. Magnetic moment, $\mu_{eff.}$: 2.05 μ_B. Λ_M (DMF, 25 °C, S m^2 mol^{-1}): 31.5. IR (ATR, cm^{-1}): 3356m ν(OH), 3269m ν(NH), 3068m ν(CH)$_{ar.}$, 1609m ν(C=N), 1595m ν(C=C), 1503m, 1456m, 1387m, 1246m ν(C–O), 1103m, 1039m, 854m δ(CH)$_{ar.}$, 815m, 754s ν(C–Cl), 680m, 616m, 537m, 504m ν(Ni–O), 449m ν(Ni←N), 416m. TGA (t / °C: weight loss, %): 100: 5.8; 150: 6.0; 200: 6.5; 300: 18.2; 400: 51.6; 500: 86.5; 600: 88.2; 700: 88.8; 800: 88.8 (Theoretical value of NiO: 11.5 %). Fluorescence spectra (EtOH, c = 1×10^{-4} mol L^{-1}, λ_{max}/ nm): 417sh, 462m.

[Cu($\mathbf{L_1}$)$_2$]·H$_2$O: Brown solid. Yield: 80 %; dec. p.: 332 °C; Combustion analysis for $C_{26}H_{16}Cl_4N_4O_3Cu$ (FW: 637.80): Calculated. C 48.96, H 2.53, N 8.78; found C 48.60, H 2.54, N 8.41. Magnetic moment, $\mu_{eff.}$: 1.62 μ_B. Λ_M (DMF, 25 °C, S m^2 mol^{-1}): 7.1. IR (ATR, cm^{-1}): 3357m,br ν(H$_2$O+NH), 3130m,br, 3054w ν(CH)$_{ar.}$, 1617m ν(C=N), 1588m ν(C=C), 1556m, 1451m, 1355m, 1244sν(C–O), 1197m, 1100m, 975m, 868m δ(CH)$_{ar.}$, 759m, 742m ν(C–Cl), 691m, 573m, 546m, 503m ν(Cu–O), 443m ν(Cu←N), 420m. TGA (t / °C: weight loss, %): 100: 2.7; 150: 3.3; 200: 6.3; 300: 18.0; 400: 49.5; 500: 85.5; 600: 87.3; 700: 87.5; 800: 87.7 (Theoretical value of CuO: 12.5 %). Fluorescence spectra (EtOH, c = 1×10^{-4} mol L^{-1}, λ_{max}/ nm): 469w,br.

[Zn($\mathbf{L_1}$)Cl(H$_2$O)]·2H$_2$O: Dirty white solid. Yield: 71 %; dec.p.: 270 °C; Combustion analysis for $C_{13}H_{13}Cl_3N_2O_4Zn$ (FW: 433.02): Calculated. C 36.06, H 3.03, N 6.47; found C 35.84, H 2.88, N 6.32. Λ_M (DMF, 25 °C, S m^2 mol^{-1}): 45.8. IR (ATR, cm^{-1}): 3365m,br ν(OH), 3203m,br ν(NH), 3042w ν(CH)$_{ar.}$, 1620m ν(C=N), 1609m ν(C=C), 1558m, 1483m, 1456m, 1321m, 1233s ν(C–O), 1147m, 969m, 856m δ(CH)$_{ar.}$, 740s ν(C–Cl), 692m, 577m, 541s, 505m ν(Zn–O), 443m ν(Zn←N), 421m. ^{1}H-NMR (500 MHz, DMSO-d$_6$, δ): 12.81 (*brs*, 1H, NH), 7.89 (*brs*, 2H, H4+H7), 7.84 (*dd*, 1H, J_1 = 7.9, J_2 = 1.6, H3'), 7.15 (*dt*, 1H, J_1 = 8.3, J_2 = 1.4, H4'), 6.71 (*dd*, 1H, J_1 = 7.7, J_2 = 3.7, H6'), 6.52 (*td*, 1H, J_1 = 7.2, J_2 = 7.1, J_3 = 1.2, H5'). TGA (t / °C: weight loss, %): 100: 8.6; 150: 11.7; 200: 16.4; 300: 25.1; 400: 53.5; 500: 79.4; 600: 82.2; 700: 82.4; 800: 82.5 (Theoretical value of ZnO: 18.8 %). Fluorescence spectra (EtOH, c = 1×10^{-4} mol L^{-1}, λ_{max}/ nm): 425sh, 450m,br.

[Pd($\mathbf{L_1}$)$_2$]·2H$_2$O: Soil colored solid. Yield: 66 %; dec. p. >350 °C; Combustion analysis for $C_{26}H_{18}Cl_4N_4O_4Pd$ (FW: 698.70): Calculated. C 44.41, H 3.01, N 7.21; found C 44.70, H 2.60, N 8.02. Λ_M (DMF, 25 °C, S m^2 mol^{-1}): 14.3. IR (ATR, cm^{-1}): 3269m,br ν(NH+OH$_2$), 3117w ν(CH)$_{ar.}$, 1602m ν(C=C), 1588m ν(C=N), 1531m, 1476m, 1310m, 1239s ν(C–O), 1144m, 1034m, 969m, 870m δ(CH)$_{ar.}$, 753s ν(C–Cl), 702m, 672m, 568m, 503m ν(Pd–O), 443m ν(Pd←N). ^{1}H-NMR (500 MHz, DMSO-d$_6$, δ): 13.43 (*s*, 1H, NH), 7.94 (*brs*, 1H, H7), 7.87 (*s*, 1H, H4), 7.68 (*dt*, 1H, J_1 = 8.0, J_2 = 1.7, H5'), 7.45 (*dt*, 1H, J_1 = 7.8, J_2 = 7.1, J_3 = 1.0, H4'), 7.22 (*d*, 1H, J = 7.6, H6'), 7.05 (*dt*, 1H, J_1 = 8.0, J_2 = 1.0, H3'). TGA (t / °C: weight loss, %): 100: 5.4; 150: 5.7; 200: 6.1; 300: 19.9; 400: 49.7; 500: 74.6; 600: 77.3; 700: 81.1; 800: 81.2 (Theoretical value of PdO: 17.5 %). Fluorescence spectra (EtOH, c = 1×10^{-4} mol L^{-1}, λ_{max}/ nm): 415sh, 459m.

*2-(5,6-Dichloro-1H-benzimidazol-2-yl)phenol (**HL$_1$**)*: Yield: 80 %. Slightly yellow solid. Decomposition point (Dec. p.): 331 °C. (+)ESI-MS (*m/z*): calculated for [$C_{13}H_8Cl_2N_2O$]$^+$ 279.1, observed 279.3 (100 %) and 281.3 for ([$C_{13}H_8Cl_2N_2O$ + 2H]$^+$ (73.9 %). Combustion analysis for $C_{13}H_8Cl_2N_2O$: Calculated. C 55.94, H 2.89, N 10.04; found C 56.15, H 3.03, N 9.97. IR (ATR): 3333m ν(NH+OH), 3101m ν(CH)$_{ar.}$, 1639m ν(C=N), 1600m ν(C=C), 1578m, 1487s, 1370m, 1256m ν(C–O), 1136m, 1106m, 960m, 865m δ(CH)$_{ar.}$, 739s ν(C–Cl), 678m, 580m, 553m, 422m, cm^{-1}. ^{1}H-NMR (500 MHz, DMSO-d$_6$, δ): 13.30 (*s*, 1H, NH), 12.42 (*s*, 1H, OH), 8.08 (*dd*, 1H, J_1 = 7.9, J_2 = 1.6, H3'), 8.00 (*brs*, 1H, H4), 7.84 (*brs*, 1H, H7), 7.41 (*dt*, 1H, J_1 =

1.6, J_2 = 7.2, J_3 = 8.4, H5'), 7.06 (*dd*, 1H, J_1 = 8.3, J_2 = 1.0, H6'), 7.03 (*dt*, 1H, J_1 = 7.6, J_2 = 1.1, H4'). Fluorescence spectra (λ_{max} / nm): 394w, 466s.

*2-(5,6-Dichloro-1H-benzimidazol-2-yl)-4-fluorophenol (**HL$_2$**)*: Yield: 71 %. Light yellow solid. Dec. p.: 352 °C. (+)ESI-MS (*m/z*): calculated for $[C_{13}H_7Cl_2FN_2O]^+$ 297.1, observed 297.3 (100 %) and 299.3 for $([C_{13}H_7Cl_2FN_2O + 2H]^+$ (66.0 %). Combustion analysis for $C_{13}H_7Cl_2FN_2O$: Calculated. C 52.55, H 2.37, N 9.43; found C 52.71, H 2.53, N 9.27. IR (ATR, cm^{-1}): 3341m ν(NH+OH), 3078m $\nu(CH)_{ar.}$, 1650m ν(C=N), 1600m ν(C=C), 1583m, 1498m, 1448m, 1304m, 1255m ν(C–O), 1168m, 1096m, 976m, 859m, 814s $\delta(CH)_{ar.}$, 780m, 743m ν(C–Cl), 665m, 561s, 470m, 443m, cm^{-1}. ^{1}H-NMR (500 MHz, DMSO-d_6, δ): 13.27 (*s*, 1H, NH), 12.21 (*s*, 1H, OH), 8.02 (*brs*, 1H, H4), 7.93 (*d*, 1H, J = 3.1, H3'), 7.91 (*brs*, 1H, H7), 7.28 (*dd*, 1H, J_1 = 9.0, J_2 = 3.1, H5'), 7.08 (d, 1H, J = 9.1, H6'). Fluorescence spectra (λ_{max} / nm): 393w, 480s.

*4-Bromo-2-(5,6-dichloro-1H-benzimidazol-2-yl)phenol (**HL$_3$**)*: Yield: 85 %. Yellowish grey solid. Dec. p.; 220 °C. (+)ESI-MS (*m/z*): calculated for $[C_{13}H_7BrCl_2N_2O + H]^+$ 359.0, observed 359.3 (100 %) and 357.3 for $([C_{13}H_7BrCl_2N_2O – H]^+$ (53.3 %). Combustion analysis for $C_{13}H_7BrCl_2N_2O$: Calculated. C 43.61, H 1.97, N 7.82; found C 43.45, H 1.91, N 7.74. IR (ATR, cm^{-1}): 3341m ν(NH+OH), 3075m $\nu(CH)_{ar.}$, 2960m,br, 1719m ν(C=O), 1620m ν(C=N), 1609m ν(C=C), 1482m, 1372m, 1249s ν(C–O), 1136m, 965m, 866m, 801s $\delta(CH)_{ar.}$, 739m ν(C–Cl), 632m, 565m ν(C–Br), 487m, 420m, cm^{-1}. ^{1}H-NMR (500 MHz, DMSO-d_6, δ): 13.31 (*brs*, 1H, NH), 12.51 (*brs*, 1H, OH), 8.16 (*d*, 1H, J = 2.4, H3'), 7.92 (*brs*, 2H, H4+H7), 7.43 (*dd*, 1H, J_1 = 8.8, J_2 = 2.4, H5'), 7.10 (*d*, 1H, J = 8.8, H6'). Fluorescence spectra (λ_{max} / nm): 393w, 474s.

*4-Chloro-2-(5,6-dichloro-1H-benzimidazol-2-yl)phenol (**HL$_4$**)*: Yield: 81 %. Yellowish grey solid. Dec. p.: 221 °C. (+)ESI-MS (*m/z*): calculated for $[C_{13}H_7Cl_3N_2O]^+$ 313.5, observed 313.2 (100 %) and 315.2 for $([C_{13}H_7Cl_3N_2O + 2H]^+$ (90.1 %). Combustion analysis for $C_{13}H_7Cl_3N_2O$: Calculated. C 49.79, H 2.25, N 8.93; found: C 49.64, H 2.16, N 8.80. IR (cm^{-1}): 3338m ν(NH+OH), 3077m $\nu(CH)_{ar.}$, 2960m,br, 1723m ν(C=O), 1621m ν(C=N), 1602m ν(C=C), 1576m, 1474m, 1444m, 1355m, 1278m, 1249m ν(C–O), 1136m, 1095m, 965m, 866m, 800m $\delta(CH)_{ar.}$, 745m ν(C–Cl), 720m ν(C–Cl), 648m, 564m, 543m, 490m, 420m, cm^{-1}. ^{1}H-NMR (500 MHz, DMSO-d_6, δ): 13.32 (*brs,* 1H, NH), 12.52 (*brs,* 1H, OH), 8.29 (*d,* 1H, J = 2.4, H3'), 8.01 (*brs*, 1H, H4), 7.88 (*brs*, 1H, H7), 7.54 (*dd,* 1H, J_1 = 8.8, J_2 = 2.4, H5'), 7.03 (*d,* 1H, J = 8.8, H6'). Fluorescence spectroscopy (λ_{max}/nm): 394w, 475m.

*2-(5,6-dichloro-1H-benzimidazol-2-yl)-4-iodophenol (**HL$_5$**)*: Yield: 65 %. Light orange solid. Dec. p.: 231 °C. (+)ESI-MS (*m/z*): calculated for $[C_{13}H_7Cl_2IN_2O]^+$ 405.1, observed 405.1 (100 %) and 407.1 for $([C_{13}H_7Cl_2IN_2O + 2H]^+$ (73.9 %). Combustion analysis for $C_{13}H_7Cl_2IN_2O$: Calculated. C 38.55, H 1.74, N 6.92; found: C 38.41, H 1.63, N 6.84. IR (cm^{-1}): 3351m ν(NH+OH), 3094m $\nu(CH)_{ar.}$, 2930m,br, 1656m ν(C=N), 1605m ν(C=C), 1565m, 1466s, 1366m, 1273m ν(C–O), 1181m, 1128m, 1095m, 961m, 865m, 814s $\delta(CH)_{ar.}$, 760m ν(C–Cl), 678m, 564m, 540m ν(C–I), 508m, 419m, cm^{-1}. ^{1}H-NMR (500 MHz, DMSO-d_6, δ): 13.22 (*s,* 1H, NH), 12.51 (*s,* 1H, OH), 8.38 (*d,* 1H, J = 2.0, H3'), 8.00 (*brs,* 1H, H4), 7.84 (*brs,* 1H, H7), 7.64 (dd, 1H, J_1 = 8.7, J_2 = 2.0, H5'), 6.87 (*d,* 1H, J = 8.7, H6'). Fluorescence spectroscopy (λ_{max}/nm): 393w, 476m.

*2-Chloro-6-(5,6-dichloro-1H-benzimidazol-2-yl)phenol (**HL$_6$**)*: Yield: 80 %. Matte yellow solid. Dec. p.: 373 °C. (+)ESI-MS (*m/z*): calculated for $[C_{13}H_7Cl_3N_2O]^+$ 313.5, observed 313.2 (100 %), 315.2 ($[C_{13}H_7Cl_3N_2O + 2H]^+$ (100 %) and 317.2 for ($[C_{13}H_7Cl_3N_2O + 4H]^+$ (47.6 %). Combustion analysis for $C_{13}H_7Cl_3N_2O$: Calculated. C 49.79, H 2.25, N 8.93; found: C 49.63, H 2.33, N 8.77. IR (cm^{-1}): 3336m,br ν(NH+OH), 3075w $\nu(CH)_{ar.}$, 1624m ν(C=N), 1601m

ν(C=C), 1464m, 1441m, 1373m, 1252m ν(C–O), 1094m, 968m, 860m δ(CH)$_{ar.}$, 785m, 747m ν(C–Cl), 736m ν(C–Cl), 665m, 611m, 571s, 427m, cm^{-1}. ^{1}H-NMR (500 MHz, DMSO-d$_6$, δ): 13.72 (*brs,* 1H, NH), 13.38 (*s,* 1H, OH1'), 8.08 (*brs,* 1H, H4), 8.02 (*dd,* 1H, J$_1$ = 7.9, J$_2$ = 1.5, H3'), 7.87 (*brs,* 1H, H7), 7.59 (*dd,* 1H, J$_1$ = 7.9, J$_2$ = 1.5, H5'), 7.06 (*t,* 1H, J$_1$ = J$_2$ = 7.9, H4'). Fluorescence spectroscopy (λ$_{max}$/nm): 394w,br, 463m,br.

2-(5,6-Dichloro-1H-benzimidazol-2-yl)-6-methoxyphenol (***HL$_7$***): Yield: 90 %. Creamy colored solid. Dec. p.: 343 °C. (+)ESI-MS (*m/z*): calculated for [C$_{14}$H$_{10}$Cl$_2$N$_2$O$_2$]$^+$ 309.0, observed 309.1 (100 %), 311.1 ([C$_{14}$H$_{10}$Cl$_2$N$_2$O$_2$ + 2H]$^+$ (69.7 %). Combustion analysis for C$_{14}$H$_{10}$Cl$_2$N$_2$O$_2$: Calculated. C 54.39, H 3.26, N 9.06; found: C 54.25, H 3.37, N 8.95. IR (cm^{-1}): 3294m,br ν(NH+OH), 3058w ν(CH)$_{ar.}$, 2943m ν(CH)$_{al.}$, 1623m ν(C=N), 1591m ν(C=C), 1476m, 1420m, 1372m, 1249s ν(C–O), 1182m ν(C–O), 1095m, 1056m, 967m, 857m δ(CH)$_{ar.}$, 776m ν(C–Cl), 731m, 603m, 545m, 425m, cm^{-1}. ^{1}H-NMR (500 MHz, DMSO-d$_6$, δ): 13.33 (*brs,* 1H, NH), 12.50 (*brs,* 1H, OH'), 7.92 (*brs,* 2H, H4+H3'), 7.63 (*d,* 1H, J = 2.9, H7), 7.12 (*dd,* 1H, J$_1$ = 8.0, J$_2$ = 1.1, H5'), 6.97 (*t,* 1H, J$_1$ = J$_2$ = 8.0, H4'), 3.84 (*s,* 3H, OCH$_3$). Fluorescence spectroscopy (λ$_{max}$/nm): 394w,br, 481s.

2-(5,6-Dichloro-1H-benzimidazol-2-yl)-5-methoxyphenol (***HL$_8$***): Yield: 80 %. Slightly yellow solid. Dec. p.: 292 °C. (+)ESI-MS (*m/z*): calculated for [C$_{14}$H$_{10}$Cl$_2$N$_2$O$_2$]$^+$ 309.0, observed 309.3 (100 %), 311.2 ([C$_{14}$H$_{10}$Cl$_2$N$_2$O$_2$ + 2H]$^+$ (64.7 %). Combustion analysis for C$_{14}$H$_{10}$Cl$_2$N$_2$O$_2$: Calculated. C 54.39, H 3.26, N 9.06; found: C 54.24, H 3.41, N 8.94. IR (cm^{-1}): 3344m,br ν(NH+OH), 3102m ν(CH)$_{ar.}$, 2971m ν(CH)$_{al.}$, 1640m ν(C=N), 1600m ν(C=C), 1453m, 1388s, 1267m ν(C–O), 1200m ν(C–O), 1134m, 1026m, 951m, 865m, 817m δ(CH)$_{ar.}$, 796m ν(C–Cl), 672m, 568m, 548m, 475m, 425m, cm^{-1}. ^{1}H-NMR (500 MHz, DMSO-d$_6$, δ): 13.17 (*s,* 1H, NH), 12.68 (*s,* 1H, OH), 7.96 (*d,* 1H, J = 8.8, H3'), 7.94 (*s,* 1H, H4), 7.77 (*s,* 1H, H7), 6.64 (*dd,* 1H, J$_1$ = 8.8, J$_2$ = 2.5, H4'), 6.59 (*d*, 1H, J = 2.4, H6'), 3.81 (*s,* 3H, OCH$_3$). Fluorescence spectroscopy (λ$_{max}$/nm): 394w,br, 452m.

2-(5,6-Dichloro-1H-benzimidazol-2-yl)-4-methoxyphenol (***HL$_9$***): Yield: 71 %. Slightly yellow solid. Dec. p.: 352 °C. (+)ESI-MS (*m/z*): calculated for [C$_{14}$H$_{10}$Cl$_2$N$_2$O$_2$]$^+$ 309.0, observed 309.2 (100 %), 311.2 ([C$_{14}$H$_{10}$Cl$_2$N$_2$O$_2$ + 2H]$^+$ (59.9 %). Combustion analysis for C$_{14}$H$_{10}$Cl$_2$N$_2$O$_2$: Calculated. C 54.39, H 3.26, N 9.06; found: C 54.25, H 3.43, N 8.95. IR (cm^{-1}): 3306m ν(NH+OH), 3076m ν(CH)$_{ar.}$, 2974m ν(CH)$_{al.}$, 1619m ν(C=N), 1598m ν(C=C), 1493m, 1450m, 1370m, 1273m ν(C–O), 1214m ν(C–O), 1171m, 1042m, 968m, 866m, 809m δ(CH)$_{ar.}$, 758m ν(C–Cl), 726m, 673m, 573m, 512m, 438m, cm^{-1}. ^{1}H-NMR (500 MHz, DMSO-d$_6$, δ): 13.24 (*s,* 1H, NH), 11.92 (*s,* 1H, OH), 8.01 (*brs,* 1H, H4), 7.85 (*brs,* 1H, H7), 7.66 (*d,* 1H, J = 2.4, H3'), 7.03 (*dd,* 1H, J$_1$ = 8.9, J$_2$ = 2.6, H5'), 6.99 (*d,* 1H, J$_1$ = 8.9, J$_2$ = 7.9, H6'), 3.80 (*s,* 3H, OCH$_3$). Fluorescence spectroscopy (λ$_{max}$/nm): 389s,br, 508m,br.

2-(5,6-dichloro-1H-benzimidazol-2-yl)-4-methylphenol (***HL$_{10}$***): Yield: 72 %. Slightly yellow solid. Dec. p.: 326 °C. (+)ESI-MS (*m/z*): calculated for [C$_{14}$H$_{10}$Cl$_2$N$_2$O]$^+$ 293.0, observed 293.2 (69.9 %), 295.2 ([C$_{14}$H$_{10}$Cl$_2$N$_2$O + 2H]$^+$ (100 %). Combustion analysis for C$_{14}$H$_{10}$Cl$_2$N$_2$O: Calculated. C 57.36, H 3.44, N 9.56; found: C 57.47, H 3.30, N 9.49. FT-IR (cm^{-1}): 3467m ν(OH), 3376m ν(NH), 3062m ν(CH)$_{ar.}$, 2925m ν(CH)$_{al.}$, 1614m ν(C=N), 1584m ν(C=C), 1485s, 1354m, 1284m ν(C–O), 1257m, 1134m, 962m, 855m, 812s δ(CH)$_{ar.}$, 780m ν(C–Cl), 685m, 554m, 476m, 442m, 421m, cm^{-1}. ^{1}H-NMR (500 MHz, DMSO-d$_6$, δ): 13.20 (*brs,* 1H, NH), 12.16 (*brs,* 1H, OH), 7.95 (*brs,* 1H, H4), 7.89 (*d,* 1H, J = 1.7, H3'), 7.84 (*brs,* 1H, H7), 7.21 (*dd,* 1H, J$_1$ = 8.3, J$_2$ = 1.8, H5'), 6.95 (*d*, 1H, J = 8.3, H6'), 2.32 (*s,* 3H, CH$_3$). Fluorescence spectroscopy (λ$_{max}$/nm): 375w,br, 394w,br, 482m.

2-(5,6-dichloro-1H-benzimidazol-2-yl)-6-methylphenol (***HL$_{11}$***): Yield: 94 %. Slightly bright yellow solid. Dec. p.: 357 °C. (+)ESI-MS (*m/z*): calculated for [C$_{14}$H$_{10}$Cl$_2$N$_2$O]$^+$ 293.0,

observed 293.3 (100 %), 295.2 ($[C_{14}H_{10}Cl_2N_2O + 2H]^+$ (92.7 %). Combustion analysis for $C_{14}H_{10}Cl_2N_2O$: Calculated. C 57.36, H 3.44, N 9.56; found: C 57.50, H 3.55, N 9.42. IR (cm^{-1}): 3323m,br ν(NH+OH), 3054m ν$(CH)_{ar.}$, 2951m ν$(CH)_{al.}$, 1628m ν(C=N), 1601m ν(C=C), 1475m, 1445m, 1415m, 1370m, 1300m, 1252m ν(C–O), 1094m, 1013m, 966m, 886m, 863m δ$(CH)_{ar.}$, 786s ν(C–Cl), 665m, 573s, 518m, 428m, cm^{-1}. ^{1}H-NMR (500 MHz, DMSO-d_6, δ): 13.52 (*s,* 1H, NH), 13.01 (*s,* 1H, OH), 8.03 (*s,* 1H, H4), 7.87 d (1H, J = 7.6, H3'), 7.81 s (1H, H7), 7.31 d (1H, J = 7.3, H5'), 6.95 dd (1H, J_1 = 7.5, J_2 = 7.6, H4'), 2.26 (*s,* 3H, CH_3). Fluorescence spectroscopy (λ_{max}/nm): 379w,br, 473s.

*2-Bromo-4-chloro-6-(5,6-dichloro-1H-benzimidazol-2-yl)phenol (**HL$_{12}$**)*: Yield: 82 %. Mate light yellow solid. Dec. p.: 228 °C. (+)ESI-MS (*m/z*): calculated for $[C_{13}H_6BrCl_3N_2O + H]^+$ 393.5, observed 393.1 (100 %), 395.1 ($[C_{13}H_6BrCl_3N_2O + 3H]^+$ (64.5 %), 391.1 $[C_{13}H_6BrCl_3N_2O – H]^+$ (55.7 %). Combustion analysis for $C_{13}H_6BrCl_3N_2O$: Calculated. C 39.78, H 1.54, N 7.14; found: C 39.75, H 1.66, N 7.01. IR (cm^{-1}): 3403m ν(NH+OH), 3085m ν$(CH)_{ar.}$, 1669s ν(C=O), 1624m ν(C=N), 1601m ν(C=C), 1448m, 1373m, 1256m ν(C–O), 1096m, 970m, 853m δ$(CH)_{ar.}$, 754m ν(C–Cl), 722m ν(C–Cl), 669m, 610m, 554m ν(C–Br), 498m, 423m, cm^{-1}. ^{1}H-NMR (500 MHz, DMSO-d_6, δ): 13.80 (*brs,* 1H, NH), 13.44 (*s,* 1H, OH), 8.18 (*brs,* 1H, H4), 8.05 (*brs,* 1H, H7), 7.95 (*s,* 1H, H3'), 7.84 (*brs,* 1H, H5'). Fluorescence spectroscopy (λ_{max}/nm): 393w,br, 479s,br.

*4-Bromo-2-(5,6-dichloro-1H-benzimidazol-2-yl)-6-fluorophenol (**HL$_{13}$**)*: Yield: 74 %. Dirty yellow solid. Dec. p.: 284 °C. (+)ESI-MS (*m/z*): calculated for $[C_{13}H_6BrCl_2FN_2O + H]^+$ 376.0, observed 377.2 (100 %), 375.1 ($[C_{13}H_6BrCl_2FN_2O – H]^+$ (65.6 %). Combustion analysis for $C_{13}H_6BrCl_2FN_2O$: Calculated. C 41.53, H 1.61, N 7.45; found: C 41.43, H 1.73, N 7.27. IR (cm^{-1}): 3398m ν(NH+OH), 3084m ν$(CH)_{ar.}$, 2872m,br, 1662s ν(C=O), 1614m ν(C=N), 1577m ν(C=C), 1489s, 1374m, 1265s ν(C–O), 1233m, 1095m, 972m, 916m, 855s δ$(CH)_{ar.}$, 807m, 754m ν(C–Cl), 666m, 553m ν(C–Br), 427m, cm^{-1}. ^{1}H-NMR (500 MHz, DMSO-d_6, δ): 13.58 (*brs,* 1H, NH), 13.15 (*brs,* 1H, OH), 8.10 (*d,* 1H, J = 2.3, H5'), 7.96 (*brs,* 1H, H4), 7.94 (*brs,* 1H H7), 7.66 (*d,* 1H, J = 2.4, H3'). Fluorescence spectroscopy (λ_{max}/nm): 393w, 418sh, 469s.

*2-Chloro-6-(5,6-dichloro-1H-benzimidazol-2-yl)-4-fluorophenol (**HL$_{14}$**)*: Yield: 89 %. Slightly yellow solid. Dec. p.: 341 °C. (+)ESI-MS (*m/z*): calculated for $[C_{13}H_6Cl_3FN_2O]^+$ 331.5, observed 331.3 (100 %), 333.3 ($[C_{13}H_6Cl_3FN_2O + 2H]^+$ (73.9 %). Combustion analysis for $C_{13}H_6Cl_3FN_2O$: Calculated. C 47.09, H 1.82, N 8.45; found: C 47.21, H 1.96, N 8.27. IR (cm^{-1}): 3420m ν(NH+OH), 3089m ν$(CH)_{ar.}$, 1662m ν(C=O), 1622m ν(C=N), 1577m ν(C=C), 1466m, 1444s, 1370m, 1264m ν(C–O), 1209m, 1100m, 999m, 867s δ$(CH)_{ar.}$, 793m ν(C–Cl), 741m ν(C–Cl), 666m, 573m, 507m, 425m, cm^{-1}. ^{1}H-NMR (500 MHz, DMSO-d_6, δ): 13.69 (*brs,* 1H, NH), 13.48 (*brs,* 1H, OH), 8.06 (*brs,* 1H, H5'), 7.92 (*d,* 1H, J = 3.0, H4), 7.90 (*d,* 1H, J = 3.0, H7), 7.61 (*d,* 1H, J = 3.0, H3'). Fluorescence spectroscopy (λ_{max}/nm): 394w,br, 482m,br.

*2,4-Dichloro-6-(5,6-dichloro-1H-benzimidazol-2-yl)phenol (**HL$_{15}$**)*: Yield: 86 %. Mate yellow solid. Dec. p.: 344 °C. (+)ESI-MS (*m/z*): calculated for $[C_{13}H_6Cl_4N_2O + H]^+$ 349.0, observed 349.3 (100 %), 347.3 ($[C_{13}H_6Cl_4N_2O – H]^+$ (64.2 %), 351.3 ($[C_{13}H_6Cl_4N_2O + 3H]^+$ (54.8 %). Combustion analysis for $C_{13}H_6Cl_4N_2O$: Calculated C 44.87, H 1.74, N 8.05; found: C 44.71, H 1.87, N 8.16. IR (cm^{-1}): 3408m ν(NH+OH), 3078m ν$(CH)_{ar.}$, 1722m ν(C=O), 1657m ν(C=N), 1623m ν(C=C), 1576m, 1477m, 1442s, 1365m, 1259m ν(C–O), 1187m, 1099m, 974m, 869m, 817m δ$(CH)_{ar.}$, 766m ν(C–Cl), 728m ν(C–Cl), 667m, 614m, 558m, 501m, 427m, cm^{-1}. ^{1}H-NMR (500 MHz, DMSO-d_6, δ): 13.78 (*brs,* 2H, NH+OH), 8.15 (*d,* 1H, J = 2.5, H3'), 8.07 (*brs,* 1H, H4), 8.03 (*brs,* 1H, H7), 7.73 (*d,* 1H, J = 2.5, H5'). Fluorescence spectroscopy (λ_{max}/nm): 393w,br, 478m,br.

*2,4-Dibromo-6-(5,6-dichloro-1H-benzimidazol-2-yl)phenol (**HL$_{16}$**)*: Yield: 75 %. Orangey yellow solid. Dec. p.: 275 °C. (+)ESI-MS (*m/z*): calculated for $[C_{13}H_6Br_2Cl_2N_2O]^+$ 437.0, observed 437.3 (100 %), 439.3 ($[C_{13}H_6Br_2Cl_2N_2O + 2H]^+$ (98.9 %), 435.3 ($[C_{13}H_6Br_2Cl_2N_2O – H]^+$ (41.6 %). Combustion analysis for $C_{13}H_6Br_2Cl_2N_2O$: Calculated. C 35.74, H 1.38, N 6.41; found: C 35.65, H 1.47, N 6.55. IR (cm^{-1}): 3354w ν(NH), 3313w ν(OH), 3069m $\nu(CH)_{ar.}$, 1637m ν(C=N), 1604m ν(C=C), 1558m, 1458s, 1445s, 1364m, 1259m ν(C–O), 1097m, 973m, 855s, 836m $\delta(CH)_{ar.}$, 733m ν(C–Cl), 684m, 599m, 550m ν(C–Br), 447m, 420m, cm^{-1}. ^{1}H-NMR (500 MHz, DMSO-d_6, δ): 13.88 (*brs,* 1H, NH), 13.82 (*brs,* 1H, OH), 8.32 (*s,* 1H, J = 2.2, H3'), 8.08 (*brs,* 1H, H4), 8.03 (*brs,* 1H, H7), 7.94 (*d,* 1H, J = 2.1, H5'). Fluorescence spectroscopy (λ_{max}/nm): 479s.

*2-(5,6-Dichloro-1H-benzimidazol-2-yl)-4,6-diiodophenol (**HL$_{17}$**)*: Yield: 76 %. Yellowish orange solid. Dec. p.: 203 °C. (+)ESI-MS (*m/z*): calculated for $[C_{13}H_6Cl_2I_2N_2O]^+$ 531.0, observed 531.3 (100 %), 533.2 ($[C_{13}H_6Cl_2I_2N_2O + 2H]^+$ (64.1 %). Combustion analysis for $C_{13}H_6Cl_2I_2N_2O$: Calculated. C 29.41, H 1.14, N 5.28; found: C 29.57, H 1.07, N 5.37. IR (cm^{-1}): 3472m ν(NH), 3375m ν(OH), 3059m $\nu(CH)_{ar.}$, 1665m ν(C=O), 1622m ν(C=N), 1594m ν(C=C), 1440s, 1356m, 1257m ν(C–O), 1136m, 1093m, 965m, 860s, 825m $\delta(CH)_{ar.}$, 736m ν(C–Cl), 662m, 595m, 541m ν(C–I), 426m, cm^{-1}. ^{1}H-NMR (500 MHz, DMSO-d_6, δ): 13.73 (*brs,* 1H, NH), 12.64 (*s,* 1H, OH), 8.39 (*d,* 1H, J = 2.0, H5'), 8.13 (*s,* 1H, H4), 7.99 (*d,* 1H, J = 2.0, H3'), 7.95 (*s,* 1H, H7). Fluorescence spectroscopy (λ_{max}/nm): 393w,br 486s.

*4-Chloro-2-(5,6-dichloro-1H-benzimidazol-2-yl)-6-methoxyphenol (**HL$_{18}$**)*: Yield: 85 %. Matte yellow solid. Dec. p.: 274 °C. (+)ESI-MS (*m/z*): calculated for $[C_{14}H_9Cl_3N_2O_2]^+$ 343.5, observed 343.2 (100 %), 345.2 ($[C_{14}H_9Cl_3N_2O_2 + 2H]^+$ (92.9 %). Combustion analysis for $C_{14}H_9Cl_3N_2O_2$: Calculated. C 48.94, H 2.64, N 8.15; found: C 48.79, H 2.80, N 8.00. IR (cm^{-1}): 3359m ν(NH+OH), 3102m $\nu(CH)_{ar.}$, 2951m $\nu(CH)_{al.}$, 2858m,br, 1665m ν(C=N), 1614m ν(C=C), 1579m, 1488m, 1442s, 1405m, 1315m, 1249s ν(C–O), 1095m, 1051m, 974m, 836m, 807m $\delta(CH)_{ar.}$, 730m ν(C–Cl), 725m ν(C–Cl), 621m, 552m, 433m, cm^{-1}. ^{1}H-NMR (500 MHz, DMSO-d_6, δ): 13.40 (*s,* 1H, NH), 12.62 (*s,* 1H, OH), 7.98 (*brs,* 1H, H4), 7.89 (*brs,* 1H, H7), 7.73 (*d,* 1H, J = 2.4, H3'), 7.18 (*d,* 1H, J = 2.0, H5'), 3.87 (*s,* 3H, OCH_3). Fluorescence spectroscopy (λ_{max}/nm): 393w, 482s.

*4-Bromo-2-(5,6-dichloro-1H-benzimidazol-2-yl)-6-methoxyphenol (**HL$_{19}$**)*: Yield: 75 %. Skin color solid. Dec. p.: 229 °C. (+)ESI-MS (*m/z*): calculated for $[C_{14}H_9BrCl_2N_2O_2 + H]^+$ 389.0, observed 389.1 (100 %), 387.1 ($[C_{14}H_9BrCl_2N_2O_2 – H]^+$ (61.2 %). Combustion analysis for $C_{14}H_9BrCl_2N_2O_2$: Calculated. C 43.33, H 2.34, N 7.22; found: C 43.51, H 2.23, N 7.03. IR (cm^{-1}): 3356m ν(NH), 3279m ν(OH), 3083m $\nu(CH)_{ar.}$, 2852w,br, 1675m ν(C=O), 1621m ν(C=N), 1602m ν(C=C), 1440m, 1372m, 1254s ν(C–O), 1238m ν(C–O), 1093m, 1058m, 972m, 838m, 806m $\delta(CH)_{ar.}$, 710m ν(C–Cl), 640m, 551m ν(C–Br), 487m, 428m, cm^{-1}. ^{1}H-NMR (500 MHz, DMSO-d_6, δ): 13.42 (*s,* 1H, NH), 12.66 (*s,* 1H, OH), 8.04 (*s,* 1H, H4), 7.87 (*s,* 1H, H7), 7.86 (*d,* 1H, J = 2.2, H5'), 7.25 (*d,* 1H, J=2.2, H3'), 3.87 (*s,* 3H, OCH_3). Fluorescence spectra (λ_{max} / nm): 393w, 486s.

*2,4-Dibromo-6-(5,6-dichloro-1H-benzimidazol-2-yl)-3-methoxyphenol (**HL$_{20}$**)*: Yield: 88 %. Yellowish orange solid. Dec. p.: 234 °C. (+)ESI-MS (*m/z*): calculated for $[C_{14}H_8Br_2Cl_2N_2O_2]^+$ 467.0, observed 467.1 (100 %), 469.1 ($[C_{14}H_8Br_2Cl_2N_2O_2 + 2H]^+$ (83.2 %). Combustion analysis for $C_{14}H_8Br_2Cl_2N_2O_2$: Calculated. C 36.01, H 1.73, N 6.00; found: C 36.35, H 1.93, N 5.87. IR (ATR, cm^{-1}): 3367w ν(OH), 3126m ν(NH), 3088m $\nu(CH)_{ar.}$, 2938m $\nu(CH)_{al.}$, 1665m ν(C=O), 1632m ν(C=N), 1600m, ν(C=C), 1564m, 1429m, 1372s, 1260m ν(C–O), 1230m ν(C–O), 1096m, 1061m, 970m, 863m $\delta(CH)_{ar.}$, 774m, 753m ν(C–Cl), 664m, 627m, 551m ν(C–Br), 460m, 412m, cm^{-1}. ^{1}H-NMR (500 MHz, DMSO-d_6, δ): 13.76 (*brs*, 2H,

NH+OH), 8.38 (*s*, 1H, H3'), 7.97 (*s*, 1H, H4), 7.95 (*s*, 1H, H7), 3.86 (*s*, 3H, OCH_3). Fluorescence spectra (λ_{max} / nm): 393w,br, 467m,br.

TABLE SI. Selected bond distances and angles for **HL_{18}** (Å, º)

C7—N1	1.367(3)	C7—N2	1.323(3)
C2—Cl1	1.739(3)	C3—Cl2	1.740(3)
C1—C2	1.377(4)	C2—C3	1.401(4)
C7—C8	1.461(3)	C9—O1	1.353(3)
C10—O2	1.368(3)	C14—O2	1.428(3)
C12—Cl3	1.740(3)	C9—C10	1.402(4)
C10—C11	1.376(4)	C11—C12	1.391(4)
C9-O1-H1A	109.5	N2-C7-N1	111.8(2)
N1-C5-C6	105.4(2)	C1-C2-Cl1	119.3(2)
C3-C2-Cl1	119.6(2)	C2-C3-Cl2	119.9(2)
C4-C3-Cl2	118.2(2)	N1-C5-C6	105.4(2)
N2-C7-N1	111.8(2)	C10-O2-C14	116.1(2)
C11-C12-Cl3	117.8(2)	C13-C12-Cl3	120.6(2)

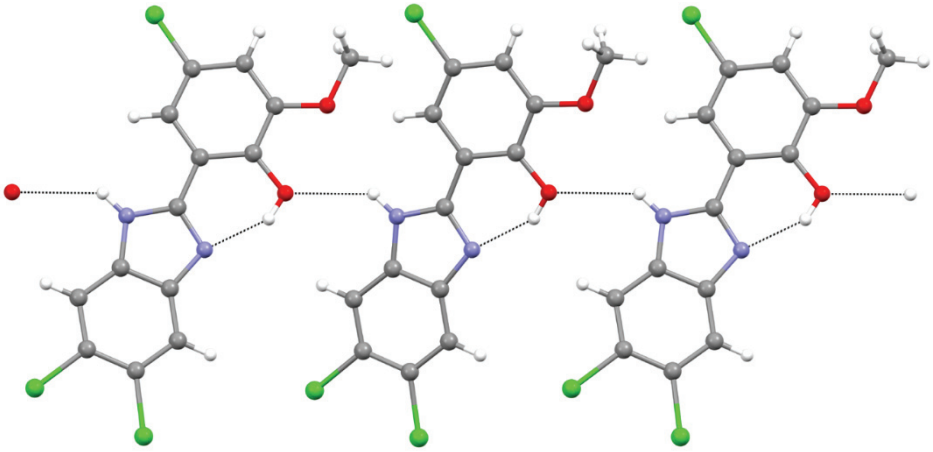

Fig. S1. Part of the crystal structure of **HL_{18}**, showing the formation of C(6) chain.

Journal of the Serbian Chemical Society
JSCS@tmf.bg.ac.rs • www.shd.org.rs/JSCS
J. Serb. Chem. Soc. *91* (2) 129–144 (2026)
JSCS–5482
Original scientific paper
Published 8 February, 2026

Molecular dynamics-based methodological approach to clarify perfluorooctanoic acid binding on human serum albumin

ALEKSANDRA M. ĐURĐEVIĆ ĐELMAŠ[1], DANILO P. TRAJKOVIĆ[1], KARLA MILČIĆ[2] and MILOŠ K. MILČIĆ[1]*

[1]*University of Belgrade – Faculty of Chemistry, Studentski trg 12–16, 11158 Belgrade, Serbia and* [2]*Institute of Chemistry, Technology and Metallurgy, Department of Chemistry, University of Belgrade, National Institute of the Republic of Serbia, Njegoševa 12, 11000 Belgrade, Serbia*

(Received 20 August, revised 27 August, accepted 5 September 2025)

Abstract: Perfluorooctanoic acid (PFOA) is a persistent environmental contaminant that binds strongly to human serum albumin (HSA), influencing its distribution and toxicokinetics. While crystallographic studies in the presence of myristic acid have identified a limited number of high-affinity binding sites, additional sites may remain undetected due to competitive binding. Here, we combined molecular docking with extensive molecular dynamics (MD) simulations to comprehensively characterize PFOA–HSA interactions. A tiled docking approach revealed twelve non-overlapping binding poses, including six not previously reported. Ligand–residue interaction mapping, *RMSD* analysis and MM/PBSA free energy calculations identified four sites, FA3, FA1, FA4 and FA6, as the most stable PFOA binding positions in the absence of competing ligands. Among all examined sites, FA3 displayed the most favorable calculated binding energy. Furthermore, ligands at both FA1 and FA3 sites exhibited over 23 and 85 kJ/mol more favorable binding energy, respectively as calculated by MM/PBSA, than the ligand at well-characterized FA4 site under other ligand-free conditions. Persistent salt bridges, hydrogen bonds, and halogen contacts were identified as key stabilizing interactions. Free-energy landscapes further confirmed the stability of PFOA binding at these sites. These findings provide a more complete understanding of the PFOA binding landscape on HSA, offering insights that may inform the design of biomimetic capture agents and strategies for environmental remediation.

Keywords: protein–ligand interactions; PFAS; binding free energy calculations.

* Correspondence E-mail: mmilcic@chem.bg.ac.rs
https://doi.org/10.2298/JSC250820067D

INTRODUCTION

Proteins are highly dynamic macromolecules involved in a wide range of vital biological processes both within and between cells. One of their essential functions is transporting various molecules, ranging from simple ions and small gases to more complex compounds such as hormones, fatty acids, neurotransmitters, amino acids, nucleic acids and drugs, collectively referred to as ligands.[1] The interactions between proteins and ligands have been extensively investigated, as proteins are not only capable of reversible ligand binding but often exhibit enzymatic activity that enables ligand transformation.[2] To understand a protein's role at the molecular level, it is crucial to identify its ligand binding site and the specific amino acid residues involved in the interaction. These residues are central to determining binding specificity and are particularly important in enzymatic recognition, where factors like side chain orientation and physicochemical properties critically affect affinity and selectivity.[3] Interestingly, Kuntz *et al.* observed that binding affinity generally increases with ligand size, but this trend plateaus when ligands exceed approximately 15 non-hydrogen atoms. Beyond this threshold, additional atoms contribute minimally to binding energy, revealing a nonlinear relationship between ligand size and binding strength.[4] Consequently, understanding ligand binding involves more than locating the binding site, it requires evaluating the broader molecular and energetic environment that governs the interaction.[5,6] Such insights are indispensable not only for fundamental biological research but also for practical applications such as rational drug design, enzyme optimization, and targeted mutagenesis.[7]

Human serum albumin (HSA) is the most abundant carrier protein in the human body, playing a vital role in maintaining osmotic pressure and transporting a wide variety of endogenous and exogenous ligands (fatty acids, amino acids, hormones, ions such as Ca^{2+}, Na^{+} and K^{+}, water, drugs,…).[8,9] It has been demonstrated that HSA is the principal transporter of perfluorooctanoic acid (PFOA) in the bloodstream.[10] PFOA (C8) is a widely prevalent perfluorinated compound structurally similar to fatty acids, whose exceptional chemical stability and resistance to degradation cause it to persist in the environment and accumulate in living organisms, resulting in significant human exposure through contaminated food and water and raising serious health concerns due to its biological half-life of approximately three years.[11,12]

Experimental and theoretical studies have identified multiple potential PFOA binding sites on HSA.[13–16] Docking simulations have revealed several putative binding locations, suggesting that while docking is a useful tool for predicting interaction sites, it may not fully capture the complexity of ligand binding due to inherent biases and its static nature. Moreover, docking often relies on X-ray crystallographic structures of proteins, which may be incomplete or lack sufficient resolution, further limiting the reliability of this method in accurately identifying true

binding sites. Limited by incomplete molecular models and scoring function shortcomings, docking alone cannot reliably predict binding affinity or the precise binding locations.[17] Protein–ligand association can be described as diffusion across a multidimensional energy landscape, which typically contains an energy minimum corresponding to the bound complex. As the ligand approaches the protein, long-range electrostatic interactions guide the process along a binding funnel that may contain local minima and multiple competing pathways.[18] In the case of PFOA binding to HSA, such complexity is particularly relevant, as this ligand is highly flexible and amphiphilic, capable of transiently interacting with several regions on the protein surface. These dynamic features often elude static docking approaches, which oversimplify the energy landscape and may miss alternative or transient binding modes.

A recent study by Maso *et al.*[13] identified a single high-affinity binding site for PFOA on HSA, along with three lower-affinity sites. These four sites were confirmed through crystallization of HSA with PFOA; however, the experiments were performed in the presence of myristic acid. Consequently, only binding positions where PFOA outcompeted myristic acid were detected, potentially leaving additional PFOA binding sites unidentified. Comprehensive mapping of all binding sites is important for fully understanding PFOA–HSA interactions, as this knowledge would enable the rational design of biomimetics capable of targeting and binding multiple PFOA molecules under diverse environmental conditions. Moreover, identifying all sites could support the development of more robust environmental remediation strategies, producing biomimetics with greater versatility in recognizing and sequestering PFOA across a range of concentrations.

Despite increasing evidence that PFOA can interact with multiple regions of HSA, the complete landscape of binding sites, their relative affinities, and the molecular determinants of binding remain insufficiently characterized. Existing structural studies have been limited by the presence of competing ligands, while computational docking alone cannot capture the conformational flexibility and dynamic nature of ligand–protein interactions. To overcome these limitations, we combined exhaustive molecular docking with molecular dynamics (MD) simulations to evaluate the stability, energetics and residue-level interactions of PFOA at all predicted binding positions. This integrated approach enabled the identification of energetically and kinetically favorable sites under other ligand-free conditions, providing a more comprehensive understanding of the PFOA–HSA interaction network. By mapping these sites and characterizing their key stabilizing interactions, our study offers new insights into the molecular basis of PFOA binding that can inform the design of selective biomimetic capture agents and guide the development of effective environmental remediation strategies.

EXPERIMENTAL

Molecular docking

Although numerous crystal structures of human serum albumin (HSA) are available in the Protein Data Bank, the structure with PDB ID: 1N5U[25] (1.90 Å) was selected for this study due to its high resolution, complete domain coverage, and absence of large conformational distortions, making it a reliable and structurally representative model. Prior to docking, all co-crystallized ligands (*e.g.*, myristic acid) were removed. Protonation states of titratable residues were assigned using H++ 3.0.[19] AutoDockTools[20] (v1.5.7) was used for assigning partial charges to protein atoms. The geometry of anion of perfluorooctanoic acid (PFOA) was optimized at the DFT/B3LYP/6-311G(d,p) level using Gaussian 09.[21] A systematic grid-based search strategy was employed, generating 1,248 partially overlapping boxes (24×24×24 $Å^3$) shifted by 8 Å to ensure complete screening of protein surface and volume. All atoms in the protein molecule were kept rigid, while free rotation around single bonds in ligand were allowed. Docking simulations were performed with AutoDock Vina.[22] Final binding poses and interaction sites were visualized using PyMOL2 and Discovery Studio 2024.

Molecular dynamics simulations

Molecular dynamics (MD) simulations were performed using the AMBER software. The protein structure was prepared by assigning appropriate protonation states and parameterizing it using the ff19SB force field.[23] The DFT-optimized structure of PFOA was used as input, while ligand topologies were generated following the standard procedure recommended by the AMBER developers. For bonds, valence angles, torsion and improper torsion angles and Lennard-Jones parameters standard generalized AMBER force-field version 2 (gaff2) parameters were used.[24] Partial atomic charges were determined by first calculating Mertz–Kollman electrostatic potential at MP2/def2-TZVP level of theory and then deriving partial charges with RESP procedure.[25] Molecular dynamic simulations were performed with 12 ligands simultaneously. Initial ligand positions were determined by docking: 12 poses with the highest docking score were used.

The optimal point charge (OPC) model was used for water and counterions added to neutralize the system. The OPC model was chosen because it provides improved accuracy in reproducing key thermodynamic and dynamic properties of liquid water compared to commonly used three-point and four-point models, while remaining computationally efficient for large-scale MD simulations. The system was neutralized with Na^+ and solvated in a truncated octahedron box of water with at least 10 Å between box edges and protein residues. Additional Na^+ and Cl^- were added to simulate the 0.15 M salt concentration. Simulations were done under periodic boundary conditions and particle mesh evald summation method was used for calculating long range electrostatics. The system was initially minimized for 2,000 steps using Newton–Raphson algorithm, and then slowly heated from 100 to 298 K for 1 ns with time-step of 1 fs, while keeping the volume constant. The initial restraint on protein and ligand atoms was 418.40 kJ/(mol $Å^2$). Next, the system was relaxed for a total of 6 ns with 1 fs time step, in NPT ensemble, by slowly lifting restraints (to 41.64, 4.18 and 0.42 kJ/(mol $Å^2$)). Finally, 5 ns of equilibration in the NPT ensemble with 1 fs time step and no restraints was conducted. For a 1000-ns production run, NPT ensemble was chosen with Langevin thermostat and Berendsen barostat and 2 fs time step. The SHAKE algorithm was employed to impose constraints on hydrogen atoms. Simulations were performed in triplicate starting from the same docking poses but with different randomly assigned initial velocities.

Molecular dynamics trajectory analysis and collective variable calculations were done with the cpptraj program.[26] Gromacs sham utility[27] was used for free energy landscape calculations. PLIP (protein ligand interaction profiler) program was used for calculating protein ligand interactions from MD trajectory. Images are created in Pymol, VMD and Discovery studio visualizer programs.

RESULTS AND DISCUSSION

To identify all potential PFOA binding sites on HSA, we performed molecular docking simulations using the DFT-optimized structure of PFOA and the crystal structure of HSA (PDB ID: 1N5U). To provide structural context, Fig. S-1 of the Supplementary material to this paper illustrates the domain organization of HSA together with its fatty acid binding sites. To achieve exhaustive spatial coverage of the protein surface and internal cavities, the HSA structure was divided into over 1,200 partially overlapping grid boxes. Separate docking calculations were performed for each box using AutoDock Vina, an approach that enables high-resolution, tiled screening and has proven effective for mapping ligand binding to large proteins.[28] This systematic search identified 12 non-overlapping binding poses, with predicted binding scores ranging from –41.00 to –25.94 kJ/mol (Table I, Fig. 1). The top 12 docking poses were selected based on an energy cut-off of 15 kJ/mol relative to the best-scoring pose.

TABLE I. Twelve best-docked PFOA ligands to HSA, labeled as L1-L12, along with their predicted binding energies obtained from molecular docking and calculated binding energies using the MM-PBSA method (kJ/mol). Bolded values indicate 4 ligand binding sites selected after MD simulations

Ligand position	Binding energies estimated by molecular docking	Binding energies calculated by MM-PBSA
L1 (FA5)	–41.00	–34.81±2.09
L2	–37.66	–33.58±4.31
L3	–36.82	–63.89±4.56
L4	–35.98	–87.11±5.82
L5	–35.15	–42.38±5.77
L6	–33.47	–9.16±3.64
L7	–32.22	–6.32±2.38
L8	–30.54	–149.08±3.22
L9	–28.45	–24.31±2.26
L10	–27.20	4.35±1.76
L11	–26.78	–1.26±6.86
L12	–25.94	–14.31±1.92

The docking simulations identified the highest-affinity PFOA binding pose (–41.00 kJ/mol) in fatty acid site 5 (FA5, Fig. S-1), stabilized by multiple non-covalent interactions. Halogen interactions occur between fluorine atoms on the PFOA tail and the side chains of Lys525 and Ala528. The carboxylate head group of PFOA forms a hydrogen bond with Ser579, while carbon–hydrogen bonds are

established with the side chains of Met548 and Leu529. Additional stabilization is provided by a π-lone pair interaction between Phe551 and a fluorine atom, as well as a π-alkyl interaction between Phe551 and the terminal carbon of PFOA. An alkyl interaction is also observed between Lys525 and the terminal carbon of PFOA (Fig. 1, L1). Notably, Met548 has previously been implicated in PFOA binding by Wu *et al.*,[29] although no other interacting residues were reported. Consequently, it remains unclear whether the site described by Wu *et al.* overlaps with the FA5 site identified in this study. Furthermore, crystallographic analysis of HSA in the presence of both myristic acid and PFOA showed myristic acid[13] occupying FA5, suggesting that competitive binding could influence the detection and characterization of this site.

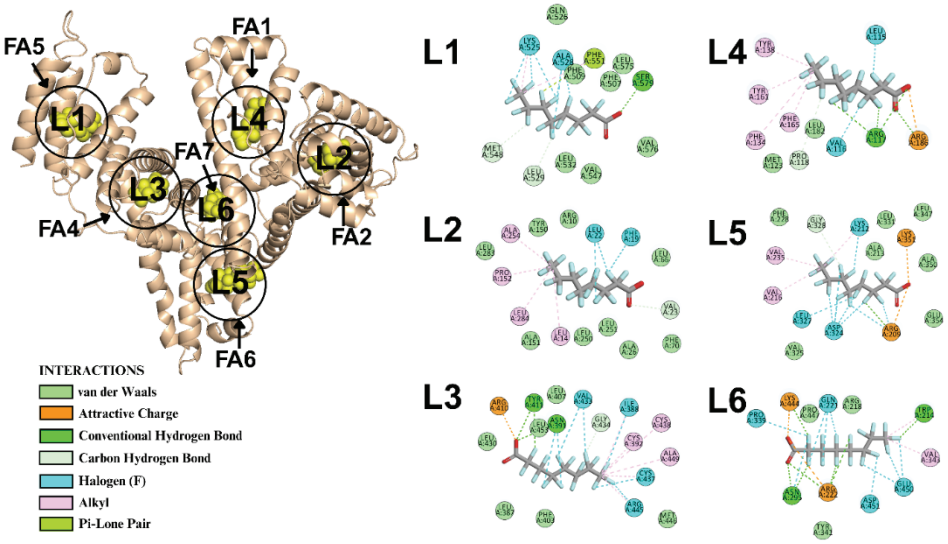

Fig. 1. Left: 3D structure of HSA with PFOA bound at the six top-scoring docking positions. Right: 2D interaction diagrams between HSA residues and PFOA for these positions.

A binding site with a calculated binding score of –37.66 kJ/mol was identified in domain Ia, near the N-terminus and adjacent to fatty acid binding site 2 (FA2) (Fig. S-1). This site is characterized by a hydrogen bond between Val23 and the carboxylic group of PFOA, supported by additional stabilizing contacts: alkyl interactions with Leu14, Pro152, Ala254 and Leu284; halogen interactions with Leu22 and Phe19; and van der Waals contacts with Arg10, Leu66, Tyr150, Ala151, Leu251 and Leu283 (Fig. 1, L2). Although this binding site has not been previously described, it is occupied by myristic acid in the crystal structure reported by Maso *et al.*[13]

The best-characterized PFOA binding site reported in multiple studies[13,30,31] and identified as a high-affinity site by Maso *et al.*[13] corresponds to the third-

highest affinity pose in our docking simulations (–36.82 kJ/mol). This site is located at Sudlow's site II, overlapping with fatty acid site 4 (FA4, Fig. S-1). At this position, the carboxylic group of PFOA forms a salt bridge with Arg410 and hydrogen bonds with Tyr411 and Asn391, all of which have been consistently identified as key interacting residues in previous reports. Additional stabilization is provided by halogen interactions with Val433, Ile388, Cys437 and Arg445, as well as alkyl interactions with Cys392, Cys438 and Ala449 (Fig. 1, L3).

The fourth-highest affinity PFOA binding site identified in our docking simulations –35.98 kJ/mol) is located at fatty acid site 1 (FA1), a site previously described by Salvalaglio *et al.*[32] and found to be occupied by myristic acid in the crystal structure reported by Maso *et al.*[13] At this location, PFOA binding is primarily mediated through interactions of its carboxylic head group with Arg186 and Arg117. Additional stabilization arises from halogen contacts with Leu115 and Val116, π-alkyl interactions with Phe134, Tyr138, Tyr161 and Phe165, and a carbon–hydrogen bond with Pro118 (Fig. 1, L4).

The next binding site (L5), with a predicted binding energy of –35.15 kJ/mol, aligns with fatty acid site 6 (FA6) and has been previously reported as a lower-affinity site for PFOA[13,33] (Fig. 1, L5). Key stabilizing interactions include salt bridges with Lys351 and Arg209, along with halogen interactions involving Lys212, Asp324 and Leu327. Additional stabilization is provided by alkyl interactions with Val216 and Val235.

The final PFOA binding site previously described in the literature by Maso *et al.*[13] and Crisali *et al.*[30] corresponds to the next-highest affinity pose identified in our docking simulations, with a predicted binding energy of –33.47 kJ/mol. This site is located near fatty acid site 7 (FA7), where the carboxylic head group of PFOA forms salt bridges with Arg222 and Lys444. Binding is further stabilized by halogen interactions with Gln221, Pro339, Glu450 and Asp451; hydrogen bonds with Trp214 and Asn295; and an alkyl interaction with Val343 (Fig. 1, L6). This site has also been observed in crystal structures and characterized as a low-affinity PFOA binding site.[13]

In addition to the previously reported binding sites, our analysis identified six lower-affinity PFOA binding sites, each with predicted binding energies below –33.47 kJ/mol. These sites have not been described in earlier studies. As with the higher-affinity sites, PFOA binding at these locations is stabilized through a combination of salt bridges involving Arg and Lys residues, hydrogen bonds, alkyl interactions, and halogen contacts (Fig. S-2 of the Supplementary material). Among the twelve highest-affinity sites identified in our docking study, only one previously reported lower-affinity site, located at a cleft in the crystal structure, was not observed. This absence is likely attributable to the high conformational mobility at the interface between domains, which may preclude stable ligand binding at this position.

To further explore the stability and temporal behavior of these interactions under dynamic conditions, we monitored PFOA–HSA contacts throughout the MD simulations. During the simulation, no significant conformational changes in the protein structure were observed, with the *RMSD* remaining within 3 Å throughout the entire trajectory (Figs. S-3 and S-4 of the Supplementary material). For this purpose, PLIP (protein ligand interaction profiler)[34] program was used for identification of ligand–residue interactions in each MD frame. These data are further used for generation of ligand–residue interaction maps (LRIMs) for all 12 binding positions across all three simulation replicas (Fig. 2). These maps show the number of frames in which each amino acid of HSA interacts with the corresponding ligand. Peak height reflects the number of frames with interaction, while the vertical spacing between the lines represents different ligand positions within a single simulation and is scaled to 30 % of the total simulation time. Multiple simultaneous interactions between a single ligand and the same amino acid are possible and are captured in the diagrams.

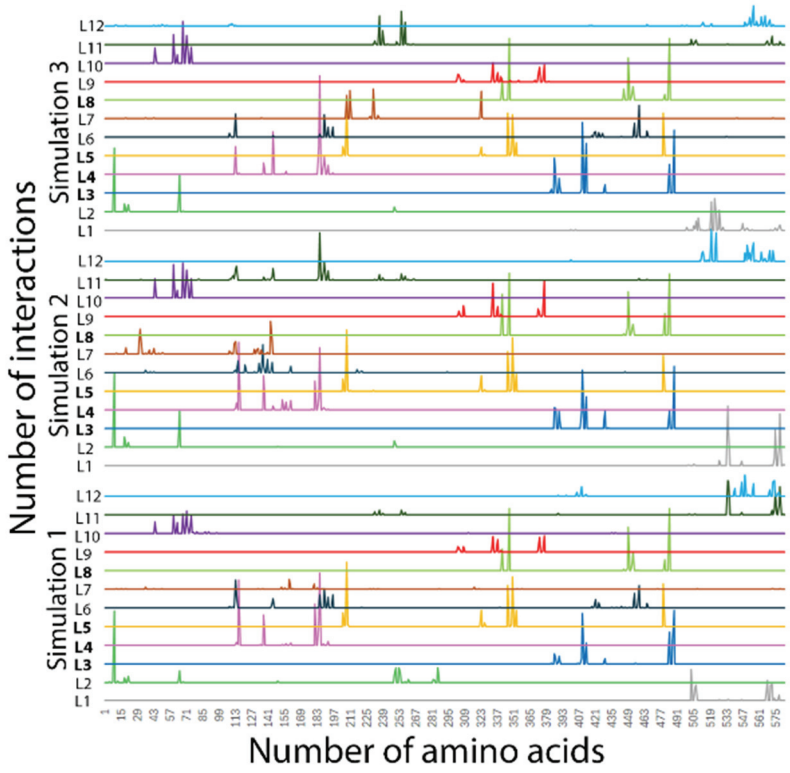

Fig. 2. Ligand–residue interaction maps (LRIMs) for ligands L1–L12 from three MD simulations. The *x*-axis shows amino acid positions, the *y*-axis the number of frames with contacts. Different colors mark individual ligands; peaks indicate residues frequently involved in binding.

Strongly bound ligands were defined using two criteria: 1) the ligand remained bound to the same site throughout all three simulations and 2) the ligand formed interactions with at least three different HSA amino acids for more than 50 % of the total simulation time. Applying these criteria yielded four binding sites corresponding to positions L3, L4, L5 and L8 from the docking study (Table I). Position L3 corresponds to the high-affinity site identified in crystallographic studies of HSA with PFOA and myristic acid, located at Sudlow's site II (FA4). Positions L4 and L5 correspond to FA1 and FA6, respectively; in the crystallographic study, FA1 was occupied by myristic acid, whereas FA6 was occupied by PFOA. Position L8 has not been previously reported as a PFOA binding site but corresponds to the FA3 site and it is also occupied with myristic acid in the crystal structure. Furthermore, the FA3 site is situated near Sudlow's site II.

To assess potential changes in ligand binding positions or orientations during simulations, *RMSD* values were calculated and *RMSD* plots were generated for all three simulations over the 1,000-ns interval. *RMSD* plots show that PFOA at positions L3 (FA4) and L8 (FA3) remain in the same orientation within the binding site thorough the simulation time with small *RMSD* values around 2 Å. However, a slight change in the orientation of the ligand at position L3 (FA4) was detected in one of the three simulations after 350 ns, as shown in Fig. 3. As noted previously, position L3 (FA4) is located at Sudlow's site II and lies in close proximity to position L8 (FA3). These two sites share a stabilizing residue, Arg485. The observed change in ligand orientation at position L3 (FA4), previously characterized as the highest-affinity PFOA binding site, is corelated to a conformational change of Arg485 side chain, which interacts with ligands at both positions in our simulations. In contrast, the binding at positions L4 (FA1) and L5 (FA6) shows higher *RMSD* values of around 5–8 Å, indicating more disordered binding sites and more conformational freedom for the ligand. Overall, the *RMSD* results support the conclusion that all four binding sites identified from the interaction diagrams are stable PFOA binding sites. RMSD profiles for all other ligand positions are provided in Fig. S-5 of the Supplementary material.

To further validate whether the four sites identified in our MD analysis represent true PFOA binding positions on HSA in the absence of competing ligands, we calculated binding free energies for all 12 positions using the MM-PBSA method (Table I). The calculated binding energy for position L3 (FA4), previously reported as the highest-affinity PFOA site, was below –62.76 kJ/mol, indicating very strong ligand binding. The binding energy for position L5 (FA6), described in earlier studies as a low-affinity PFOA site, was approximately 20.92 kJ/mol less favorable than position L3 (FA4), consistent with previous reports showing PFOA binding to both sites but with higher affinity at position L3 (FA4). In contrast, binding energies for positions L4 (FA1) and L8 (FA3) were more than 20.92 and

83.68 kJ/mol lower (*i.e.*, more favorable) than that of position L3 (FA4), respectively. Although crystallographic data indicate that myristic acid binds more strongly than PFOA at these sites, our results suggest that, in the absence of myristic acid, PFOA binding at FA1 (position L4) and FA3 (position L8) is actually stronger than at FA4 (position L3). MM-PBSA-calculated binding energies for PFOA at other eight positions are substantially lower; however, there are still indications that PFOA may bind at two additional positions: FA5 (position L1) and FA2 (position L2). Discrepancies between docking scores and MM-PBSA results, such as the case of L8 (FA3), highlight the limited predictive power of docking alone. Docking employs simplified scoring functions and rigid structures, whereas MD simulations with MM-PBSA incorporate conformational flexibility and dynamic interactions, offering a more reliable estimate of binding affinities.

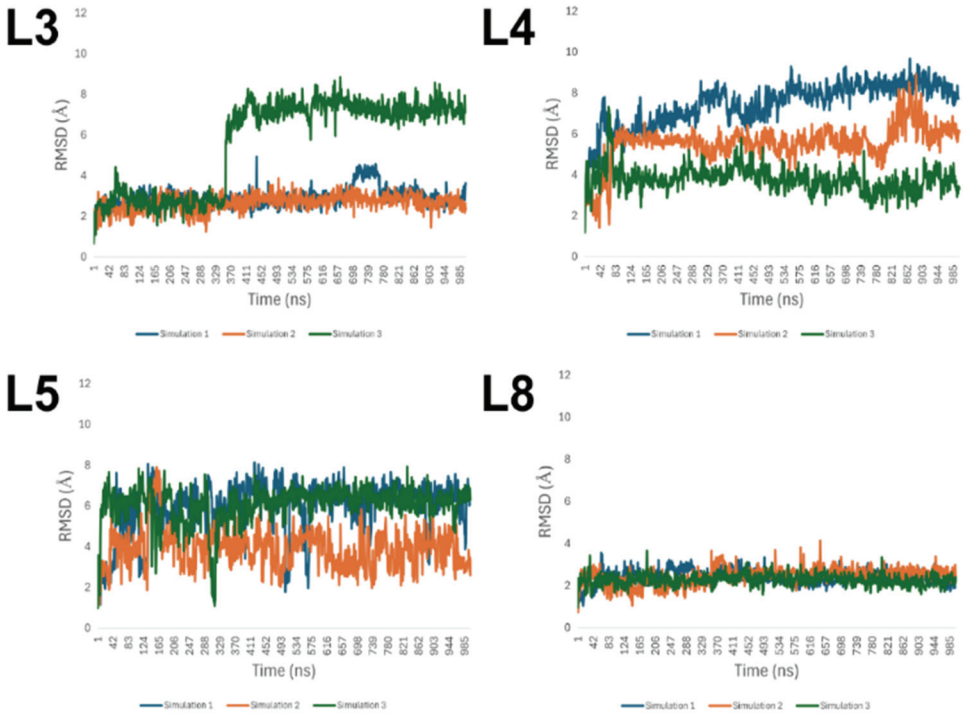

Fig. 3. RMSD plots for the four ligands of interest (L3, L4, L5 and L8) during 1,000-ns MD simulations.

Based on the combined analysis of MD trajectories, protein–ligand interaction profiles, *RMSD* values, and MM-PBSA-calculated binding energies, we conclude that, in the absence of competing ligands, PFOA preferentially binds to the four proposed binding sites. To further characterize these interactions, free-energy landscapes were constructed for ligands at each of these positions. The free energy

landscape for PFOA binding at position L8 (FA3) exhibits a well-defined single minimum, indicating a stable binding mode. In contrast, the landscape at position L3 (FA4) reveals two distinct minima, which arise from conformational changes of Arg485. These observations are in agreement with both the *RMSD* profiles and the calculated MM-PBSA binding energies. Conversely, the landscapes corresponding to positions L4 (FA1) and L5 (FA6) display more diffuse minima, consistent with their higher *RMSD* fluctuations and visual inspection of the MD trajectories (Fig. 4).

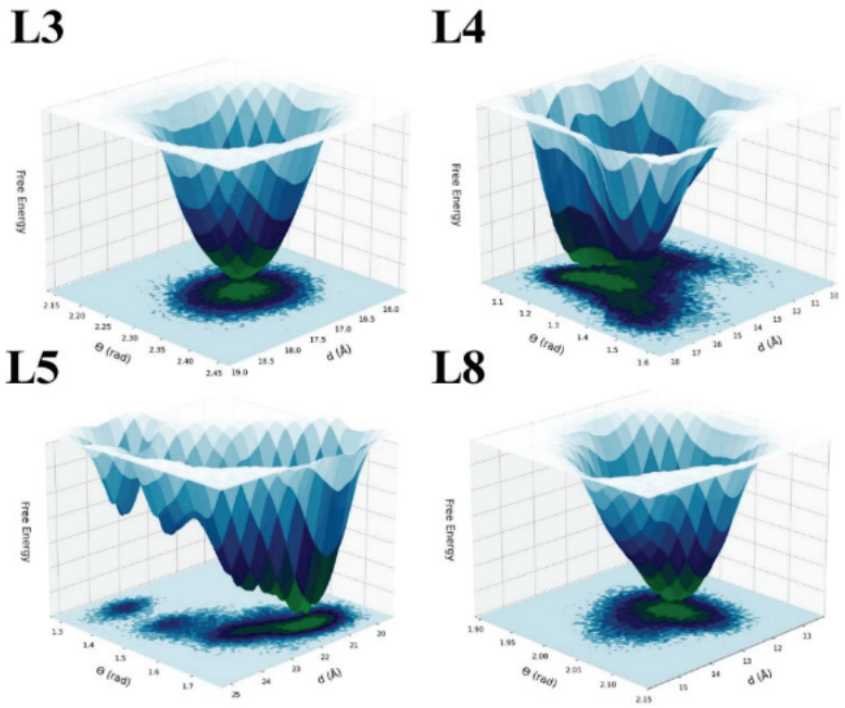

Fig. 4. Free-energy landscapes for best binding ligands (L3, L4, L5, L8).

To further characterize the molecular determinants of PFOA binding at the four identified sites, we employed the PLIP program[34] to track all protein–ligand interactions over the full MD trajectories. This analysis enables the identification of critical HSA residues involved in stabilizing PFOA at each site. Using these data, we constructed interaction diagrams illustrating the residues engaged in binding and the corresponding interaction types throughout the 1,000-ns simulations, including only those residues that interact with the ligand for more than 40 % of the simulation time (Fig. 5).

Our analysis shows that PFOA binding at the site with the most favorable MM-PBSA-calculated binding energy (FA3, L8) is primarily stabilized by two salt bridges formed with Arg347 and Arg485, both present in every frame of the 1,000-

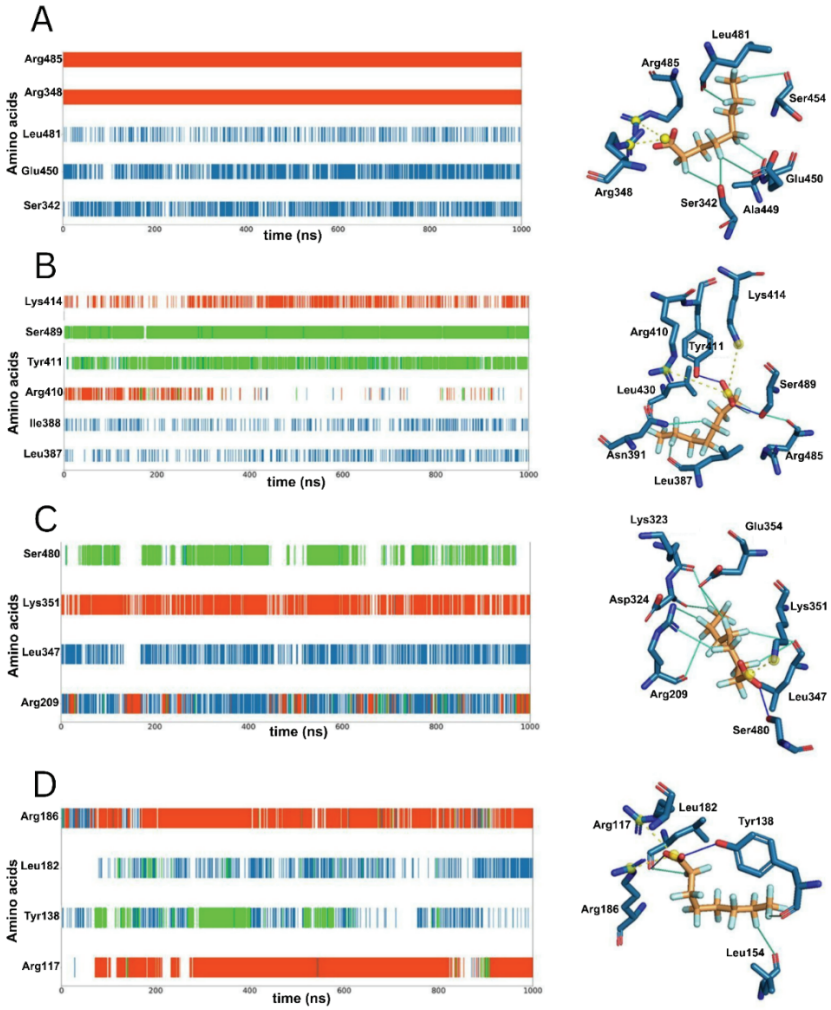

Fig. 5. Interactions formed by specific amino acid residues at the four identified PFOA binding sites on HSA. Panels A–D correspond to the key residues involved in binding L8, L3, L4 and L5, respectively. Left: interactions between protein residues and PFOA observed in at least 40 % of the 1,000-ns MD simulations. Orange bars indicate salt bridges, blue bars indicate halogen interactions, and green bars indicate hydrogen bonds. Right: three-dimensional representations of PFOA bound at each site, showing the interacting HSA residues.

-ns simulations. Additional stabilization is provided by halogen interactions with Ser342, Glu450 and Leu481 (Fig. 5A). Binding at the FA4 (L3) site is mediated

by a salt bridge with either Arg410 at the start of the simulation or Lys414, located in close proximity, later in the trajectory. This site also features two hydrogen bonds with Tyr411 and Ser489 curtail for stabilization of carboxylic group, as well as halogen interactions with Leu387 and Ile388 (Fig. 5B). At L4 position (FA6), the carboxyl group of PFOA is anchored by a persistent salt bridge with Lys351 and either an alternating hydrogen bond with Ser480 or a salt bridge with Arg209; when Ser480 forms a hydrogen bond, Arg209 predominantly engages in halogen interactions (Fig. 5C). Finally, the binding at L5 (FA1) is characterized by two salt bridges formed with Arg117 and Arg185, along with alternating halogen and hydrogen bond interactions involving Tyr138 and Leu182 (Fig. 5D).

CONCLUSION

In this study, we combined molecular docking with extensive molecular dynamics (MD) simulations to comprehensively map potential PFOA binding sites on human serum albumin (HSA). While previous crystallographic analyses in the presence of myristic acid identified one high-affinity and three low-affinity binding sites, our approach revealed twelve distinct binding poses, including six that have not been previously reported. Through ligand-residue interaction mapping, RMSD analysis, and MM-PBSA free energy calculations, we identified four binding sites (FA3 (L8), FA4 (L3), FA1 (L4) and FA6 (L5)) as the most likely PFOA binding positions in the absence of competing ligands.

Our simulations show that PFOA binding is stabilized by persistent salt bridges and hydrogen bonds between the carboxylic head group and protein residues, as well as halogen contacts between the PFOA tail and protein amino acids. Among the identified sites, FA3 (L8) exhibited the most favorable calculated binding energy. Notably, our results suggest that FA1 (L4) and FA3 (L8) may bind PFOA more strongly than the well-characterized FA4 (L3) site in the absence of myristic acid. The free-energy landscapes further confirmed the stability of PFOA at these sites, revealing well-defined minima at FA3 (L8) site, consistent with strong binding.

By integrating MD simulations with docking predictions, this work advances the current understanding of PFOA-HSA interactions beyond static structural models. These findings provide a more complete picture of the binding landscape, which can inform the rational design of biomimetic capture agents and guide strategies for environmental remediation. Future experimental validation of these predicted sites and binding affinities, such as site-directed mutagenesis of FA1/ /FA3 residues or by ITC and fluorescence displacement assays in the presence and absence myristic acid, will be essential to translate these computational insights into practical applications for PFOA detection and removal.

SUPPLEMENTARY MATERIAL

Additional data and information are available electronically at the pages of journal website: https://www.shd-pub.org.rs/index.php/JSCS/article/view/13509, or from the corresponding author on request.

Acknowledgements. This research was supported by the Science Fund of the Republic of Serbia, grant no. 7750288, "Tailoring Molecular Magnets and Catalysts Based on Transition Metal Complexes – TMMagCat". We also acknowledge the support of the Ministry of Science, Technological Development and Innovation of the Republic of Serbia (Contract Nos. 451-03-136/2025-03/200168 and 451-03-136/2025-03/200026).

ИЗВОД

МЕТОДОЛОШКИ ПРИСТУП ЗАСНОВАН НА МОЛЕКУЛСКОДИНАМИЧКИМ СИМУЛАЦИЈАМА ЗА ПОЈАШЊЕЊЕ МЕСТА ВЕЗИВАЊА PFOA НА HSA

АЛЕКСАНДРА М. ЂУРЂЕВИЋ ЂЕЛМАШ[1], ДАНИЛО ТРАЈКОВИЋ[1], КАРЛА МИЛЧИЋ[2] и МИЛОШ МИЛЧИЋ[1]

[1]Универзитет у Београду – Хемијски факултет, Студентски трг 12–16, 11158Београд и [2]Институт за хемију, технологију и металургију, Центар за хемију, Универзитет у Београду, Институт од националног значаја за Републику Србију, Његошева 12, 11000 Београд

Перфлуорооктаноична киселина (PFOA) је постојани загађивач животне средине који се снажно везује за хумани серумски албумин (HSA), утичући на њену дистрибуцију и токсикокинетику. Иако су кристалографске студије у присуству миристинске киселине идентификовале ограничен број везивних места високог афинитета, додатна места могу остати неоткривена због компететивног везивања. У овом раду смо комбиновали молекулско доковање високе резолуције са обимним симулацијама молекулске динамике (MD) како бисмо свеобухватно окарактерисали интеракције PFOA–HSA. Приступ са подељеним мрежама открио је дванаест непоклапајућих везивних позиција, укључујући шест претходно непознатих. Анализа интеракција лиганда и амино-киселина, *RMSD* анализа и прорачуни слободне енергије везивања методом MM/PBSA идентификовали су четири места, FA3, FA4, ФА1 и FA6, као најстабилнија везивна места PFOA у одсуству конкурентних лиганада. Међу њима, FA3 је показало најповољнију израчунату енергију везивања, док су FA1 и FA3 показала јаче везивање од добро окарактерисаног FA4 места у условима без миристинске киселине. Перзистентни сони мостови, водоничне везе и халогене интеракције идентификовани су као кључне стабилизујуће интеракције. Анализа енергетских пејзажа додатно је потврдила стабилност везивања PFOA на овим местима. Ови резултати пружају потпунији увид у везивни пејзаж PFOA на HSA и могу послужити као основа за дизајн биомиметичких хватача и развој стратегија за ремедијацију животне средине.

(Примљено 20. августа, ревидирано 27. августа, прихваћено 5. септембра 2025)

REFERENCES

1. X. Du, Y. Li, Y. L. Xia, S. M. Ai, J. Liang, P. Sang, X. L. Ji, S. Q. Liu, *Int. J. Mol. Sci.* **17** (2016) 144 (https://doi.org/10.3390/ijms17020144)
2. J. Kraut, *Science* **242** (1988) 533 (https://doi.org/10.1126/science.3051385)
3. D. B. Roche, S. J. Tetchner, L. J. McGuffin, *BMC Bioinformatics* **12** (2011) (https://doi.org/10.1186/1471-2105-12-160)

4. I. D. Kuntz, K. Chen, K. A. Sharp, P. A. Kollman, *PNAS* **96** (1999) 9997 (https://doi.org/10.1073/pnas.96.18.9997)
5. K. Henzler-Wildman, D. Kern, *Nature* **450** (2007) 964 (https://doi.org/10.1038/nature06522)
6. M. Held, P. Metzner, J. H. Prinz, F. Noé, *Biophys. J.* **100** (2011) 701 (https://doi.org/10.1016/j.bpj.2010.12.3699)
7. D. B. Roche, M. T. Buenavista, L. J. McGuffin, *PLoS One* **7** (2012) (https://doi.org/10.1371/journal.pone.0038219)
8. G. Fanali, A. Di Masi, V. Trezza, M. Marino, M. Fasano, P. Ascenzi, *Mol. Aspects Med.* **33** (2012) 209 (https://doi.org/10.1016/j.mam.2011.12.002)
9. S. Wang, S. Liu, Y. Zhang, J. He, D. H. Coy, L. Sun, *Health Sci. J.* **14** (2020) 698 (https://www.itmedicalteam.pl/articles/human-serum-albumin-hsa-and-itsapplications-as-a-drug-delivery-vehicle.pdf)
10. M. Forsthuber, A. M. Kaiser, S. Granitzer, I. Hassl, M. Hengstschläger, H. Stangl, C. Gundacker, *Environ. Int.* **137** (2020) 105324 (https://doi.org/10.1016/j.envint.2019.105324)
11. K. Li, P. Gao, P. Xiang, X. Zhang, X. Cui, L. Q. Ma, *Environ. Int.* **99** (2017) 43 (https://doi.org/10.1016/j.envint.2016.11.014)
12. K. Steenland, T. Fletcher, D. A. Savitz, *Environ. Health Perspect.* **118** (2010) 1100 (https://doi.org/10.1289/ehp.0901827)
13. L. Maso, M. Trande, S. Liberi, G. Moro, E. Daems, S. Linciano, F. Sobott, S. Covaceuszach, A. Cassetta, S. Fasolato, L. M. Moretto, K. De Wael, L. Cendron, A. Angelini, *Prot. Sci.* **30** (2021) 830 (https://doi.org/10.1002/pro.4036)
14. G. Moro, S. Liberi, F. Vascon, S. Linciano, S. De Felice, S. Fasolato, C. Foresta, L. De Toni, A. Di Nisio, L. Cendron, A. Angelini, *Chem. Res. Toxicol.* **35** (2022) 2049 (https://doi.org/10.1021/acs.chemrestox.2c00211)
15. M. Peng, Y. Xu, Y. Wu, X. Cai, W. Zhang, L. Zheng, E. Du, J. Fu, *Toxics* **12** (2024) 43 (https://doi.org/10.3390/toxics12010043)
16. Y.-D. Yang, N. Lu, R. Tian, *Int. J. Biol. Macromol.* **254** (2024) 128069 (https://doi.org/10.1016/j.ijbiomac.2023.128069)
17. J. Fan, A. Fu, L. Zhang, *Quant. Biol.* **7** (2019) 83 (https://doi.org/10.1007/s40484-019-0172-y)
18. V. Limongelli, *Wiley Interdiscip. Rev. Comput. Mol. Sci.* **10** (2020) e1455 (https://doi.org/10.1002/wcms.1455)
19. R. Anandakrishnan, B. Aguilar, A. V. Onufriev, *Nucleic Acids Res.* **40** (2012) W537 (https://doi.org/10.1093/nar/gks375)
20. G. M. Morris, H. Ruth, W. Lindstrom, M. F. Sanner, R. K. Belew, D. S. Goodsell, A. J. Olson, *J. Comput. Chem.* **30** (2009) 2785 (https://doi.org/10.1002/jcc.21256)
21. Gaussian, Inc., Wallingford, CT, 2016 (https://gaussian.com/citation/)
22. O. Trott, A. J. Olson, *J. Comput. Chem.* **31** (2010) 455 (https://doi.org/10.1002/jcc.21334)
23. C. Tian, K. Kasavajhala, K. A. A. Belfon, L. Raguette, H. Huang, A. N. Migues, J. Bickel, Y. Wang, J. Pincay, Q. Wu, C. Simmerling, *J. Chem. Theory. Comput.* **16** (2020) 528 (https://doi.org/10.1021/acs.jctc.9b00591)
24. J. Wang, R. M. Wolf, J. W. Caldwell, P. A. Kollman, D. A. Case, *J. Comput. Chem.* **25** (2004) 1157 (https://doi.org/10.1002/jcc.20035)
25. C. I. Bayly, P. Cieplak, W. D. Cornell, P. A. Kollman, *J. Phys. Chem.* **97** (1993) 10296 (https://doi.org/10.1021/j100142a004)

26. D. R. Roe, B. R. Brooks, *J. Chem. Phys.* **153** (2020) 054123 (https://doi.org/10.1063/5.0013849)
27. M. J. Abraham, T. Murtola, R. Schulz, S. Páll, J. C. Smith, B. Hess, E. Lindahl, *SoftwareX* **1**–**2** (2015) 19 (https://doi.org/10.1016/j.softx.2015.06.001)
28. A. Đurđević Đelmaš, T. Šeba, N. Gligorijević, M. Pavlović, M. Gruden, M. Nikolić, K. Milcic, M. Milčić, *Int. J. Biol. Macromol.* **306** (2025) 141425 (https://doi.org/10.1016/j.ijbiomac.2025.141425)
29. Y. Wu, J. Bao, Y. Liu, X. Wang, X. Lu, K. Wang, *Toxics* **12** (2024) 46 (https://doi.org/10.3390/toxics12010046)
30. A. M. Crisalli, A. Cai, B. P. Cho, *Chem. Res. Toxicol.* **36** (2023) 703 (https://doi.org/10.1021/acs.chemrestox.3c00011)
31. G. A. Tiburtini, L. Bertarini, M. Bersani, T. A. Dragani, B. Rolando, A. Binello, A. Barge, F. Spyrakis, *Arch. Toxicol.* **98** (2024) 3035 (https://doi.org/10.1007/s00204-024-03797-0)
32. M. Salvalaglio, I. Muscionico, C. Cavallotti, *J. Phy. Chem., B* **114** (2010) 14860 (https://doi.org/10.1021/jp106584b)
33. H. Chen, Q. Wang, Y. Cai, R. Yuan, F. Wang, B. Zhou, *Int. J. Environ. Res. Public Health* **17** (2020) 1319 (https://doi.org/10.3390/ijerph17041319)
34. S. Salentin, S. Schreiber, V. J. Haupt, M. F. Adasme, M. Schroeder, *Nucleic Acids Res.* **43** (2015) W443 (https://doi.org/10.1093/nar/gkv315).

Journal of the Serbian Chemical Society
JSCS@tmf.bg.ac.rs • www.shd.org.rs/JSCS
J. Serb. Chem. Soc. 91 (2) S61–S63 (2026) *Supplementary material*

SUPPLEMENTARY MATERIAL TO

Molecular dynamics-based methodological approach to clarify PFOA binding on human serum albumin

ALEKSANDRA M. ĐURĐEVIĆ ĐELMAŠ[1], DANILO P. TRAJKOVIĆ[1], KARLA MILČIĆ[2] and MILOŠ K. MILČIĆ[1]*

[1]*University of Belgrade – Faculty of Chemistry, Studentski trg 12–16, 11158 Belgrade, Serbia and* [2]*Institute of Chemistry, Technology and Metallurgy, Department of Chemistry, University of Belgrade, National Institute of the Republic of Serbia, Njegoševa 12, 11000 Belgrade, Serbia*

J. Serb. Chem. Soc. 91 (2) (2026) 129–144

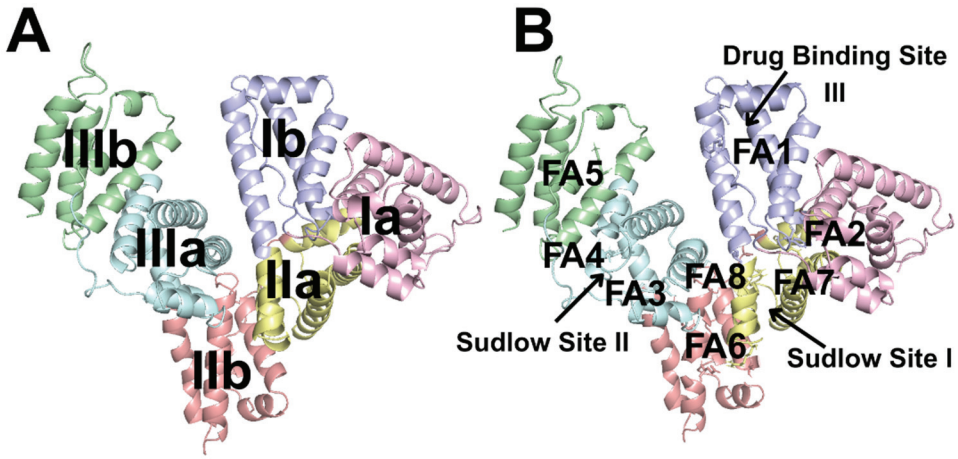

Figure S-1. *PyMOL* representation of the crystal structure of HSA (PDB: 1N5U). (A) The overall structure with subdomains highlighted: Domain Ia (light pink), Domain Ib (light blue), Domain IIa (light yellow), Domain IIb (salmon), Domain IIIa (pale cyan), and Domain IIIb (pale green). (B) Binding pockets relevant to ligand interactions are labeled, including eight fatty acid binding sites (FA1–FA8), two Sudlow's drug-binding sites (Sudlow's site I and II), and an additional drug-binding pocket. Binding site annotations are based on literature-reported positions.

* Correspondence E-mail: mmilcic@chem.bg.ac.rs

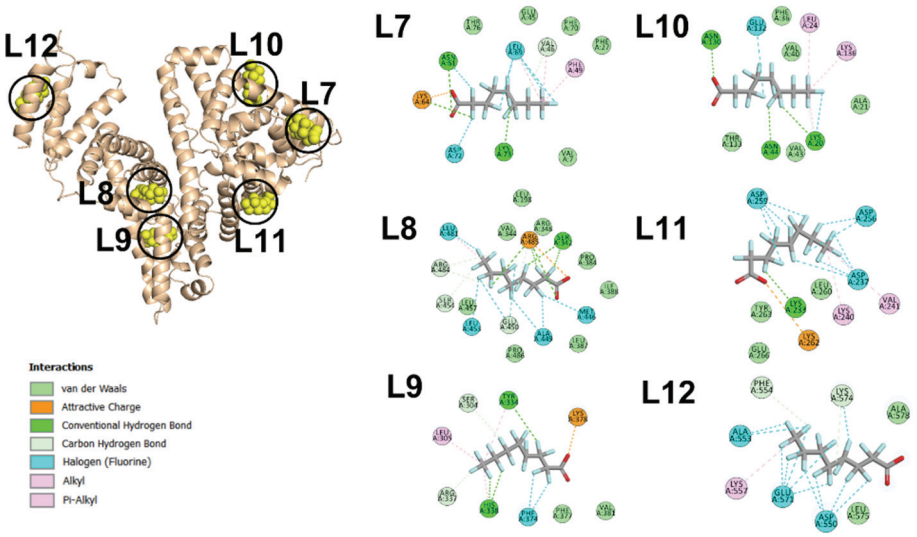

Figure S-2. Representation of docking poses with binding energies below –33.4 kJ/mol. Poses L7–L12 are shown on the HSA molecule (left), while the right panels present the interactions for each pose, as generated in the *Discovery Studio* program. The legend for the interaction types is provided below the depiction of the HSA crystal structure (PDB: 1N5U) with bound ligands.

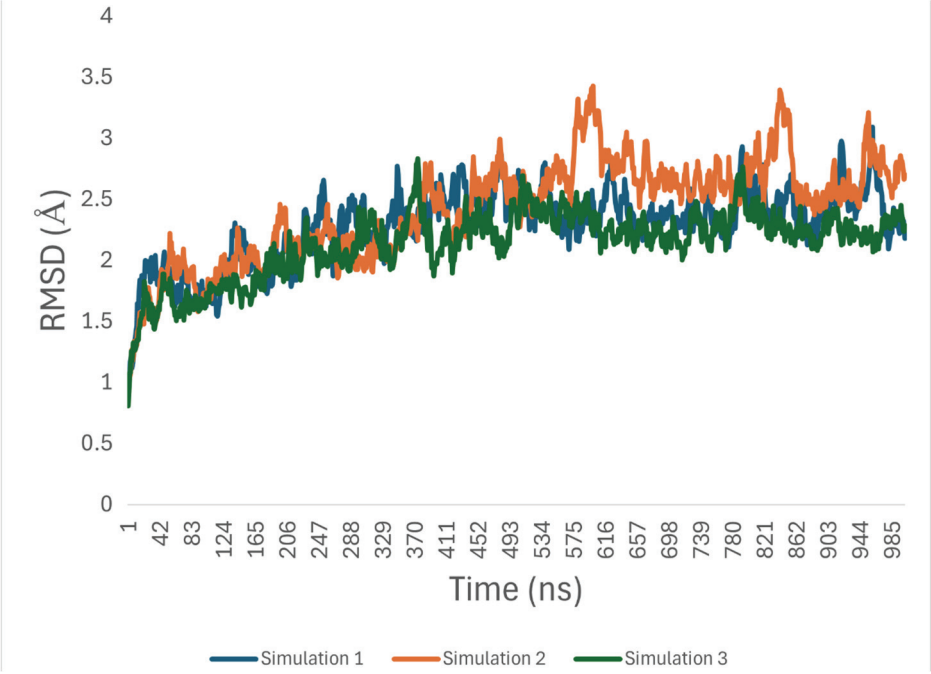

Figure S-3. RMSD of HSA during all three 1000-ns MD simulation.

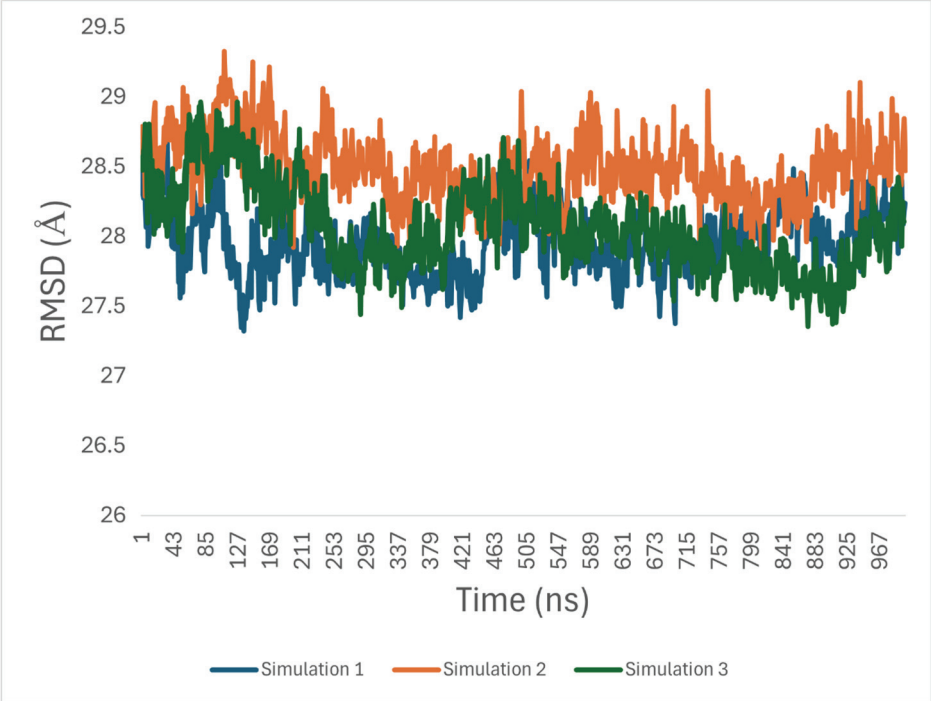

Figure S-4. Radius of gyration of HSA during all three 1000-ns MD simulation.

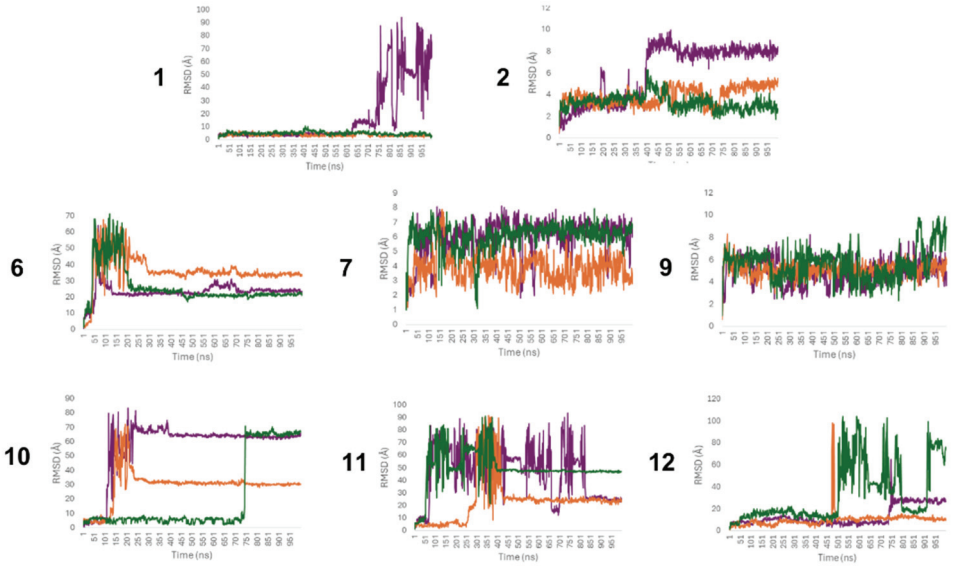

Figure S-5. RMSD plots for ligand (L) poses not selected as PFOA binding sites on HSA. The plots were generated from three independent MD simulations.

Journal of the Serbian Chemical Society
JSCS-info@shd.org.rs • www.shd.org.rs/JSCS
J. Serb. Chem. Soc. *91* (2) 145–159 (2026)
JSCS–5483
Original scientific paper
Published 16 February, 2026

A simple and feasible determination of the selective estrogen receptor modulator raloxifene in pharmaceutical formulation using pretreated boron-doped diamond electrode

ERTUĞRUL KESKİN[1]*, MUSA KIRAN[2] and YAVUZ YARDIM[2]**

[1]*Adıyaman University, Faculty of Pharmacy, Department of Analytical Chemistry, 02040 Adıyaman, Türkiye, and* [2]*Yüzüncü Yıl University, Faculty of Pharmacy, Department of Analytical Chemistry, 65080 Van, Türkiye*

(Received 18 July, revised 1 November, accepted 23 December 2025)

Abstract: This article reports on the development of an electroanalytical method for the quantitative determination of the selective estrogen receptor modulator raloxifene (RLX) using voltammetry at a pretreated boron-doped diamond (BDD) electrode. RLX exhibited irreversible cyclic voltammetric (CV) behavior in 0.04 mol L^{-1} Britton–Robinson (BR) supporting electrolyte at pH 2, generating two anodic oxidation peaks at approximately 0.79 V (P_{A1}) and 1.46 V (P_{A2}). Scan rate analysis revealed that both adsorption and diffusion mechanisms govern RLX transport to the electrode surface. Consequently, incorporating a preconcentration (deposition) step was hypothesized to enhance analytical sensitivity. Optimal deposition parameters, along with supporting electrolyte pH and square-wave voltammetry (SWV) modulation settings, were systematically optimized. Quantitative analysis was based on the first anodic peak (P_{A1}) in 0.04 mol L^{-1} BR buffer at pH 2, exhibiting a linear dynamic range from 0.025 to 5.0 μg mL^{-1} (from 4.9×10^{-8} to 9.9×10^{-6} mol L^{-1}) and a detection limit of 0.0073 μg mL^{-1} (1.4×10^{-8} mol L^{-1}). The method's applicability was validated by successfully quantifying RLX in pharmaceutical formulations.

Keywords: raloxifene; square-wave voltammetry; sensing; boron-doped diamond electrode; pharmaceutical formulation.

INTRODUCTION

Osteoporosis and breast cancer are among the most serious health issues affecting women.[1,2] The main cause of both problems is the lack of the estrogen hormone, which plays an important role in bone remodelling in postmenopausal women. This condition is characterized by an increased risk of fragility fractures due to deterioration of bone microarchitecture.[3,4] The conventional approach to

* Corresponding author. E-mail: (*)keskinertugrul@gmail.com; (**)yavuzyardim2002@yahoo.com
https://doi.org/10.2298/JSC250718094K

treating osteoporosis involves hormone replacement therapy (HRT), which has been proven effective through various studies.[5] However, reports indicate that HRT may be associated with adverse effects, including potential risks for cardiovascular diseases and an increased risk of breast cancer.[3] Additionally, breast cancer is the second most common type of cancer among women, following lung cancer, with over one million women diagnosed annually worldwide.[6,7] Increasingly, the use of selective estrogen receptor modulators (SERMs) has gained acceptance as an alternative to HRT in the management of these related conditions. SERMs provide the benefits of estrogen on bone health while potentially minimizing the adverse effects of estrogen in breast and other tissues.[8]

Raloxifene hydrochloride (RLX) is one of the most significant second-generation SERMs frequently prescribed for the prevention of postmenopausal osteoporosis, where it acts as an estrogen agonist, and for breast cancer treatment, where it acts as an estrogen antagonist.[9–11] Compared to other SERM drugs, RLX is associated with fewer side effects, making it a preferred choice among anti-cancer drugs.[12] Furthermore, the neuroprotective efficacy of RLX has also been demonstrated in animal models of age-related neurodegenerative disorders, such as Parkinson's disease.[13–15] There is an increasing need for robust, simple, rapid and reliable quantitative analytical methods to reliably monitor adverse effects resulting from overdoses of this medication, particularly in patients undergoing cancer treatment.

Several articles have been published on the quantitative analysis of RLX based on different analytical methodologies, including spectrophotometric methods,[16–19] chromatographic techniques[20–22] and capillary electrophoresis.[23] While these techniques offer selective and sensitive results, they also present several drawbacks such as requiring costly reagents, expensive instrumentation and time-consuming sample preparation. Another notable method for RLX analysis, based on resonance Rayleigh scattering, is characterized by multiple processing steps and the use of costly reagents.[24]

Electrochemical methods have become an important alternative to the above-mentioned analytical techniques due to their simplicity, speed, and cheap instrumentation.[25,26] Owing to the electroactive chemical structure of RLX (Scheme 1, 6-hydroxy-2-(4-hydroxyphenyl)-benzothiophene-3-yl]-[4-[2-(1-piperidyl)ethoxy]-phenyl]-methanone, there has been a growing number of quantitative analyses in recent years, particularly electrochemical ones. These studies have achieved varying sensitivity levels by using bare electrodes such as graphite[27] and glassy carbon electrodes (GCE)[28] as well as GCEs modified with carbon nanoparticles,[29] reduced graphene oxide–carbon nanotubes (rGOCNT),[30] graphene nanocomposite[31] and carbon paste electrodes (CPE) modified with carbon nanopowder,[32] nickel (II) oxide nanoparticles,[33] nanocomposites,[34] N–CQD/Fe_3O_4 nanoparticles.[35] Moreover, an electroanalytical study demonstrated the quantitative analysis of RLX can

be mentioned that performed the quantitative analysis of RLX at a sensitivity level of 3 nM on a PGE electrode modified with nanocomposite materials.[36]

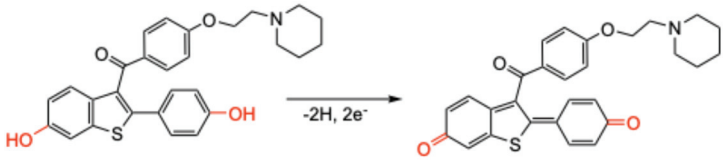

Scheme 1. Possible oxidation mechanism of RLX.

Boron-doped diamond electrodes offer numerous advantages for electrochemical analysis. Among these, the most prominent advantage is their wide potential window, which enables the analysis of a broad range of species.[37] Furthermore, these electrodes exhibit high electrochemical reactivity, enhancing analytical sensitivity and maintain low background currents that contribute to improved detection limits.[38] Their inert surface minimizes contamination, while their stability ensures consistent signals over extended periods. Additionally, their robust durability prolongs their service life, and their compatibility with portable systems further elevates their status as a preferred choice for electrochemical applications.[39]

Despite numerous reports on chemically modified electrodes for RLX, there is currently no advanced electroanalytical study that uses simple electrochemically pretreated boron-doped diamond (BDD) electrodes in combination with square-wave (SW) modulation for analyzing this chemotherapeutic agent. This study involves the optimization of the experimental conditions, elucidating the electrode reaction mechanism and determining the supporting electrolyte pH following a simple pretreatment of the working electrode. Subsequently, the analytical performance and selectivity of the proposed method are evaluated. Overall, this study shows great potential to stimulate future investigations into rapid, reliable, sensitive and cost-efficient electrochemical methods for detecting electroactive species, typically employing pretreated BDD electrodes.

EXPERIMENTAL

Chemicals and solutions

The raloxifen standard (raloxifen hydrochloride ReagentPlus®, 99.91 %) was obtained from ChemScene LLC (USA). No additional purification step was performed for this standard prior to the experiments. A solution of raloxifen hydrochloride (hereinafter referred to as RLX) at a concentration of 1.0 μg mL^{-1} was prepared in methanol. This solution was stored in a freezer at 4 °C when not in use, and exposure to direct light was also avoided during use. Britton–Robinson buffer (BR, 0.04 mol L^{-1}, pH 2–11) solution used in the experiments was prepared by dissolving 2.47 g of H_3BO_3 and adding 2.76 mL of 85 % H_3PO_4 and 2.29 mL of glacial acetic acid per liter of solution. The pH of the resulting mixture was adjusted to the desired value using 3 M NaOH and/or 3 M HCl. The preparation and dilution of the solutions were carried out using purified water obtained from a Millipore Milli-Q system (Millipore) with a resistivity of ≥18.2 MΩ·cm.

Apparatus and measurements

Electrochemical measurements were conducted using an Autolab type III electrochemical analyzer (Metrohm Autolab B.V., Utrecht, The Netherlands). The data were managed using the general-purpose electrochemical software (GPES, version 4.9). All square wave voltammograms were smoothed using a moving average filtering algorithm for baseline correction, followed by the Savitzky–Golay algorithm (peak width: 0.01 V). The experiments were performed in a three-electrode electrochemical cell equipped with an Ag/AgCl/ 3 mol L^{-1} NaCl reference electrode (BAS, model RE-1, USA), a commercially available BDD working electrode (with a 3 mm disk diameter and a claimed boron doping concentration of 1000 ppm, Windsor Scientific Ltd., UK), and a platinum wire auxiliary electrode (BAS, MW-4130, USA). pH measurements were recorded using an aWTWinoLab pH 720 m pH meter (Xylem, New York, USA) equipped with a combined glass-reference electrode at 25 °C.

At the beginning of each experimental day, the BDD electrode was electrochemically pretreated in 0.5 mol L^{-1} H_2SO_4. The pretreatment consisted of an anodic polarization step at 1.8 V for 180 s, followed by a cathodic polarization step at –1.8 V for 180 s, performed in a separate electrochemical cell. This procedure is known to produce oxygen-terminated and hydrogen--terminated surface characteristics, respectively.[40] After pretreatment, the electrode surface was gently polished using a polishing pad, rinsed with deionized water, and prepared for subsequent electrochemical measurements. During the day, only gentle polishing was applied between measurements, as no significant surface passivation was observed under the experimental conditions.

The electrochemical behavior of RLX in the supporting electrolyte used for the analyses, as well as the mechanism of driving forces such as diffusion and adsorption involved in the electrode reaction, were investigated using cyclic voltammetry (CV). Subsequently, the effects of supporting electrolyte pH, deposition parameters, and selected pulse technique (square-wave, SW) parameters on RLX signals were examined. Experimental and instrumental variables were optimized iteratively by selecting the conditions that produced the highest and best-shaped RLX responses; each parameter was optimized sequentially while holding the others constant. The analytical performance of the method, specifically the relationship between RLX concentration and its oxidation peak currents, was evaluated under the optimized conditions yielding the strongest signals. Finally, the practical applicability of the proposed method was demonstrated by analyzing RLX in tablet formulations.

Quantitative analyses of RLX were performed by immersing the three electrodes in a voltammetric cell containing RLX solution prepared in 0.04 mol L^{-1} BR buffer at pH 2 using the SW modulation technique. The potential was scanned from 0 to 1.3 V employing the same pulse technique. The SWV method was utilized for the quantitative evaluation of RLX. All measurements were performed in triplicate, except for the intraday repeatability assessment, which was conducted with ten repetitions.

Sample preparation

For real sample analyses, fixed dose combination tablets containing RLX HCl (Ralien®, Genveon Co., Türkiye) were obtained from a local pharmacy. The manufacturer declares that each tablet contains 60 mg RLX HCl. Ten tablets were first ground into powder using a mortar and pestle. An amount of the powder equivalent to 10 mg RLX hydrochloride was accurately weighed and transferred to a 250 mL volumetric flask, which was filled to volume with methanol. The contents of the flask were stirred for approximately 15 minutes to facilitate dissolution. Subsequently, a 100 μL aliquot of this solution was taken and added to a voltammetric

cell containing 0.04 mol L^{-1} BR buffer at pH 2 as supporting electrolyte. Analysis was performed on the same day as sample preparation in accordance with the recommended procedures, applying calibration curve method based on the relevant regression equation.

RESULTS AND DISCUSSION

Assessment of electrochemical behavior of RLX on pretreated BDD electrode

The cyclic voltammetry (CV) technique is used to determine the potential values at which electroactive species are reduced/oxidized and to determine which force dominates the transport of the electroactive compound to the electrode surface. For this purpose, three consecutive cyclic voltammograms (CVs) of 100 μg mL^{-1} RLX were recorded in the potential range from–0.7 to 1.80 V in 0.04 mol L^{-1} BR buffer solution at pH 2, which was established as the most suitable medium for analytical applications. The CV of the blank solution (without RLX) was also recorded for comparison. Fig. 1A shows two distinct oxidation peaks observed at approximately 0.79 V (P_{A1}, well-defined) and approximately 1.46 V (P_{A2}) in the first cycle of RLX and then a decrease in the intensity of these peaks in the following cycles.

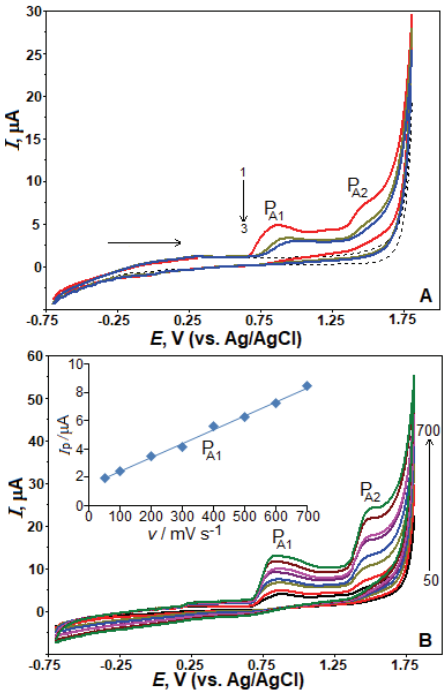

Fig. 1. Triplicate CVs of 100 μg mL^{-1} RLX obtained at a scan rate of 100 mV s^{-1} (A) and CV recordings of 100 μg mL^{-1} RLX at different scan rates (50, 100, 200, 300, 400, 500, 600 and 700 mV s^{-1}) (B).

This may be due to deactivation of the working electrode after contamination or the adsorption of RLX oxidation products on its surface. On the other hand, the

absence of any reduction signal in the subsequent reverse scan of the CV recordings can be considered as clear evidence that RLX on the BDD electrode is completely irreversible.

Effect of scan rate

In CV, the variation in peak currents of electroactive species at different scan rates is examined. These data enable predictions regarding the reaction kinetics of the examined species at the working electrode. In this context, the effect of the scan rate on the peak current of RLX was investigated using the BDD electrode in 0.04 mol L^{-1} BR buffer solution at pH 2 with scan rates ranging from 50 to 700 mV s^{-1} ($n = 8$ scans, Fig. 1B). As the first oxidation peak (P_{A1}) is more pronounced than the second (P_{A2}), the effect was investigated based on P_{A1} of RLX. As a result, a linear relationship was observed between the scan rate (v) and the peak current (i_p) of P_{A1}, as described by Equation 1:

$$i_{pA1}\ (\mu A) = 0.010 \pm 0.0003v\ (\text{mV s}^{-1}) + 1.423 \pm 0.0498, \quad r = 0.998 \qquad (1)$$

A similar linear relationship was observed between the i_p of the RLX and the $v^{1/2}$:

$$i_{pA1}\ (\mu A) = 0.331 \pm 0.0106v^{1/2}\ (\text{mV s}^{-1}) - 0.925 \pm 0.0324, \quad r = 0.98 \qquad (2)$$

These results indicate that both adsorption and diffusion phenomena contribute to RLX oxidation on the BDD electrode. Additionally, the relationship between the logarithm of the peak current and the logarithm of the scan rate was investigated, and a linear fit was obtained:

$$\log\ (i_p\ (\mu A)(= 0.563 \pm 0.0181 \log\ v\ (\text{mV s}^{-1}) - 0.721 \pm 0.0252, \ r = 0.988 \qquad (3)$$

The slope of this line (~0.56), lying between the expected values of 1 and 0.5 for adsorption- and diffusion-controlled processes, respectively, confirms the dual mechanism of RLX oxidation. Similar results were reported in our research team's previously published work.[40] Scan rate studies indicate that RLX adsorbs onto the BDD electrode surface and suggest that improved sensitivity can be achieved by applying deposition processes in the quantitative analysis of RLX. Therefore, such an approach is expected both to mitigate electrode surface fouling and enhance sensitivity in investigating RLX oxidation processes in aqueous solutions. In the later stages of the study, adsorption-based modulation (square wave-adsorptive stripping voltammetry, SW-AdSV) was preferred due to its excellent sensitivity and lower consumption of electroactive molecules.

The electrochemically active surface area of the BDD electrode was evaluated by CV in a 0.1 M KCl electrolyte containing 1.0 mM $K_3[Fe(CN)_6]$. CV measurements were collected at scan rates between 25 and 400 mV s^{-1}. The electroactive surface area was obtained from the linear relationship between the peak current (I_p) and the $v^{1/2}$, in accordance with the Randles–Ševčík equation:

$$I_p = (2.69\times10^5)n^{3/2}AD^{1/2}Cv^{1/2} \quad (4)$$

where I_p denotes the anodic peak current (A), n is the number of electrons involved in the redox process ($n = 1$), A represents the electroactive surface area (cm^2), D is the diffusion coefficient (7.6×10^{-6} cm^2 s^{-1}), C corresponds to the concentration of the redox probe (M) and v is the scan rate (V s^{-1}). Based on these parameters, the electrochemically active surface area of the BDD electrode was calculated to be 0.039 cm^2. This value is consistent with a previously published study.[41]

Effect of supporting electrolyte pH and the nature of reaction mechanism

It is well known that changing the pH of the supporting electrolyte also changes the response of the oxidation/reduction products of the electroactive species. This effect manifests both in the potential position of the peaks within the working potential window and in their current intensity. To investigate this influence more thoroughly, the effect of the BR supporting electrolyte on the RLX oxidation current at the BDD electrode was examined in the pH range of 2–11 (Fig. 2). The study was carried out using SW–AdSV in the potential range of 0 to 1.30 V for an RLX concentration of 2.5 μg mL^{-1}. As clearly seen in Fig. 3, the oxidation potentials of RLX shift toward more negative values with increasing pH. This observation provides evidence that RLX oxidation on the BDD electrode is pH-dependent. Conversely, a general decreasing trend in the peak currents of RLX oxidation signals is also observed as the pH increases. Moreover, the variation in the peak potential positions (E_p) of RLX oxidation as a function of the working solution's pH exhibited a linear correlation (inset of Fig. 2):

$$E_p\,(\mathrm{V}) = -\,0.055\mathrm{pH} + 0.862\,, \quad r = 0.993 \quad (5)$$

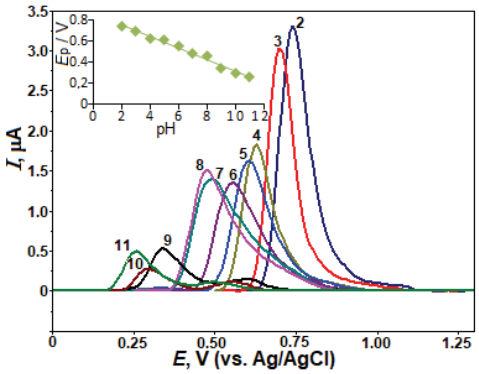

Fig. 2. SW-AdS voltammograms for 2.5 μg mL^{-1} RLX in BR buffer (pH 2–11) at the BDD electrode. At open circuit, the accumulation time is 30 s; the SWV parameters were as follows: f = 50 Hz; ΔE_s = 8 mV; ΔE_{sw} = 30 mV.

The slope of this linear correlation is 55 mV, which is close to the theoretical Nernstian value of 59 mV per pH unit. This can be interpreted as evidence that the number of protons and electrons involved in the RLX oxidation are equal.[42,43] Given the extant data and previously proposed mechanistic pathways, we posit that

RLX undergoes oxidation to the products depicted in Scheme 1 at the pretreated BDD electrode.[27,29]

Effect of accumulation variables

In processes where the adsorption significantly influences electrode kinetics, investigating the effects of accumulation parameters on the response of the electroactive species is an important step. Therefore, the effect of the accumulation time and accumulation potential on the electrochemical response of RLX were examined (data not shown). During these experiments, one parameter was kept constant while the other variable was varied. First, the accumulation potential was optimized under open circuit condition during the accumulation time ranging from 0 to 180 s for 2.5 μg mL^{-1} RLX in BR supporting electrolyte at pH 2 using the BDD electrode. The results indicated that the maximum peak current for RLX was achieved after 30 s of accumulation, with no significant increase observed at longer times. This suggests that the 30 s accumulation time was sufficient to adsorb the maximum amount of RLX onto the electrode surface. When longer deposition times were tested, RLX adsorption onto the electrode surface ceased, and the resulting current responses remained nearly unchanged.

The accumulation potential, the second accumulation parameter, was investigated over the range from 0.1 to 0.6 V as well as under open circuit conditions using the previously optimized accumulation time of 30 s. The results demonstrated that varying the accumulation potential, whether under open circuit conditions or applied potentials, did not significantly influence the oxidation peak currents of RLX. Therefore, subsequent experiments were conducted under open circuit conditions.

Optimization of SWV instrumental parameters

Optimizing the conditions that yield the highest peak current, considering chemical and accumulation variables, as well as SW modulation parameters such as frequency (f), ΔE_s and ΔE_{sw}, is critical for enhancing the anodic peak current. In SW modulation optimization, two of the three variables are held constant while the third is varied to obtain the highest and best-shaped peak current. The study proceeded by sequentially fixing the optimized value of one parameter and optimizing the others to achieve the best instrumental response. All instrumental optimizations were conducted under open circuit with a 30 s accumulation time in BR at pH 2. First, the frequency was varied from 50 to 125 Hz while the step potential and pulse amplitude were held constant at 8 and 30 mV, respectively. As the frequency value increased, the anodic peak current of RLX also increased, but peak broadening was observed beyond 100 Hz. Since the highest and most well-defined peak was obtained at 100 Hz, this frequency was selected for subsequent experiments. Next, with the frequency fixed at 100 Hz and the step potential at 8 mV, the

pulse amplitude was varied between 30 and 70 mV. The anodic peak current increased linearly with pulse amplitude; however, a significant broadening of the peak shape was noted beyond 60 mV. Therefore, 60 mV was chosen as the optimal pulse amplitude. Finally, with the frequency and pulse amplitude fixed at their optimized values, the step potential was varied between 8 and 14 mV. The anodic peak current increased up to 12 mV and then decreased thereafter. Hence, 12 mV was selected as the optimal step potential for further analytical studies. In conclusion, since the optimal instrumental parameters – 100 Hz frequency, 60 mV pulse amplitude and 12 mV step potential – yielded the best and highest peak currents, these values were adopted for subsequent stages of the study.

Analytical performance of the method

The functional applicability of the optimized experimental and instrumental parameters using the SW–AdS voltammetry method was evaluated by monitoring the change in peak current with increasing RLX concentration in 0.04 mol L^{-1} BR supporting electrolyte at pH 2. This was achieved by sequentially adding standard RLX solutions of varying concentrations to the voltammetric cell and recording the corresponding signals. Fig. 3 shows the changes in SW-AdS voltammograms of the RLX oxidation peak currents at 0.74 V with increasing standard RLX concentration. The RLX concentration was varied from 0.025 (4.9×10^{-8} mol L^{-1}) to 5 μg mL^{-1} (9.9×10^{-6} mol L^{-1}), with voltammograms recorded after each addition. The inset of Fig. 4 presents the calibration curve demonstrating a linear relationship between the anodic peaks and RLX concentration. A linear correlation, is obtained between the anodic peak signals and RLX concentration:

$$i_p\,(\mu A) = 2.576 \pm 0.0745c\,(\mu g\ mL^{-1}) + 0.273 \pm 0.0085\ (r = 0.999,\ n = 8) \quad (6)$$

In the linear equation, c indicates the RLX concentration, i_p indicates the anodic peak current, n represents the number of measurements, and r denotes the correlation coefficient.

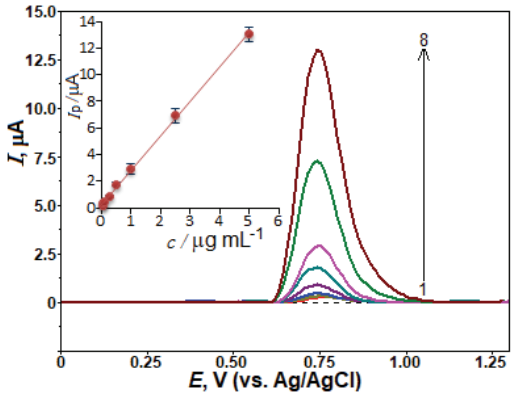

Fig. 3. SW-AdS voltammograms with RLX concentrations of 0.025, 0.05, 0.10, 0.25, 0.50, 1.0, 2.5 and 5.0 μg mL^{-1} (1–8) in BR buffer solution at pH 2 on the BDD electrode. The calibration graph for RLX measurement is shown inset. At open circuit, the accumulation time is 30 s, and the SWV parameters are as follows: f = = 100 Hz; ΔE_S = 12 mV; ΔE_{SW} = 60 mV.

Using this analytical curve, the detection limit (*LOD*) and quantification limit (*LOQ*) were calculated as 0.0073 (1.4×10^{-8} mol L^{-1}) and 0.025 μg mL^{-1} (4.9×10^{-8} mol L^{-1}), respectively. The $3s/m$ relation was used to calculate the detection limit, where s is the standard deviation of 10 measurements of the lowest concentration on the calibration line, and m is the slope of the corresponding calibration curve.[44] The analytical performance of the proposed method is compared with those of other previously published electrochemical analyses in Table I, which is arranged from the most sensitive to the least sensitive according to *LOD* values (except for our study, given in the last column). In electrochemical analyses, working electrodes are often functionalized with modifying agents to achieve better sensitivity;[28,32,34,35] however, some studies exhibit lower sensitivity compared to our results.[27,30,31,33] Achieving comparable sensitivity levels to a modified electrode in RLX analyses with a sample pre-treatment step-without any electrode modification-represents the most original and prominent aspect of the method.

TABLE I. Comparison of published electroanalytical methods for RLX detection; electrodes: graphene–CuO–polypyrrole/pencil graphite electrode, CPE/NiO/SWCNTs/1B4MPTFB; carbon paste electrode-nickel (II) oxide/single-walled carbon nanotubes/1-butyl–4-methylpyridinium tetrafluoroborate, N–CQD/Fe3O4/N–B-3-MITFB/CPE: N-CQD/Fe_3O_4 nanoparticles/ /*N*-butyl-3-methylimidazolium tetrafluoroborate, CNP/Mela/GCE; carbon nanoparticle/melamine/glassy carbon electrode, Nd_2O_5 NPs@GO; neodymium sesquioxide nanoparticles decorated graphene oxide nanocomposite, 1-M-3-OITFB/ZnO/CNTs/CPE; 1-methyl-3-octylimidazolium tetrafluoroborate/ZnO/CNTs nanocomposite, GCE, glassy carbon electrode, BDD, boron-doped diamond. Techniques: SWV, square wave voltammetry, DPV, differential pulse voltammetry; DPAdSV, differential pulse adsorptive stripping voltammetry; AdLSSV, adsorptive linear sweep stripping voltammetry; SW-AdSV, square wave adsorptive stripping voltammetry

Working electrode	Supporting electrolyte	Technique	Linear range μM	*LOD* nM	Analyzed samples	Ref.
GO–CuO–PP/PGE	PBS pH 2.5	SWV	40–320	3	Tablets, serum	36
CPE/NiO/SWCNTs/1B4MPTFB	PBS pH 7	SWV	0.03–520	7	Tablets, serum	33
N–CQD/Fe_3O_4/N–B-3-MITFB/CPE	PBS pH 5	DPV	0.04–320	10	Tablets, Urine	35
CNP/Mela/GCE	BR pH 3	DPAdSV	0.04–2	10	Tablets	29
Nd_2O_5 NPs@GO	PBS pH 7	Amperometry	0.03–472.5	18.43	Blood, urine	31
Carbon nanopowder/CPE	PBS pH 8	AdLSSV	0.001–40	19.5	Tablets, serum	32
1–M–3–OITFB/ZnO/CNTs/CPE	pH 8	DPV	0.08–400	40	Tablets, Urine	34
GCE	PBS pH 3	DPV	0.2–50	75	Tablets, plasma	28
BDD	BR pH 2	SW-AdSV	0.049–9.9	14	Tablets	This work

The precision of the method under the same conditions was investigated through intraday and inter-day repeatability experiments. The intraday repeatability of the anodic peak shapes was assessed by performing ten repetitions using 0.025 μg mL^{-1} of the RLX solution. An *RSD* value of 5.22 % shows that the method is repeatable. Additionally, the *RSD* value of 6.85 % for inter-day repeatability, measured at the same concentration and under the same conditions over five consecutive days, also serves as a clear indicator of the method's repeatability for analytical purposes.

Effect of interference

Before testing the applicability of the method on real samples, the effect of potential interfering species in drug formulations was investigated using SW--AdSV under the same test conditions and for 0.1 μg mL^{-1} RLX. The concentrations of interfering species causing ±5 % error in RLX peak currents were adopted as tolerable limit values. It was observed that inorganic ionic species such as calcium, magnesium, zinc, iron, titanium, potassium, sodium, chlorides, nitrates and sulphates did not have a noticeable effect on RLX signals even in the presence of a 50-fold excess concentrations of RLX. Similarly, the presence of sugars commonly used in drug formulations, such as mannitol, glucose, sucrose and fructose, at a 50-fold excess concentration did not have a significant effect on RLX signals. Finally, drug additives such as microcrystalline cellulose, corn starch and magnesium stearate, even at excessive concentrations (50-fold), did not alter RLX signals. These findings show that the proposed method has a high degree of selectivity and can be successfully applied to commercially available pharmaceutical formulations.

Applicability of the method on real samples

In the final stage, the practical applicability of the developed method was tested for the detection of RLX in commercially available drug formulations (Fig. 4). The detailed procedure for drug sample preparation and subsequent evaluation is described in the Experimental section. After spiking the drug samples with standard RLX solutions, it was found that each tablet contained 56.9 mg RLX (3.3 % *RSD*), which is very close to the 60 mg value declared by the manufacturer.

To verify the proposed method, a recovery study was conducted. This study involved spiking RLX standard solutions into the drug sample solution in the voltammetric cell at final concentrations of 0.1, 0.25 and 0.5 μg mL^{-1}. The *RSD* values obtained from three replicate measurements are presented in Table II. The satisfactory recovery results demonstrate that the proposed method can be effectively applied to the analysis of RLX in tablet formulations without a significant matrix effect.

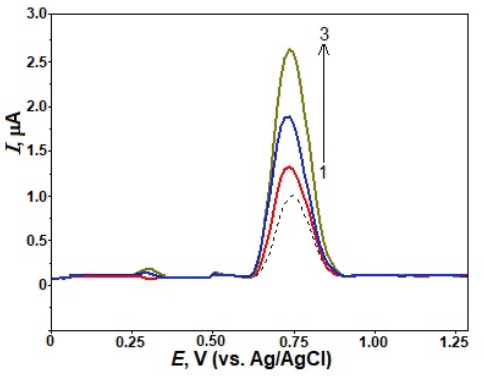

Fig. 4. SW-AdS voltammograms of a diluted pharmaceutical formulation (dashed lines) as well as standard additions to create the final concentration values of 0.1, 0.25, and 0.50 µg mL^{-1} (1–3) RLX in BR buffer solution at pH 2. The other working conditions are depicted in Fig. 4.

TABLE II. Recovery values of pharmaceutical formulations samples spiked with RLX standard solutions using the proposed voltammetric method

Added,[a] µg mL^{-1}	Expected,[a] µg mL^{-1}	Found,[a,b] µg mL^{-1}	Recovery ± *RSD*, %
0	–	0.237	±3.3
0.1	0.337	0.361	107.1±3.1
0.25	0.487	0.493	101.2±2.8
0.50	0.737	0.689	93.5±2.5

[a]Concentration in the measured solution; [b]average of three replicate measurements

CONCLUSION

This study describes a procedure for applying a mechanical cleaning process to the BDD electrode following anodic and cathodic pretreatment steps, respectively, before employing it for the quantitative analysis of RLX. The electrochemical behavior of RLX was elucidated using CV, while quantitative analysis was conducted based on SW modulation. Considering that adsorption, in addition to diffusion, influences the transport of RLX to the electrode surface, the effect of deposition parameters on the quantitative analysis was examined, and optimum conditions were identified. After a simple pretreatment of the BDD electrode, a linear working range of 0.025 to 5 µg mL^{-1} and a detection limit value of 0.0073 µg mL^{-1} (1.4×10^{-8} mol L^{-1}) were achieved under optimized experimental conditions, including the deposition step and the best SW modulation parameters. The method proposed herein offers a simpler and more rapid electrode preparation compared to electrochemical analysis techniques based on modified electrodes for RLX detection. It also presents advantages in terms of ease of use and cost-effectiveness, avoiding the laborious electrode preparation processes commonly required. Compared to other analytical approaches, this method provides a cost-efficient and straightforward alternative for RLX analysis with simpler instrumentation and procedure. Furthermore, the electrochemical protocol in this study demonstrates

good sensitivity for analyzing other electroactive species, such as active pharmaceutical ingredients and environmental contaminants, making it a promising candidate as an alternative method for rapid and economical future solutions.

Acknowledgement. The authors gratefully acknowledge financial support from the Adıyaman University Scientific Research Project Unit (Project number: ECZFMAP/2018-0001).

ИЗВОД

ЈЕДНОСТАВНО И ИЗВОДЉИВО ОДРЕЂИВАЊЕ СЕЛЕКТИВНОГ МОДУЛАТОРА ЕСТРОГЕНСКИХ РЕЦЕПТОРА РАЛОКСИФЕНА У ФАРМАЦЕУТСКОЈ ФОРМУЛАЦИЈИ КОРИШЋЕЊЕМ ПРЕТХОДНО ТРЕТИРАНЕ ДИЈАМАНТСКЕ ЕЛЕКТРОДЕ ДОПОВАНЕ БОРОМ

ERTUĞRUL KESKİN[1], MUSA KIRAN[2] и YAVUZ YARDIM[2]

[1]Adıyaman University, Faculty of Pharmacy, Department of Analytical Chemistry, 02040 Adıyaman, Türkiye, и [2]Yüzüncü Yıl University, Faculty of Pharmacy, Department of Analytical Chemistry, 65080 Van, Türkiye

У овом раду се приказује развој електроаналитичке методе за квантитативно одређивање селективног модулатора естрогенских рецептора ралоксифена (RLX) коришћењем волтаметрије на претходно третираној дијамантској електроди допованој бором (BDD). Циклична волтаметрија RLX је показала иреверзибилно понашање у Britton–Robinson (BR) основном електролиту концентрације 0,04 mol L^{-1} и вредности pH 2, при чему су добијена два анодна оксидациона пика на приближно 0,79 (P_{A1}) и 1,46 V (P_{A2}). Зависност волтамограма од брзине скенирања је показала да је транспорт RLX до површине електроде одређен и адсорпцијом и дифузијом. Сходно томе, претпостављено је да би се аналитичка осетљивост повећала укључивањем ступња претходне концентрације (таложења). Оптимални параметри таложења, заједно са pH вредношћу електролита и модулацијом параметара волтаметрије са правоугаоним сигналом (SWV) су систематски оптимизовани. Квантитативна анализа је заснована на анодном пику P_{A1} у BR пуферу концентрације 0,04 mol L^{-1} при pH 2, и показала је линеарни динамички опсег од 0,025 до 5,0 μg mL^{-1} (4,9×10^{-8} до 9,9×10^{-6} mo L^{-1}) и границу детекције од 0,0073 μg mL^{-1} (1,4·10^{-8} L^{-1}). Применљивост методе је потврђена успешном квантификацијом RLX у фармацеутским формулацијама.

(Примљено 18. јула, ревидирано 1. новембра, прихваћено 23. децембра 2025)

REFERENCES

1. Y. Wu, X. Jin, E. Ashrafzadeh Afshar, M. A. Taher, C. Xia, S. W. Joo, T. Mashifana, Y. Vasseghian, *Chemosphere* **305** (2022) 135392 (https://doi.org/10.1016/j.chemosphere.2022.135392)
2. I. Bozovic-Spasojevic, E. Azambuja, W. McCaskill-Stevens, P. Dinh, F. Cardoso, *Cancer Treat. Rev.* **38** (2012) 329 (https://doi.org/10.1016/j.ctrv.2011.07.005)
3. M. D. Ansari, I. Khan, P. Solanki, J. Pandit, R. N. Jahan, M. Aqil, Y. Sultana, *J. Drug Deliv. Sci. Technol.* **68** (2022) 103102 (https://doi.org/10.1016/j.jddst.2022.103102)
4. T. Sözen, L. Özışık, N. Çalık Başaran, *Eur. J. Rheumatol.* **4** (2017) 46 (https://pmc.ncbi.nlm.nih.gov/articles/PMC5335887/)
5. M. Gass, B. Dawson-Hughes, *Am. J. Med.* **119** (2006) S3 (https://doi.org/10.1016/j.amjmed.2005.12.017)

6. A. S. Abu Lila, M. H. Abdallah, S. U. D. Wani, H. V. Gangadharappa, K. M. Younes, E. S. Khafagy, T. M. Shehata, M. S. Soliman, *Colloids Surfaces, A* **625** (2021) 126971 (https://doi.org/10.1016/j.colsurfa.2021.126971)
7. A. Jemal, R. Siegel, E. Ward, Y. Hao, J. Xu, M. J. Thun, *CA Cancer. J. Clin.* **59** (2009) 225 (https://doi.org/10.3322/caac.20006)
8. B. H. Mitlak, F. J. Cohen, *Drugs* **57** (1999) 653 (https://doi.org/10.2165/00003495-199957050-00001)
9. G. Y. Stokes, J. C. Conboy, *J. Am. Chem. Soc.* **136** (2014) 1409 (https://doi.org/10.1021/ja409250y)
10. R. Abdelhamid, J. Luo, L. VandeVrede, I. Kundu, B. Michalsen, V. A. Litosh, I. T. Schiefer, T. Gherezghiher, P. Yao, Z. Qin, G. R. J. Thatcher, *ACS Chem. Neurosci.* **2** (2011) 256 (https://doi.org/10.1021/cn100106a)
11. H. D. Nelson, M E Beth Smith, J. C. Griffin, R. Fu, *Ann. Int. Med.* **158** (2013) 604 (https://doi.org/10.7326/0003-4819-158-8-201304160-00005)
12. M. Y. Williams-Brown, S. M. Salih, X. Xu, T. D. Veenstra, M. Saeed, S. K. Theiler, C. R. Diaz-Arrastia, S. A. Salama, *J. Steroid Biochem. Mol. Biol.* **126** (2011) 78 (https://doi.org/10.1016/j.jsbmb.2011.05.001)
13. A. M. Baraka, A. A. Korish, G. A. Soliman, H. Kamal, *Life Sci.* **88** (2011) 879 (https://doi.org/10.1016/j.lfs.2011.03.010)
14. A. A. Poirier, M. Côté, M. Bourque, M. Morissette, T. Di Paolo, D. Soulet, *Neurobiol. Aging* **48** (2016) 61 (https://doi.org/10.1016/j.neurobiolaging.2016.08.004)
15. M. Bourque, M. Morissette, T. Di Paolo, *Neurobiol. Aging* **35** (2014) 2347 (https://doi.org/10.1016/j.neurobiolaging.2014.03.017)
16. Y. Wu, X. Jin, E. Ashrafzadeh Afshar, M. A. Taher, C. Xia, S. W. Joo, T. Mashifana, Y. Vasseghian, *Chemosphere* **305** (2022) 135392 (https://doi.org/10.1016/j.chemosphere.2022.135392)
17. F. Ibrahim, N. El-Enany, R. El-Shaheny, I. Mikhail, *J. Mol. Liq.* **252** (2018) 408 (https://doi.org/10.1016/j.molliq.2018.01.005)
18. K. Basavaiah, K. Tharpa, U. R. Anil Kumar, N. Rajedraprasad, S. G. Hiriyanna, K. B. Vinay, *Arch. Pharm. Res.* **32** (2009) 1271 (https://doi.org/10.1007/s12272-009-1913-7)
19. J. Dharuman, V. Ravichandran, N. Thirumoorthy, A. Dharamsi, *Pharmazie* **59** (2004) 720 (https://www.ingentaconnect.com/contentone/govi/pharmaz/2004/00000059/00000009/art00013)
20. K. Basavaiah, U. R. A. Kumar, K. Tharpa, *Acta Pharmaceutica* **58** (2008) 347 (https://doi.org/10.2478/v10007-008-0018-z)
21. J. Trontelj, T. Vovk, M. Bogataj, A. Mrhar, *Pharmacol. Res.* **52** (2005) 334 (https://doi.org/10.1016/j.phrs.2005.05.007)
22. J. Zweigenbaum, J. Henion, *Anal. Chem.* **72** (2000) 2446 (https://doi.org/10.1021/ac991413p)
23. T. Pérez-Ruiz, C. Martínez-Lozano, A. Sanz, E. Bravo, *J. Pharm. Biomed. Anal.* **34** (2004) 891 (https://doi.org/10.1016/j.jpba.2003.12.008)
24. S. P. Liu, Y. Q. He, Z. F. Liu, L. Kong, Q. M. Lu, *Anal. Chim. Acta* **598** (2007) 304 (https://doi.org/10.1016/j.aca.2007.06.054)
25. E. Keskin, A. S. Ertürk, *Ionics (Kiel)* **24** (2018) 4043 (https://doi.org/10.1007/s11581-018-2532-4)

26. M. Ghalkhani, N. K. Bakirhan, S. A. Ozkan, *Crit. Rev. Anal. Chem.* **50** (2020) 538 (https://doi.org/10.1080/10408347.2019.1664281)
27. X. Q. Li, J. B. He, L. Liu, T. Cui, *Electrochim. Acta* **96** (2013) 74 (https://doi.org/10.1016/j.electacta.2013.02.069)
28. A. Bagheri, H. Hosseini, *Bioelectrochemistry* **88** (2012) 164 (https://doi.org/10.1016/j.bioelechem.2012.03.007)
29. S. Shahrokhian, M. Ghalkhani, H. Balotf, R. Salimian, *J. Electroanal. Chem.* **780** (2016) 126 (https://doi.org/10.1016/j.jelechem.2016.09.012)
30. M. Ghalkhani, S. Shahrokhian, M. Navabi, *Mater. Chem. Phys.* **263** (2021) 124131 (https://doi.org/10.1016/j.matchemphys.2020.124131)
31. T. W. Chen, J. Princy Merlin, S. M. Chen, S. Anandaraj, M. S. Elshikh, T. W. Tseng, K. Wang, D. Qi, J. Jiang, *Ultrason. Sonochem.* **64** (2020) 104717 (https://doi.org/10.1016/j.ultsonch.2019.104717)
32. N. L. Teradal, R. D. Tandel, J. Seetharamappa, *Mater. Sci. Energy Technol.* **2** (2019) 337 (https://doi.org/10.1016/j.mset.2019.02.007)
33. S. Salmanpour, A. Sadrnia, F. Karimi, N. Majani, M. L. Yola, V. K. Gupta, *J. Mol. Liq.* **254** (2018) 255 (https://doi.org/10.1016/j.molliq.2018.01.105)
34. S. Cheraghi, M. A. Taher, H. Karimi-Maleh, *Appl. Surf. Sci.* **420** (2017) 882 (https://doi.org/10.1016/j.apsusc.2017.05.218)
35. F. Shalali, S. Cheraghi, M. A. Taher, *Mater. Chem. Phys.* **278** (2022) 125658 (https://doi.org/10.1016/j.matchemphys.2021.125658)
36. M. Fouladgar, H. Karimi-Maleh, F. Opoku, P. P. Govender, *J. Mol. Liq.* **311** (2020) 113314 (https://doi.org/10.1016/j.molliq.2020.113314)
37. R. R. Swara, A. I. M. Rahma, C. Y. Kharismasari, D. A. Wulandari, S. N. Zakiyyah, Y. Einaga, Y. W. Hartati, Irkham, *Clin. Chim. Acta* **574** (2025) 120285 (https://doi.org/10.1016/j.cca.2025.120285)
38. F. Zouaoui, G. Menassol, C. Ducros, P. Mailley, Y. Thomas, *Microchem. J.* **209** (2025) 112650 (https://doi.org/10.1016/j.microc.2025.112650)
39. T. Kondo, *Curr. Opin. Electrochem.* **32** (2022) 100891 (https://doi.org/10.1016/j.coelec.2021.100891)
40. H. İ. Özok, S. Allahverdiyeva, Y. Yardım, Z. Şentürk, *Electroanalysis* **34** (2022) 1487 (https://doi.org/10.1002/elan.202100654)
41. S. Allahverdiyeva, E. Keskin, P. T. Pınar, O. Yunusoğlu, Y. Yardım, Z. Şentürk, *Diam. Relat. Mater.* **108** (2020) 107962 (https://doi.org/10.1016/j.diamond.2020.107962)
42. N. Milhazes, P. Martins, E. Uriarte, J. Garrido, R. Calheiros, M. P. M. Marques, F. Borges, *Anal. Chim. Acta.* **596** (2007) 231 (https://doi.org/10.1016/j.aca.2007.06.027)
43. Ľ. Švorc, M. Vojs, P. Michniak, M. Marton, M. Rievaj, D. Bustin, *J. Electroanal. Chem.* **717**–**718** (2014) 34 (https://doi.org/10.1016/j.jelechem.2014.01.008)
44. H. B. Ammar, M. Ben Brahim, R. Abdelhédi, Y. Samet, *Mater. Sci. Engi., C* **59** (2016) 604 (https://doi.org/10.1016/j.msec.2015.10.025).

Journal of the Serbian Chemical Society
JSCS-info@shd.org.rs • www.shd.org.rs/JSCS
J. Serb. Chem. Soc. *91* (2) 161–179 (2026)
JSCS–5484
Original scientific paper
Published 12 February, 2026

A comparative study of ketoprofen-loaded microparticles prepared using emulsion-congealing and solvent evaporation techniques

HADJER SEBAIHI[1], WASSILA BENSALAH[2], KARIMA BADIS[1] and MERINE HAOUARIA[1]*

[1]*Laboratory of Macromolecular Physical and Organic Chemistry, Faculty of Exact Sciences, University of Djillali Liabes, Sidi Bel-Abbes, Algeria and* [2]*Laboratory for the Application of Organic Electrolytes and Polyelectrolytes (LAEPO), University of Tlemcen, B.P. 119, 13000 Tlemcen, Algeria*

(Received 7 September, revised 10 November, accepted 18 December 2025)

Abstract: Ketoprofen (Ket) is a commonly used non-steroidal anti-inflammatory drug (NSAID) with analgesic and anti-inflammatory properties. However, its poor aqueous solubility and short biological half-life limit its therapeutic efficacy and patient compliance. Controlled-release microparticles offer a strategy to prolong drug release and improve bioavailability. In this study, we prepared ketoprofen-loaded microparticles using two microencapsulation techniques: emulsion/congealing with beeswax and solvent evaporation with cellulose acetate butyrate (CAB). We then tailored co-matrices containing hydrophobic components (PMMA and PCL) and hydrophilic components (HPMC and *β*-cyclodextrin) to modulate drug release. Microparticles based on beeswax, particularly when combined with PMMA, exhibited slower release due to reduced matrix permeability. Including hydrophilic excipients in beeswax-based microparticles accelerated the release of ketoprofen by promoting water penetration and drug solubilization. By contrast, the incorporation of hydrophilic excipients into CAB-based microspheres slightly decreased drug release, probably because a denser matrix structure formed during solvent evaporation. These results demonstrate that the encapsulation method and matrix composition both critically influence ketoprofen release kinetics, providing guidance for the rational design of controlled-release drug delivery systems.

Keywords: ketoprofen; encapsulation techniques; beeswax micropellets; cellulose acetate butyrate microspheres; controlled release.

* Corresponding author E-mail: merine_houaria@yahoo.fr
https://doi.org/10.2298/JSC250907093H

INTRODUCTION

Ketoprofen (Ket), a non-steroidal anti-inflammatory drug (NSAID), is widely used in clinical practice for its analgesic, antipyretic and anti-inflammatory properties.[1] In particular, it is prescribed to relieve symptoms associated with chronic conditions such as osteoarthritis, rheumatoid arthritis, ankylosing spondylitis and dysmenorrhea.[2] Despite its clinical efficacy, ketoprofen has several pharmaceutical limitations, most notably its poor water solubility and short biological half-life (approximately 2–3 h).[3] These pharmacokinetic properties result in a rapid decline in plasma concentration following administration, necessitating frequent dosing to maintain therapeutic levels.[4] Such a regimen may result in decreased patient compliance and increased risk of adverse effects, including gastrointestinal irritation-a common concern with NSAIDs.[5,6]

To overcome these limitations, oral controlled release (CR) formulations have been extensively studied as a solution to prolong therapeutic effect, reduce dosing frequency and improve patient adherence.[7–9] Controlled release systems offer the added benefit of minimizing peak-trough fluctuations in plasma drug concentrations, thereby improving therapeutic outcomes and reducing side effects.[9] Among the various approaches being explored, multiparticulate drug delivery systems such as microspheres, microcapsules, micropellets, tablets and granules have received significant attention due to their potential to offer customizable release profiles, ease of administration, and better gastrointestinal tolerability compared to monolithic dosage forms.[6,8,10–16]

The success of these systems is highly dependent on the selection of appropriate polymer matrices, which dictate the release kinetics and stability of the encapsulated drug.[17] Both hydrophilic and hydrophobic polymers have been used to formulate matrix-based or membrane-coated delivery systems. Hydrophilic polymers, particularly cellulose derivatives such as hydroxypropyl methylcellulose (HPMC), hydroxypropyl cellulose (HPC), cellulose acetate (CA), carboxymethyl ethyl cellulose (CMEC), ethyl cellulose (EC) and methyl cellulose (MC), have attracted considerable interest due to their swelling and gel-forming capabilities in aqueous media.[18,19] These properties allow them to control water penetration and drug diffusion, which are essential mechanisms for sustained drug release.[20–25]

On the other hand, hydrophobic polymers such as poly(lactic-co-glycolic acid) (PLGA),[26] poly(ε-caprolactone) (PCL)[21,22] and polymethyl methacrylate (PMMA)[21] are widely used for their biodegradability, biocompatibility, and ability to retard water penetration, thereby prolonging drug release. These materials are particularly valuable for the formulation of microspheres intended for long-term therapeutic use.

In addition to polymers, cyclodextrins (CDs) – a class of cyclic oligosaccharides composed of α-(1,4)-linked glucopyranose units – have been extensively studied for their ability to form inclusion complexes with poorly water-soluble drugs, thereby enhancing their aqueous solubility, dissolution rate and absorption profile.[3,21,22,27] CDs possess a hydrophobic inner cavity and an ideal hydrophilic outer surface, making them candidates for complexation-based drug delivery.[27,28] The incorporation of drug-CD complexes into solid oral dosage forms, such as tablets or capsules, can further enhance bioavailability and enable the development of controlled delivery systems, especially when used in conjunction with appropriate matrix-forming agents.

Among the various encapsulation techniques, the emulsion-solvent evaporation method has been widely used in pharmaceutical development to produce polymer-based microspheres. This technique typically involves dissolving both the drug and the polymer in a volatile organic solvent, followed by emulsification into an aqueous phase and subsequent evaporation of the solvent.[6,8] The resulting microspheres are able to encapsulate the drug in a stable matrix, providing controlled and sustained release over an extended period of time. This method is particularly suitable for poorly water-soluble drugs, where oil-in-water (O/W) emulsions and water-insoluble polymers are commonly used. The process is relatively simple, inexpensive and does not require sophisticated equipment, making it an attractive option for pharmaceutical manufacturing.

However, the use of organic solvents raises potential safety and environmental concerns. To overcome these limitations, alternative encapsulation techniques, such as the emulsion/ congealing, have been explored. This technique is based on the melting of lipophilic materials (e.g. natural waxes or fats) in which the active pharmaceutical ingredient (API) is either dissolved or dispersed. The melted mixture is emulsified in an aqueous phase and then cooled to form solid microparticles.[12–15] This solvent-free process is environmentally friendly, cost effective, suitable for thermolabile compounds and offers a simple and scalable process with good reproducibility.

Solid lipid microparticles (SLMPs), based on natural or synthetic waxes, represent another class of lipid-based drug delivery systems that have shown promise for sustained release and protection of sensitive drugs from chemical degradation. These systems are increasingly being used as excipients due to their biocompatibility, low toxicity and ability to provide controlled drug release profiles. Beeswax, a natural lipid with a long history of pharmaceutical and cosmetic use, is particularly attractive due to its generally recognized as safe (GRAS) status, low cost and availability from renewable sources.[29]

Despite the considerable potential of multiparticulate drug delivery systems, particularly those utilizing lipid or polymer-based encapsulation techniques,

limited comparative studies have been conducted to evaluate their respective efficacy in modulating the release of poorly water-soluble drugs such as ketoprofen.[10]

In this study, we investigated and compared two different microencapsulation techniques for the formulation of ketoprofen-containing controlled-release microparticles:

1. The emulsion-congealing technique using beeswax from the Tessala region of Sidi Bel Abbes (Algeria) as the primary lipid matrix.
2. The emulsion-solvent evaporation technique using cellulose acetate butyrate (CAB) as the main encapsulating polymer.

To modulate the drug release profiles and improve the physicochemical properties of the microparticles, various hydrophobic and hydrophilic excipients, including, PCL, PMMA, HPMC and *β*-cyclodextrin (β-CD), were incorporated in the matrix formulations at different ratios. The study aims to evaluate the effect of encapsulation technique and matrix composition on the morphology, particle size, drug entrapment efficiency and *in vitro* drug release kinetics of the prepared microspheres. This work contributes to the growing field of advanced oral drug delivery systems by providing insight into the comparative performance of polymeric and lipid-based microspheres for the sustained release of poorly water-soluble drugs.

EXPERIMENTAL

Chemicals

Ketoprofen (MW: 254.29) was obtained from APM Company (Sult, Jordan). Cellulose acetate butyrate, with a viscosity of 0.1 Pa·s in a 5 mass % solution prepared in a toluene/ethanol mixture (4:1 volume ratio), was supplied by Merck (India). Beeswax was kindly provided as a gift sample by Tessala, SBA (Algeria). Tween 80, hydroxypropylmethylcellulose (HPMC), *β*-cyclodextrin (*β*-CD), and polycaprolactone (PCL, *Mw*: 70,000–90,000) were all purchased from Sigma–Aldrich. Dichloromethane (DCM, >98 % purity) was used as the organic internal phase. A simulated gastric fluid (pH 1.2) was prepared by dissolving 2 g of NaCl and 60 mL of hydrochloric acid solution (1 M) in 1 L of deionized water. The phosphate buffer solution at pH 7.4 was prepared by mixing 250 mL of potassium dihydrogen phosphate solution (KH_2PO_4, 0.2 M) with 195.5 mL of sodium hydroxide solution (NaOH, 0.1 M), and adjusting the final volume to 1 L with deionized water.

Materials and equipment

Infrared (IR) spectra were recorded using a Bruker Alpha FT-IR spectrometer equipped with a platinum ATR single-reflection diamond module. X-ray diffraction (XRD) patterns of the pure drug, polymeric carriers and microsphere formulations were obtained using a Rigaku MiniFlex 600 diffractometer (MiniFlex acquisition system, λ = 1.541 Å) over a 2θ range of 5 to 70° and analyzed for comparative purposes. The carbon-13 nuclear magnetic resonance (^{13}C--NMR) spectra of the polymers were recorded on a Bruker spectrometer operating at 300 MHz.

Viscometric measurements were conducted using a Cannon-Fenske KPG-type capillary viscometer, with the temperature maintained at 25±0.1 °C using a thermostatic water bath. The average molar mass (M_V) of the PMMA fractions was determined *via* intrinsic viscosity measurements using the Mark–Houwink equation.

The mean particle diameter and size distribution of the microspheres were calculated based on optical microscopy observations (Optika 4083.B1) by counting over 500 individual microparticles at the appropriate magnification. The number average diameter (d_{10}), the average surface diameter (d_{32}), the weight average diameter (d_{43}) and the particle size distribution (δ) were calculated from the expressions given below:

$$d_{10} = \frac{\sum n_i d_i}{\sum n_i} \tag{1}$$

$$d_{32} = \frac{\sum n_i d_i^3}{\sum n_i d_i^2} \tag{2}$$

$$d_{43} = \frac{\sum n_i d_i^4}{\sum n_i d_i^3} \tag{3}$$

$$\delta = \frac{d_{43}}{d_{10}} \tag{4}$$

The morphology of the ketoprofen-loaded microspheres was examined further, using scanning electron microscopy (SEM) with a Hitachi TM 1000 microscope.

Ketoprofen release kinetics were monitored using a double-beam UV–Vis spectrophotometer (Shimadzu UV-2401) equipped with thermostated cells in a simulated gastric medium (pH 1.2), which was maintained at 37±0.1 °C.

Synthesis and characterization of polymethylmethacrylate (PMMA)

Polymethylmethacrylate (PMMA) was obtained by a radical polymerization, under nitrogen atmosphere, in anhydrous tetrahydrofuran (THF) as solvent, at 90 °C, and in the presence of initiator: 0.5 % of benzoyl peroxide during 4 h.

In two glass polymerization tubes, five grammes of monomer (MMA), 0.5 mass % of benzoyl peroxide and 3 ml of THF are introduced into each tube. After degassing with nitrogen, the polymerization tube is immersed in a bath of oil set at 90 °C.

Polymers are generally mixtures of homologs that differ in molecular weights. Fractionation is a means of separating the different molecular weights of the polymer. The poly-molecularity index is a quantity that provides information on the heterogeneity of the macromolecule.

In our case, the fractionation process involves adding the polymer solution to a non-solvent (precipitating agent) to precipitate the polymer.[30] This method is based on the principle that longer polymer chains precipitate first, followed by progressively shorter chains. A total of eight fractions (F1–F8) were obtained.

Experimental fractionation protocol

The polymer was solubilized in 20 ml of chloroform and then poured into a beaker. A volume of heptane was poured into a burette and added progressively (drop by drop) to the solution under continuous stirring until the appearance of a turbidity. After a few hours of ripening, the haze is dissolved by varying the temperature. The solution is left to stand for several hours.

The concentrated phase is separated by decantation; then dissolved in a small amount of solvent and finally isolated by pouring the solution into pure precipitant (the volume of precipitant is 3 times that of the solution). The solid obtained after vacuum filtration is oven-dried at 40 °C until the weight is constant. The volume of supernatant (reduced by evaporation) is treated again with an additional amount of precipitant to obtain a new fraction. This process is

repeated until a large quantity of precipitant has no effect. The final solution was then concentrated under reduced pressure, the precipitant poured off and the last fraction isolated. Note that the first fraction was further fractionated to give 2 further fractions PMMA (F1, 1) and PMMA (F1, 2). After drying all the fractions. A yield of 92 % was obtained. The aim of our study is to investigate the effect of molecular weight on the release of ketoprofen by focusing on fractions F1.1, F3 and F4.

The eight fractions of white aspects were characterized: IR, $\bar{\nu}$ (cm^{-1}): 1735.73: C=O (ester); 1041.72: C–O (ester); 2953: –C–H, stretch; 1452,.75: $–CH_3$(bending). ^{1}H-NMR (300MHz): OCH_3, 3.58 ppm; $–CH_2$, 2.143 ppm; $–CH_3$: 1.224 ppm. ^{13}C-NMR (300MHz, $CDCl_3$), δ (ppm): 178 (C=O); O–CH_3 (52); 46 (C: tertiary carbon); 31 (–CH_2–); 17 (C–CH_3). $M_{V(F1)}$ =52177 g/mol, $M_{V(F1,1)}$= 59319 g/mol, $M_{V(F1,2)}$ =43677 g/mol), $M_{V(F2)}$ = 42788 g/mol, $M_{V(F3)}$ =36323 g/mol, $M_{V(F4)}$ =15434 g/mol, $M_{V(F5)}$ =10894 g/mol, $M_{V(F6)}$ =8721 g/mol, $M_{V(F7)}$ =715 g/mol,

Preparation of microparticles

Encapsulation using the emulsion/congealing technique is carried out according to the following procedure.

First, dissolve 0.75 g of Tween® 80 in 150 mL of distilled water, stirring vigorously and heating to 90 °C. This temperature is kept constant.

In a second step, depending on the formulation, an appropriate amount of beeswax or a mixture of beeswax (C.A.) with PMMA at different fractions (F1, F2 and F3), β-CD and HPMC were used. These polymers were added as additives to control the release of ketoprofen.

The mixture is melted in a water bath. The appropriate amount of Ket is added to the molten mixture. The composition of various formulations is given in Table I.

TABLE I. Experimental conditions for microspheres formulations prepared by emulsion-congealing technique; stirring speed: 800 rpm; number of blades: 4

Lot	Composition (drug:matrix), %
µP1	Ket:CA (33:67)
µP2	Ket:CA:PMMA (F1) (33:60:07)
µP3	Ket:CA:PMMA (F3) (33:60:07)
µP4	Ket:CA:PMMA (F4) (33:60:07)
µP5	Ket:CA:β-CD:HPMC (25:25:25:25)
µP6	Ket:CA:β-CD (25:50:25)
µP7	Ket:CA:HPMC (25:50:25)

Finally, the molten mixture was poured into the hot aqueous solution containing Tween® 80 under precisely regulated mechanical stirring at 800 rpm. Agitation was maintained until the emulsion had cooled to room temperature for 20 min. The solid-state micropellets obtained were vacuum-filtered and washed three times with distilled water, then dried at room temperature.

Microspheres produced by the emulsion/solvent evaporation process are prepared according to the following procedure:

One or more polymers (depending on the formulation) and an appropriate amount of Ket were dissolved in 30 mL of DCM. The resulting organic solution was then poured into 150 g of deionized water containing 0.75 g of Tween® 80, which served as the external aqueous phase.

The resulting O/W emulsion was stirred under mechanical agitation 800 rpm for 3 h at room temperature until the solvent evaporated. The resulting microspheres were collected by

filtration, washed several times with deionized water and dried under vacuum in a desiccator for at least 48 h.

The initial composition of the various microspheres prepared by the two encapsulation processes is summarized in Tables I and II.

TABLE II. Experimental conditions for microspheres formulations prepared by emulsion /solvent evaporation process; stirring speed: 800 rpm; number of blades: 4

Lot	Composition (matrix:drug), %
µS1	Ket:CAB (33:67)
µS2	Ket:CAB:PMMA (F1) (33:60:07)
µS3	Ket:CAB:PMMA (F3) (33:60:07)
µS4	Ket:CAB:PMMA (F4) (33:60:07)
µS5	Ket:CAB:*β*-CD:HPMC (25:25:25:25)
µS6	Ket:CAB:*β*-CD (25:50:25)
µS7	Ket:CAB:HPMC (25:50:25)

Determination of drug loading, encapsulation efficiency and microparticles yield

Two protocols were followed to determine the ketoprofen content in the microparticles prepared by the two methods studied:

Ketoprofen was extracted by weighing 15 mg of micropellets that were prepared using the emulsion/congealing technique with different polymers. This amount was dispersed in 10 ml of phosphate buffer solution (pH 7.4) and stirred for 10 min at 70 °C. After filtration, the solution was analysed using a UV–Vis spectrophotometer at 262 nm (16107 L mol^{-1} cm^{-1}) to determine the Ket content. Each determination was performed in triplicate.

On the other hand, Ket content of the microspheres prepared by the emulsion/solvent evaporation process is determined by the extraction of 10 mg of microspheres dissolved in 10 ml of absolute ethanol under magnetic stirring for 24 h. The solution is examined at 250 nm (2711 L mol^{-1} cm^{-1}) to determine the Ket content. Each determination is carried out in triplicate.

The different equations below make it possible to determine the drug loading (*DL*) and the yield (*Y* in %) of microencapsulation:

$$\text{Ket}_{\text{loaded}} = 100\frac{\text{Ket mass in microparticles}}{\text{Mass of microparticles}} \tag{5}$$

$$\text{Ket}_{\text{EE}} = 100\frac{\text{Ket actual drug load}}{\text{Theoretical drug load}} \tag{6}$$

$$Y = 100\frac{\text{Microparticle recovered (practical mass)}}{\text{Mass of carrier and drug used in the formulation (theoretical mass)}} \tag{7}$$

In vitro *Ket release measurements*

A suitable glass dissolution reactor immersed in a bath regulated at 37±0.5 °C equipped with a filter tube to allow removal of the solution without microparticles was adopted for the *in vitro* dissolution tests of Ket from the formulations obtained by the two microencapsulation processes.

Appropriate amounts of formulations containing 25 mg of ketoprofen were placed in the 1000 ml dissolution reactors, filled with 900 ml of simulated gastric fluid at pH 1.2 at 37 °C and a stirring speed of 500 rpm. Aliquots of the medium of 3 mL were taken periodically at predetermined time intervals, and analyzed by UV spectroscopy at the appropriate wavelength

of the gastric medium: λmax = 264 nm (15130 L mol^{-1} cm^{-1}). The removed volume was replaced with an equal volume of fresh pre-warmed medium (37±0.5 °C). Drug release kinetics for each batch were performed in duplicate and the average readings were used for calculation.

The corresponding drug release profiles were represented by plots of cumulative percent drug release (calculated from the total amount of Ket contained in each formulation) *versus* time.

Two mathematical models recording the Higuchi's and the Korsmeyer–Peppar's equations were developed, to elucidate drug transport processes and predict the resulting drug release kinetics.

RESULTS AND DISCUSSION

Microspheres characterizations

Excipients are essential components of nearly all pharmaceutical dosage forms. The formulation of a stable and effective solid dosage form depends on the selection of appropriate excipients, which are added to facilitate drug administration and protect it from degradation.

In this context, fourteen microparticles were analyzed for their shape, surface morphology, drug entrapment and size (mean diameter). Fourteen formulations loaded with Ket and various polymers were developed using two microencapsulation processes: emulsion-congealing and solvent evaporation. Different proportions of polymer were used under the same experimental conditions, resulting in varying sizes (average diameter) and surface morphologies, as well as different levels of drug entrapment. Table III provides information on the drug loading results (Ket loaded, %), entrapment efficiency, percentage practical yield (%) and size distribution.

TABLE III. Microencapsulation results for the prepared microparticles; *DL* – drug loading, *EE* – entrapment efficiency, *Y* – practical yield

Lot	*DL* / %	*EE* / %	*Y* / %	d_{10} / μm	d_{32} / μm	d_{43} / μm	δ
μP1	19.49	58.40	33.58	324.26	423.85	453.86	1.4
μP2	47.02	96	72.68	327.52	509.68	544.86	1.66
μP3	30.21	84	68.24	402.58	699.11	795.74	1.97
μP4	25.33	81.11	56.76	325.30	436.91	469	1.44
μP5	15.67	47	30	162.11	197.64	213.58	1.36
μP6	27	80	41	227.56	289.74	308.87	1.36
μP7	21.48	64.44	52	141.03	186.92	205.93	1.46
μS1	13.63	27.27	35.02	135.01	164.96	178.82	1.32
μS2	36.22	72.43	48.21	155.94	186.80	200.23	1.28
μS3	19.82	39.65	39.03	138.36	158.1	168.23	1.22
μS4	18.04	36.07	30.42	162.80	180.08	187.51	1.16
μS5	16.43	32.86	31	95.36	102.73	106.62	1.12
μS6	20.00	40.00	43.06	117.20	130.24	137.24	1.12
μS7	17.00	34.00	28.48	99.12	107.13	110.91	1.12

The drug content in all formulations ranged from 15.67 to 47.02 % for micropellets (μP1–μP7) and from 13.63 to 36.22 % for microspheres (μS1–μS7), the

encapsulation efficiency (*EE*) varied from 47 to 96 % for micropellets and from 27.27 to 72.43 % for microspheres, while the practical yield ranged from 30 to 72.68 % for micropellets and 28.48 to 48.21 % for microspheres. The loading efficiency and yield were found to be dependent on the technique of encapsulation and the nature of polymer used in the formulation.

The results clearly show that PMMA matrices combined with *β*-CD achieve a higher encapsulation rate, yield and efficiency than beeswax using the emulsion--congealing technique and then CAB employing the solvent-evaporation method. This improved performance is due to the hydrophobic nature of PMMA, which restricts water from penetrating the molten phase containing the beeswax and active ingredient.[21] This reduces the loss of the drug during microencapsulation. Overall, these findings demonstrate that PMMA is more effective than beeswax or CAB at retaining ketoprofen.

Comparing microparticles μP2, μS2, μP3, μS3, μP4 and μS4, which contain PMMA with different viscometric masses, reveals an increase in loading efficiency (Ket loading percentage), yield and encapsulation efficiency as the viscometric mass of the different fractions increases (F1: 59,319 g/mol; F2: 36,323 g/mol; F3: 15,434 g/mol). This confirms the hypothesis that the hydrophobic nature of PMMA limits the transfer of Ket into the aqueous phase. The high molar mass of the entangled structure of PMMA fraction F1 further reduces the solubility of Ket in water, which explains the higher encapsulation rates observed in μP2 (47.02 %) and μS2 (36.22 %).

On the other hand, it was found that the micropartricles containing CDs with CA or CAB depending on the case μP6 and μS6, presented a high drug content compared with the microparticles containing CA or CAB alone (μP1 and μS1). *β*-CDs are fairly soluble in water; they can form water-soluble complexes with lipophilic guests hiding in the CD cavity improving drug entrapment.[22,31,32]

The low yield observed in the formulation (μP5, μS7, μS5) may be attributed to the water solubility of HPMC and *β*-CD which could result in their transfer to the external phase.[22,33] Furthermore, the reduced yield observed in formulations μS5 and μS7, which contain the CAB polymer and the HPMC–*β*-CD/HPMC co--matrix, may be attributed to the migration of fine microparticles during the filtration process.

Effect of the encapsulation process is notable on the drug loading, encapsulation efficiency and yield. Microencapsulation by the emulsion/ congealing technique gives promising results and presents a drug loading which reaches a value of 47.02 % p.a. for μP2 compared to the solvent evaporation method of microencapsulation.[25]

Solid lipids nano- or microparticles SLNs are considered promising drug carrier systems, particularly with the aim of giving a sustained release profile to active substances.[34]

In fact, common ingredients include solid lipids, surfactants and water. The term lipid is used in a broad sense and includes triglycerides, partial glycerides, fatty acids, steroids and waxes (*e.g.*, beeswax as in our case). They have a better biocompatibility because they're made up of lipids similar to physiological lipids, which reduces toxicity. In addition, SLNs are physicochemically stable and can be easily produced on a large industrial scale, and the raw materials and production costs are relatively low.[35]

Emulsions can be used as precursors for the preparation of solid lipid particles since lipids, which are solid at room temperature, can be heated 5 to 10 °C above its melting point to obtain a liquid lipid. In the first step, the lipophilic drug is dissolved in molten lipids. The lipids are then emulsified with a hot surfactant solution using a high shear homogenization. The resulting hot O/W emulsion is cooled to room temperature, and the droplets solidify in the form of solid lipid particles. The microparticles efficiently entrapped Ket due to the appropriate matrix structures of the lipophilic materials, which allowed for the encapsulation of lipophilic drugs.

Optical microscopic analysis was carried out on various microparticle samples. Observations revealed that microgranules were predominantly irregular in shape, whereas microspheres exhibited a generally spherical morphology with varying sizes. The mean particle diameter was measured, and the number-based, surface-based and volume-based mean diameters were calculated from a data set of 500 individual microparticles. Depending on the formulation, the Sauter mean diameter (d_{32}) ranged from 196.92 to 699.11 μm for micropellets and from 102.73 to 186.80 μm for microspheres. The average polydispersity index (*PDI*) was 1.52 for micropellets and 1.19 for microspheres, indicating a narrower size distribution and greater uniformity for the latter. Under identical processing conditions – including a stirring speed of 800 rpm and the use of Tween as surfactant – the solvent evaporation method produced smaller, more spherical, more homogeneous and less dispersed microspheres. In contrast, the thermal gelation method produced larger micropellets with more irregular shapes and greater batch-to-batch variability.

The surface and morphology of the microparticles were further examined by SEM, representative images of which are shown in Fig. 1. Microspheres prepared by thermal gelation (μP1, μP4) showed irregular shapes with a pronounced tendency to agglomerate (aggregate formation). In contrast, microspheres obtained by solvent evaporation were mostly spherical with rough and highly porous surfaces, indicating that drug release is likely to occur through these channels. In addition, microspheres formulated with CAB/BCD (μS6) were also spherical but had smooth surfaces with a slightly collapsed appearance.

The infrared spectra of the micropellets (μP1–μP7) and microspheres (μS1––μS7) were compared with those of the polymeric matrices and the active ingredient, ketoprofen. As an illustration, Fig. 2 presents the spectra of samples

μP6 and μS6 along with those of their respective matrices. Comparative analysis showed that the microparticles exhibited certain characteristic bands of ketoprofen, albeit with relatively low intensities, which can be attributed to the low drug loading. Moreover, none of the spectra of the formulations showed the appearance of new bands, suggesting the absence of chemical interactions between Ket and the polymeric excipients (CA, CAB and *β*-CD). The comparison between the IR spectra of the starting materials and that of the μP6 and μS6 microparticles (Fig. 2) confirms the presence of the active ingredient in the formulation, as evidenced by the O–H stretching vibration band observed around 2916 cm^{-1} and the C=O stretching vibration of the carboxylic acid group of ketoprofen around 1735.42 cm^{-1}. The simultaneous presence of characteristic bands from both Ket and the polymers, without any additional bands, indicates good compatibility between the components and chemical stability of the active ingredient in the formulations studied.

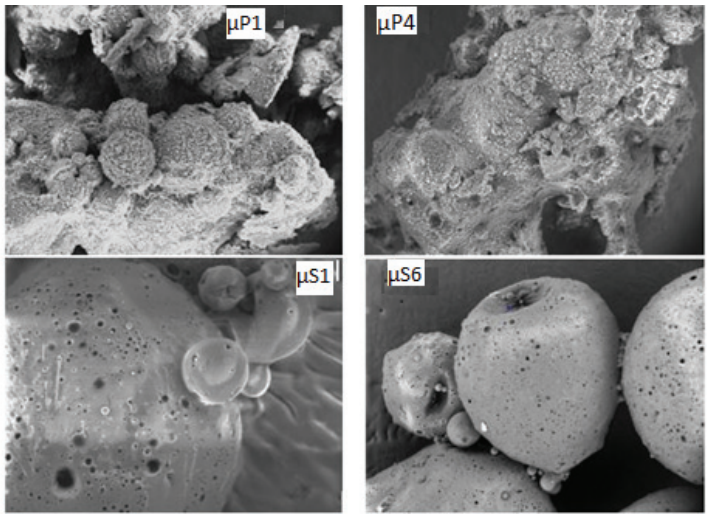

Fig. 1. SEM micrographs of the surface and the morphology of ketoprofen loaded microparticles prepared.

Fig. 3 shows the X-ray diffraction (XRD) patterns of microspheres μP1 and μS2, together with those of the active ingredient ketoprofen and the polymeric matrices CA, CAB and PMMA. It should be noted that ketoprofen and beeswax are semi-crystalline compounds, whereas CAB and PMMA have amorphous structures. Accordingly, the Bragg reflections observed in the μP1 profile can be attributed to the crystalline phases of Ket and CA. In particular, the crystalline peaks of CA are well resolved in μP1, indicating the presence of a highly crystalline material. In contrast, the diffraction pattern of μS2 shows no detectable peaks associated with Ket, suggesting that the drug is present in an amorphous state within the μS2 microspheres.

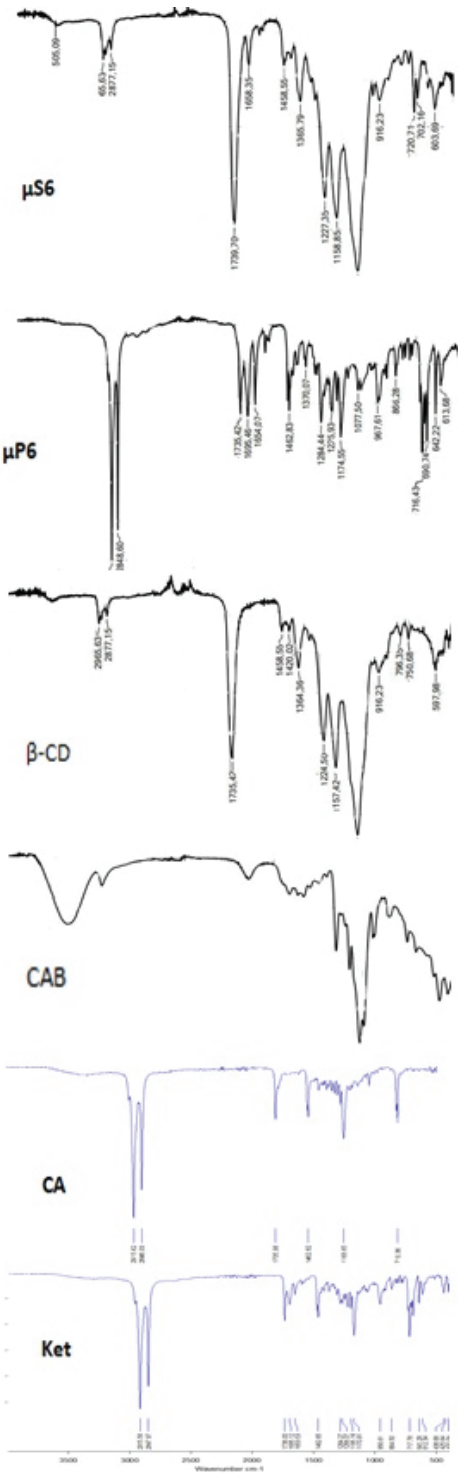

Fig. 2. Infrared spectra of Ket, microparticles (μS6, μP6) and matrices (*β*-CD, CAB, CA).

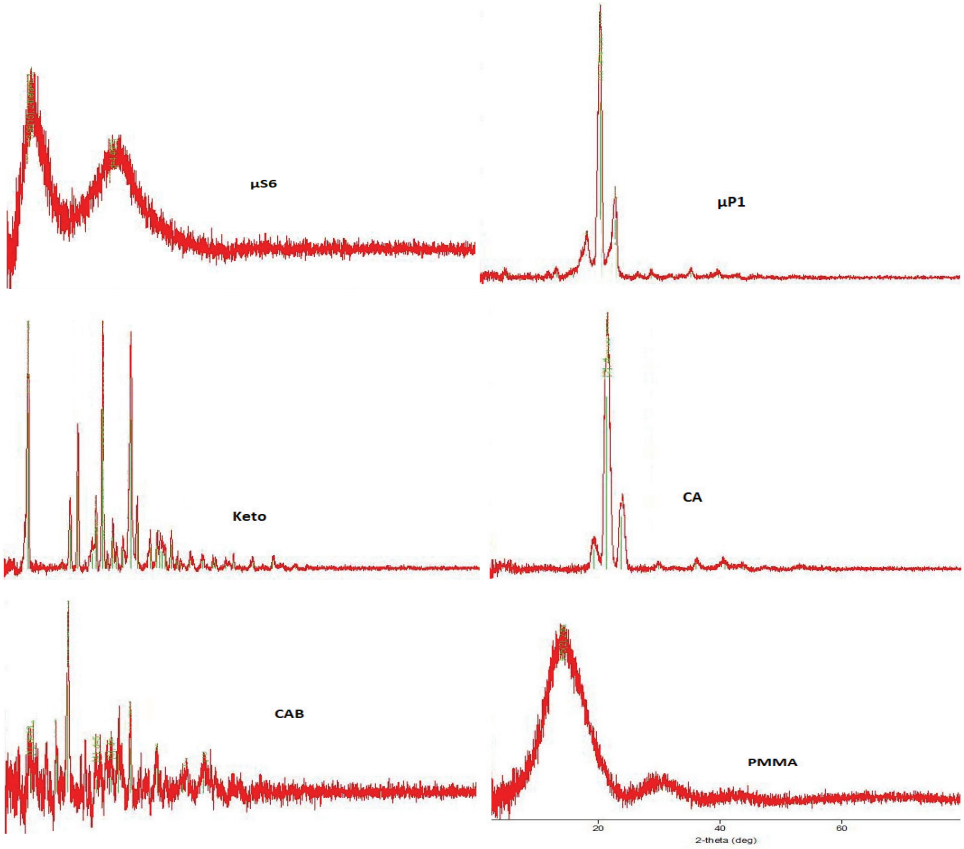

Fig. 3. DRX of Ket, microparticles (µS6, µP1) and matrices (CA, CAB, PMMA).

The nature of surfactant used has been shown to have a significant effect on the transfer of the drug to the external phase, thereby affecting its entrapment efficiency.[36] Surfactants, known for their ability to reduce surface and interfacial tension, are often added to pharmaceutical formulations to improve drug solubility.[37] Surfactants with a hydrophilic–lipophilic balance (HLB) above 15 have been identified as particularly effective solubilising agents.[38] Accordingly, the µp formulations were developed using Tween 80, a hydrophilic surfactant with an HLB of 15, which is ideal for forming stable emulsions with lipid components such as beeswax.[39] In addition, Tween 80 contributed to a significant reduction in microparticle size, as HLB values have a significant effect on droplet size.[40] Similar results were reported by Brahmi *et al.* who also observed the formation of small droplets when using Tween 80.[25] This discussion focuses specifically on the role of Tween 80 in our system, emphasizing its direct impact on emulsion stability and microparticle size, rather than on general surfactant theory.

In vitro *dissolution of Ket from microspheres formulations*

A dissolution study of the active pharmaceutical ingredient was conducted in simulated gastric fluid (pH 1.2). Simultaneously, an *in vitro* drug release evaluation was carried out on various formulations produced by both manufacturing methods, employing beeswax as the primary matrix for micropellets and CAB for microspheres. Hydrophobic and hydrophilic excipients, including, PCL, PMMA (with varying molecular weights), HPMC and *β*-CD), were incorporated in different proportions, depending on the specific formulation. Drug release profiles from the microparticles, assessed after 360 min in the simulated gastric medium, are presented in Fig. 4.

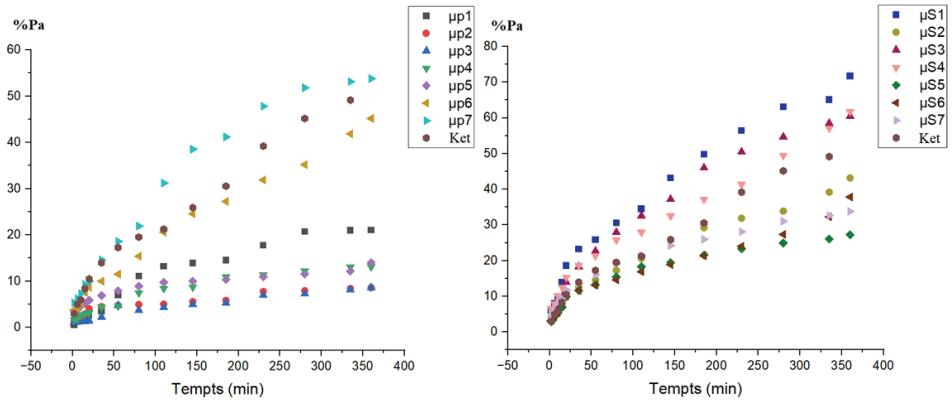

Fig. 4. Drug release profiles from the microparticles, assessed after 360 min in the simulated gastric medium.

The *in vitro* release of ketoprofen from microparticles (µP1-7 and µS1-7) is influenced by several factors, in particular the encapsulation method, matrix type and formulation composition. Table IV shows the evaluation of the Ket release rates from the microparticles after 30, 120 and 360 min. Initially, a comparative study was conducted on four micropellet batches (µP1–µP4) and four microsphere batches (µS1–µS4). The primary matrix used for the micropellets was beeswax (CA), and the primary matrix used for the microspheres was CAB. All formulations included PMMA as a co-matrix with different molecular weights.

The results showed that drug release from beeswax-based micropellets (µP1) was lower, reaching only 8.23 % after 2 h, while CAB-based microspheres showed higher release, with the control batch (µS1) releasing 36 % over the same period. In contrast, PMMA-containing microsphere batches (µP2–µP4, corresponding to F1, F2 and F3) released 5.26, 4.13 and 8.48 %, respectively. Similarly, microspheres containing PMMA showed reduced release: 21.5, 34 and 28.3 % at 2 h.

After 360 min, the cumulative release from microspheres reached 21.04 % for the control (µP1) and 8.59, 8.62 and 13.11 % for µP2 (F1), 3 (F2) and 4 (F3),

respectively. For microspheres, the corresponding values were 71.73 %: μS1, 43.2%: μS2 (F1), 60.6%: μS3 (F2) and 61.8%: μS4 (F3).

TABLE IV. Percentage of Ket released after 30, 120 and 360 min at pH 1.2

Time min	Ket	μP1	μP2	μP3	μP4	μP5	μP6	μP7	μS1	μS2	μS3	μS4	μS5	μS6	μS7
30	13.05	3.13	4.21	1.9	4.1	6.3	9.6	14.2	23	12.3	18	18.2	11	11.2	13.2
12	17.91	8.23	5.26	4.13	8.48	9.8	21.5	33	36	21.5	34	28.3	18.5	17.6	23.3
360	47.16	21.04	8.59	8.62	13.11	14	45.16	53.8	71.73	43.2	60.6	61.8	27.3	37.9	24.24

These results confirm that the presence of PMMA, due to its hydrophobic nature, limits the penetration of the aqueous medium and slows the diffusion of ketoprofen from both micropellets and microspheres. Furthermore, the drug release rate was inversely correlated with the molecular weight of PMMA, as demonstrated by the similar profiles of F1 (M_V = 59319 g/mol) and F2 (M_V = 36323 g/mol) and the comparatively higher release of F3 (M_V = 15434 g/mol).

In addition, the encapsulation method significantly influenced the drug release. Micropellets prepared by thermal gelation showed a more pronounced delayed release behavior, which was attributed to the hydrophobicity of beeswax, which further reduces water permeability and drug diffusion.

The incorporation of hydrophilic excipients such as HPMC and *β*-CD led to a progressive increase in ketoprofen release from micropellets (μP5–μP8), likely due to improved wettability and water penetration in the hydrophobic beeswax matrix. In contrast, microspheres μS5–μS8, also containing HPMC and *β*-CD, showed slightly slower release rates compared to μS1–μS4. This difference may be related to the structural characteristics of the microspheres formed by the solvent evaporation method, where the addition of co-matrices could result in a denser internal structure or reduced porosity, thus slowing the diffusion of the drug.

These observations align with previous results on comparable polymeric matrices and microencapsulation processes, including studies from our laboratory and other research groups that have worked with beeswax-, PMMA- and CAB-based systems containing various active ingredients.[21–25,27] This comparison further highlights the relevance and consistency of our findings.

Release mechanisms and mathematical analysis

Two mathematical models, Higuchi and Korsmeyer–Peppas, were used to describe the release of the drug from polymeric matrices. Each batch was analyzed using the appropriate equations to determine the most appropriate model.
Higuchi:

$$Q_t = K_H\sqrt{t} \tag{8}$$

Korsmeyer–Peppas:

$$\frac{M_t}{M_\infty} K_K t^n \quad (9)$$

The results, presented in Table V, show that both models fit the experimental data well, with correlation coefficients greater than 0.95. This suggests that the drug release is primarily controlled by a diffusion-controlled mechanism.

TABLE V. Coefficients of correlation and dissolution rate constants of HCTZ from microspheres in simulated gastric fluid (pH 1.2)

Lot no.	Higuchi		Korsmeyer–Peppas		
	r^2	K_H	r^2	ln K_K	n
Lot 1	0.954	1.285	0.965	–4.081	0.705
Lot 2	0.943	0.374	0.956	–2.413	0.324
Lot 3	0.975	0.435	0.964	–3.119	0.461
Lot 4	0.972	0.759	0.972	–2.671	0.461
Lot 5	0.966	0.530	0.979	–3.628	0.266
Lot 6	0.98	2.317	0.967	–4.006	0.517
Lot 7	0.985	3.103	0.971	–3.665	0.519
Lot 8	0.993	3.694	0.989	–3.306	0.497
Lot 9	0.99	2.131	0.985	–3.706	0.467
Lot 10	0.996	3.371	0.991	–3.798	0.568
Lot 11	0.978	2.934	0.982	–3.230	0.438
Lot 12	0.982	1.372	0.986	–3.817	0.437
Lot 13	0.964	1.698	0.979	–3.843	0.455
Lot 14	0.993	1.638	0.995	–3.355	0.385

The values of the diffusion exponent n, close to 0.5 for formulations containing PMMA, HPMC and β-CD, indicate Fickian diffusion. For µP5 and µS7 batches, lower values of n correspond to quasi-Fickian diffusion, while the value of n = 0.705 for µP1 suggests an anomalous transport mechanism combining diffusion and matrix erosion.

Moreover, the nature of the matrix significantly affects the release behavior: the incorporation of PMMA significantly slows down the drug dissolution. These results confirm that *in vitro* drug release is influenced by the matrix composition, its molecular weight and the encapsulation method used.

CONCLUSION

The *in vitro* release of ketoprofen from microparticles is determined by a combination of formulation factors and manufacturing methods. Micropellets prepared by thermal gelation using beeswax as the primary matrix exhibited slower release profiles, especially when combined with hydrophobic excipients such as PMMA. The release rate further decreased with increasing molecular weight of PMMA, suggesting reduced matrix permeability. In contrast, the addition of hydrophilic excipients such as HPMC and β-cyclodextrin enhanced drug release from

micropellets by facilitating water penetration and drug solubilization. However, in microspheres prepared by solvent evaporation using CAB, the same hydrophilic co-matrices resulted in a slight decrease in release rates compared to formulations without co-matrices. This may be due to denser or less porous structures formed during the solvent removal process. Overall, the results highlight that both the type of co-matrix and the encapsulation method have a significant impact on drug release behavior, with the solvent evaporation process generally producing more porous and faster releasing microspheres compared to the thermal gelation method. Based on these observations, the most promising system for achieving prolonged and controlled ketoprofen release is beeswax-based micropellets combined with high-molecular-weight PMMA.

Acknowledgements. The authors would like to thank the General Directorate of Scientific Research and Technological Development (DGRSDT) and the Ministry of Higher Education and Scientific Research (MESRS) of Algeria for their invaluable support during the research.

ИЗВОД

КОМПАРАТИВНА СТУДИЈА МИКРОЧЕСТИЦА ИСПУЊЕНИХ КЕТОПРОФЕНОМ ПРИПРЕМЉЕНИХ ТЕХНИКАМА ЗГУШЊАВАЊА И ИСПАРАВАЊА РАСТВАРАЧА ЕМУЛЗИЈЕ

HADJER SEBAIHI[1], WASSILA BENSALAH[2], KARIMA BADIS[1] и MERINE HAOUARIA[1]

[1]*Laboratory of Macromolecular Physical and Organic Chemistry, Faculty of Exact Sciences, University of Djillali Liabes, Sidi Bel-Abbes, Algeria и* [2]*Laboratory for the Application of Organic Electrolytes and Polyelectrolytes (LAEPO), University of Tlemcen, B.P. 119, 13000 Tlemcen, Algeria*

Кетопрофен (Кет) је често коришћени нестероидни антиинфламаторни лек (NSAID) са аналгетским и антиинфламаторним својствима. Међутим, његова слаба растворљивост у води и кратак биолошки полуживот ограничавају његову терапијску ефикасност и могућност примене од стране пацијента. Микрочестице са контролисаним ослобађањем омогућавају стратегију за продужење ослобађања лекова и побољшање биорасположивости. У овој студији припремљене су микрочестице испуњене кетопрофеном користећи две технике микрокапсулације: емулзију-згушњавање пчелињим воском и испаравање растварача са целулозним ацетат-бутиратом (CAB). Затим су прилагођене ко-матрице које садрже хидрофобне компоненте (PMMA и PCL) и хидрофилне компоненте (HPMC и β-циклодекстрин) за модулацију ослобађања лека. Микрочестице на бази пчелињег воска, посебно у комбинацији са PMMA, показале су спорије ослобађање због смањене пропустљивости матрице. Укључивање хидрофилних помоћних материја у микрочестице на бази пчелињег воска убрзало је ослобађање Кет и подстакло продирања воде и солубилизације лекова. Насупрот томе, укључивање хидрофилних помоћних материја у микросфере на бази CAB незнатно је смањило ослобађање лека, вероватно зато што је гушћа структура матрице формирана током испаравања растварача. Ови резултати показују да метода енкапсулације и састав матрице критично утичу на кинетику ослобађања Кет, пружајући смернице за рационални дизајн система за испоруку лекова са контролисаним ослобађањем.

(Примљено 7. септембра, ревидирано 10. новембра, прихваћено 18. децембра 2025)

REFERENCES

1. F. Jamali, D. Brocks, *Clin. Pharmacokinet.* **19** *(*1990) 197 (https://doi.org/10.2165/00003088-199019030-00004)
2. D. Wolff, G. Christophersen, C. Brown, S. M. Mulcahey, M. K. Mulcahey, *The Phys. Sportsmed.* **49** (2021) 381 (https://doi.org/10.1080/00913847.2021.1886573)
3. R. Rajamohan, E.Kamaraj, P. Muthuraja, K. Murugavel, C. Govindasamy, D. S. Prabakaran, T. Malik, Y. R. Lee, *Sci. Rep.* **14** *(*2024) 21516 (https://doi.org/10.1038/s41598-024-71615-9)
4. A. K. Arifah, M. F. Landoni, S. P. Frean, P. Lees, *Am. J. Vet. Res.* **62** *(*2001) 77 (http://dx.doi.org/10.2460/ajvr.2001.62.77)
5. S. Bindu, S. Mazumder, U. Bandyopadhyay, *Biochem. Pharmacol.* **180** (2020) 114147 (https://doi.org/10.1016/j.bcp.2020.114147)
6. K. Sanka, P. R. Veerareddy, R. R. Pragada, *J. Hol. Integ. Pharm.* **6** (2025) 83 (https://doi.org/10.1016/j.jhip.2025.03.001)
7. P. R. Sune, K. S. Jumde, P. R. Hatwar, R. L. Bakal, A. V. Korde, *GSC Biol. Pharm. Sci*. **29** (2024) 286 (https://doi.org/10.30574/gscbps.2024.29.3.0475)
8. T. K.Giri, C.Choudhary, Ajazuddin, A. Alexander, H. Badwaik, D. K. Tripathi, *Saudi Pharm. J.* **21** (2013) 125 (http://dx.doi.org/10.1016/j.jsps.2012.05.009)
9. W. Elballa, M. Salih, A. E. Elawni, *J. Phar. Res. Int.* **36** (2024) 78 (https://doi.org/10.9734/jpri/2024/v36i127630)
10. F. Maestrelli, N. Zerrouk, M. Cirri, P. Mura, *Int. J. Pharm.* **485** (2015) 365 (https://doi.org/10.1016/j.ijpharm.2015.02.073)
11. R. Bodmeier, H. Chen, *J. Contr. Rel.* **10** (1989) 167 (https://doi.org/10.1016/0168-3659(89)90059-X)
12. G. J. Vergote, C. Vervaet, I. V. Driessche, S. Hoste, S. De Smedt, J. Demeester, R. A. Jain, S. Ruddy, J. P. Remon, *Int. J. Pharm.* **219** (2001) 81 (https://doi.org/10.1016/S0378-5173(01)00628-7)
13. V. Nahum, A. J. Domb, *Int J. Pharm.* **621** (2022) 121797 (https://doi.org/10.1016/j.ijpharm.2022.121797)
14. L. Y. Ho, Z. S. Xiang, R. Gopal, S. A. Khan, *Int J. Pharm.* **596** (2021) 120230 (https://doi.org/10.1016/j.ijpharm.2021.120230)
15. M. Üner, U. Gönüllü, G. Yener, T. Altınkurt, *Farmaco* **60** (2005) 27 (https://doi.org/10.1016/j.farmac.2004.08.008)
16. M. Ricci, P. Blasi, S. Giovagnoli, C. Rossi, G. Macchiarulo, G. Luca, G. Basta, R. Calafiore, *J. Contr. Rel.* **107** (2005) 395 (https://doi.org/10.1016/j.jconrel.2005.06.023)
17. S. Kangishwar, N. Radhika, A. A. Sheik, A. Chavali, S. Hariharan, *Polym. Bull.* **80** (2023) 47 (https://doi.org/10.1007/s00289-022-04087-4)
18. F. Ö. Gökmen, N. P. Bayramgil, *Carbohydrate Polymers*. **297** (2022) 120030 (https://doi.org/10.1016/j.carbpol.2022.120030)
19. B. Gupta, V. Mishra, S. Gharat, M. Momin, A. Omri, *Pharmaceuticals (Basel)* **14** (2021) 1201 (https://doi.org/10.3390/ph14111201)
20. T. Yamada, H. Onishi, Y. Machida, *J. Contr. Rel.* **75** (2001) 271 (https://doi.org/10.1016/S0168-3659(01)00399-6).
21. O. C. Larbi, H. Merine, Y. Ramli, F. B. Toumi, K. Guemra, A. Dehbi, *J. Serb. Chem. Soc.* **83** *(*2018) 1243 (https://doi.org/10.2298/JSC171112065LA)

22. K. Badis, H. Merine, Y. Ramli, O. C. Larbi, C. H. Memou, *J. Mex. Chem. Soc.* **66** (2022) 17 (https://doi.org/10.29356/jmcs.v66i1.1583)
23. M. Mouffok, A. Mesli, I. Abdelmalek, E. Gontier, *J. Serb. Chem. Soc.* **81** (2016) 1183 (https://doi.org/10.2298/JSC160308068M)
24. A. Merdoud, M. Mouffok, A. Mesli, N. Chafi, M. Chaib, *J. Serb. Chem. Soc.* **85** (2020) 531 (https://doi.org/10.2298/JSC190326132M)
25. R. Brahmi, K. Diaf, Z. ELBahri, M. Baitiche, *J. Serb. Chem. Soc.* **89** (2024) 91 (https://doi.org/10.2298/JSC230501088B)
26. D. J. Hines, D. L. Kaplan, *Crit. Rev. Ther. Drug Carrier Syst*. **30** (2013) 257 (https://doi.org/10.1615/critrevtherdrugcarriersyst.2013006475)
27. O. Khoukhi, Z. El Bahri, K. Diaf, M. Baitiche, *Chem. Pap.* **70** *(*2016) 0014 (https://doi.org/10.1515/chempap-2016-0014).
28. E. Obaid, A. K. M. Jamil, S. Prabu, S. M. Saharin, S. Mohamad, *Spectrochim. Acta, A* **241** (2020) 118674 (https://doi.org/10.1016/j.saa.2020.118674).
29. G. Gupta, K. Anjali, *IOP Conf. Ser.: Earth Environ. Sci.* **1110** (2023) 012041 (https://doi.org/10.1088/1755-1315/1110/1/012041)
30. G. Champetier, L. Monnerie, *Introduction à la Chimie Macromoléculaire,* Hermann, Paris, 1975
31. J. Szejtli, *Cyclodextrin Technology*, Kluwer Academic Publishers, Dordrecht, 1988, pp. 1–78
32. V. J. Stella, M. R. Venkatramana, E. A. Zannou, V. Zia, *Adv. Drug Deliv. Rev*. **36** (1999) 3 (https://doi.org/10.1016/S0169-409X(98)00052-0)
33. G. Poovi, S. Rajpriyadarsini, S. Uma, R. Vinothini, *Asian J. Pharm. Sci.* **10** (2015) 433 (https://doi.org/10.1016/j.ajps.2015.05.001)
34. L. Battaglia, M. Gallarate, P. P. Panciani, E. Ugazio, S. Sapino, E. Peira, D. Chirio, in *Application of Nanotechnology in Drug Delivery*, A. D. Sezer, Ed., InTechOpen LTD, London, 2014 (http://dx.doi.org/10.5772/58405)
35. R. H. Müller, K. Mader, S. Gohla, *Eur. J. Pharm. Biopharm*. **50** (2000) 161 (https://doi.org/10.1016/S0939-6411(00)00087-4)
36. R. Dinarvand, S. H. Moghadam, A. Sheikhi, F. Atyabi, *J. Microencapsul.* **22** *(*2005) 139 (https://doi.org/10.1080/02652040400026392)
37. A. Müllertz, A. Ogbonna, S. Ren, T. Rades, *J. Pharm. Pharmacol.* **62** (2010) 1622 (http://dx.doi.org/10.1111/j.2042-7158.2010.01107.x)
38. R. B. Pedada, E. Vanka, A. M. S. Sudhakar Babu, P. K. Desu, P. R. Bharathi, P. V. Rao, *PharmaTutor* **1** (2013) 60 (http://www.pharmatutor.org/pdf_download/pdf/1(2)-enhancement-of-solubility-an-over-view.pdf)
39. A. K. Hassan, *Indian J. Pharm. Sci.* **80** (2018) 334 (https://doi.org/10.36468/pharmaceutical-sciences.561)
40. E. Kim, W. G. Cho, *J. Korean Appl. Sci. Technol.* **31** (2014) 203 (http://dx.doi.org/10.12925/jkocs.2014.31.2.203).

Journal of the Serbian Chemical Society
JSCS-info@shd.org.rs • www.shd.org.rs/JSCS
J. Serb. Chem. Soc. *91* (2) 181–193 (2026)
JSCS–5485
Original scientific paper
Published 12 February, 2026

Exploring the distinct physico-mechanical characteristics of bio-polymer based chambray fabric

NASRIN AKTER[1], MD. REAZUDDIN REPON[2], ARNOB D. PRANTA[3,4]*, MD. RUHUL AMIN[1], NURZOD YUNUSOV[5] and SALIM M. OTAJONOV[5]

[1]Department of Textile Engineering, Ahsanullah University of Science and Technology, Tejgaon I/A, Dhaka-1208, Bangladesh, [2]Department of Bioproducts and Biosystems, School of Chemical Engineering, Aalto University, Vuorimiehentie 1, 02150 Espoo, Finland, [3]ZR Research Institute for Advanced Materials", Sherpur-2100, Bangladesh, [4]Department of Textile Engineering, Mawlana Bhashani Science and Technology University, Santosh, Tangail, 1902, Bangladesh and [5]Department of Technological Education, Fergana State University, Fergana 150100, Uzbekistan

(Received 18 June, revised 7 July, accepted 3 October 2025)

Abstract: Denim is known for its strength and longevity whereas chambray is softer, more comfortable and often used for trendy garments. This research work compares the physical and mechanical properties of bio-polymer based organic cotton (100 %) denim and organic cotton (100 %) chambray fabric. While the both fabrics had identical warp and weft counts, denim had a higher ends per inch (*EPI*) and picks per inch (*PPI*) despite having a comparable construction. Denim has a higher (5.65 %) grams per square meter (*GSM*) than chambray which in turn allows for greater dye absorption. While chambray had a lower tensile and bursting strength than bio-polymer based 100 % cotton denim in the warp direction, the weft direction showed the reverse. Additionally, denim performed much better in the tear strength test (6.29 %). Chambray fabric, on the other hand exhibited less pilling behaviour. The abrasion resistance test yielded excellent results for chambray fabric. The results show that denim is stronger, more compact and more durable, making it better suited for tough conditions. In contrast, chambray offers a softer feel, better breathability and greater comfort in summer, along with a distinct look for coloration.

Keywords: tensile strength; fabric construction; abrasion resistance; comfort performance; organic cotton; pilling behaviour.

* Corresponding author E-mail: arnobdhar75@gmail.com
https://doi.org/10.2298/JSC250618076A

INTRODUCTION

Modern consumers' demand for absolute bio-polymer based comfortable apparel in today's cutting-edge is growing simultaneously. Contemporary consumers seek not only trendy design but also opt for comfort apparel for everyday use.[1,2] The cozy embrace of fabric is like slipping into a cocoon. Its softness and cooling effect provide relief in regular daily life use.[3] Bio-polymer based materials like cotton have been the prime choice for users from the beginning of modern civilization.[4] Hence, there is a wide range of cotton fabrics available in the market. However, these fabrics vary from one to another according to manufacturing techniques, construction and designs. Additionally, manufacturers along with buyers are in a race to introduce new fabrics designs and construction to provide additional functions to consumers so that they can solve the real life challenges as per consumers demand for bio-polymer based materials.[5]

Since chambray evolved from cambric, its origins can be traced back to the mid-1500s. Cambric, originally fashioned from linen which is an airy plain weave fabric. Cambrai, a northern French region that was formerly part of Flanders where the cloth was first manufactured.[6] Shirting, handkerchiefs, and elaborate needlework and lace were common uses for cambric, a high-quality fabric. On the other hand, Denim is a fabric that is comfortable, fashionable, affordable and durable which make it ideal for many garments and accessories. A lighter cotton twill fabric, denim is recognizable by its diagonal weave or texture and traditionally dyed indigo blue.[7] Chambray, a 100 % cotton plain-weave soft fabric with diagonal ridges has a white weft and a light blue warp. Chambray, with its blue warp and white weft, is often mistaken for denim. Though similar to denim, chambray is lighter and woven differently. The fabric is thinner and softer than denim.[8]

Numerous knitted fabrics have been the subject of substantial investigation in bio-polymer based textile research, with a focus on qualities, uses and performance indicators.[9–11] The investigation of chambray fabric is severely understudied. Research on knitted fabrics has been extensive but chambray has been largely disregarded in favor of denim, cellulosic fibers and polyester. More research into the unique properties, performance features, and possible uses of chambray fabric deserves consideration due to this void in the existing literature.

The research work explores the physical traits of bio-polymer based chambray fabric compared to denim fabric with different areas maintaining the same construction parameters such as ends per inch (*EPI*), picks per inch (*PPI*), tear strength, bursting strength, abrasion resistance, pilling nature and fastness properties. The research attempts to offer a thorough comprehension of bio-polymeric chambray fabric and its possible uses in various domains such as design, textiles, and fashion. The purpose of this research work is to fill a knowledge vacuum in textile science and add to the existing body of knowledge. The findings should then inform fabric design, industry applications, and future research.

EXPERIMENTAL

Materials

100 % cotton yarns are used as bio-polymer to prepare chambray fabric of 1/1 plain structure and denim fabric of 3/1 twill structure for the present study. Both chambray and denim fabric's warp yarns were Indigo dyed and the weft yarns were kept undyed. both warp and weft yarns were sourced from Simtex Industries PLC. *EPI* and *PPI* of grey denim fabric are 98 and 50, respectively. The warp count and weft count of grey denim fabric are 32/2 Ne and 21/2 Ne individually. The same specifications are maintained for chambray fabric.

Experimental apparatus

Air jet loom (Picanol Omni plus 800, China) and rapier loom (Picanol OptiMax-I, China) were used for weaving chambray and denim fabric respectively. Mechanical properties were assessed through a tear tester (Thwing-Albert, West Berlin, NJ, USA), tensile strength tester (James H. Heal, Halifax, UK), bursting strength tester (James H. Heal) and abrasion and pilling tester (M235, UK).

Determination of EPI *and* PPI

Counting glasses were used to inspect samples. A square-shaped part of the counting glass helped count yarns per inch. This measurement was essential for analyzing woven fabric density and quality. The warp direction of the fabric's lengthwise threads was used to determine *EPI*. The weft direction of the threads flowing widthwise across the fabric was used to calculate *PPI*. These measures illuminated the woven material's structure and properties.

*Determination of grams per square meter (*GSM*)*

The test technique began with 48-h fabric conditioning to guarantee adequate relaxation, following test method BS 2471:1978.[12] Five 100-square-centimeter test specimens were carefully cut from each sample using a *GSM* cutter. Each specimen was weighed carefully on an electric scale and multiplied by 100 to calculate *GSM*.

Determination of tensile strength

Test standard ISO-139342 was adopted to determine the tensile strength.[13] The bio-polymer based manufactured fabric was conditioned for 48 h before testing to ensure relaxation. Next, a 200 by 100-mm cloth sample was properly created. Two fabric ends were secured and fastened into jaws. Using a 100-mm gauge, the upper and lower front jaws were 25 mm by 25 mm and the upper and lower back jaws 25 mm by 50 mm. Using a load cell, the force range was calibrated for the breaking point. The specimen was carefully positioned between the upper and lower jaws and pre-tensioned to straighten the lower end. The fabric ruptured after stretching. This was done five times for warp and weft to ensure thorough testing and analysis.

Determination of tear strength

According to ISO 13937-1, the fabric was conditioned for 48 h to guarantee optimal relaxation before testing. Fabric samples were then cut from the warp and weft directions using a steel plate to precise specifications. Samples measuring 60 mm by 100 mm were taken from the weft and warp directions, respectively. A systematic strategy was used to gather five warp and weft samples for testing. To achieve accurate and consistent results, all parameters were properly set before testing. The fabric was loaded with 3200 g (326.9 N) during the tear test. Two jaws that fit a 20-mm slit secured the fabric. The tear test used a C-type pendulum to break the fabric apart.

Determination of abrasion

Bio polymer based manufactured fabric durability testing was meticulously done according to ISO 12947-3:1999.[14] At first, the fabric was conditioned for 48 h to relax. After that, a sample cutter neatly cut 38-mm samples. To test these samples were placed in golden rings. Pushing down on each specimen's polyurethane foam provided pressure. To ensure accuracy, specimen holders were properly set up in the testing machine and all counters were calibrated to zero before testing. Sample weights were taken at 250, 500, 750, 1000, 1250, 1500 and 2000 cycles during testing. These measurements were crucial for computing each sample's mass loss in %, which provided ISO 12947-3:1999-compliant fabric abrasion resistance and durability statistics.

Assessment of pilling

The bio polymer based manufactured fabric was conditioned for 48 h before testing to ensure relaxation. After cutting the test specimen using a pilling cutter, 140-mm samples were taken. Two samples were prepared for the pilling table and specimen holder. The gadget was wrapped in a rubber specimen holding ring and a 140-mm specimen disk was placed on top, allowing excess material to dangle over the edge. A 90-mm felt was also used. After rolling the rubber ring up the loading block, the specimen holder was removed. Before starting the machine, all counters were checked for zero. The fabric's pilling resistance was assessed using a 5-point scale at 125, 500 and 2000 cycles.

Determination of bursting strength

Test standard ISO 13938-1:1999 approach assessed the fabric's bursting strength.[15] The bio polymer based manufactured fabric was conditioned for 48 h to relax. After that, a one-yard swatch was carefully split into 125-mm test specimens. After that, the specimens were carefully placed between the testing device's top and bottom clamps to avoid wrinkles. Turning the hand wheels clockwise ensured homogeneous specimen compression in the clamps. The fabric was held tightly and pressured until it ruptured at a specific pressure. All pressure and time data from the testing machine were carefully collected.

RESULTS AND DISCUSSION

Impacts of bio-polymer based chambray and denim fabric on EPI *and* PPI

Denim has a higher average *EPI* of 114 than chambray, which is obvious from the appearance which is seen in Fig. 1. Additionally, chambray has a lower average *PPI* of 61 than denim. According to a study, denim fabric features a weft count of 20 Ne and has *PPI* of 50.[16] In the present study, the weft count is 21 Ne, resulting in a higher yarn density per inch due to its finer nature and aligning closely with traditionally utilized denim fabrics. The entire width and total number of warp threads determine the *EPI*. Once the fabric enters the relaxation condition, it begins to compress. The compactness and tear strength of fabrics with a higher *EPI* are superior to those with a lower *EPI*. Fabrics with a lower *EPI* rating also tend to be more comfortable. The lower porosity between the yarns in denim's 3/1 twill weave structure means that there is less space for the yarns to compress after relaxation that leads to a higher *EPI*. Chambray fabric has a lower *EPI* than other fabrics, but it can compress more yarns per inch because of its greater interlacement point and

higher porosity between yarns. Because of its finer weave and increased breathability, chambray fabrics are ideal.

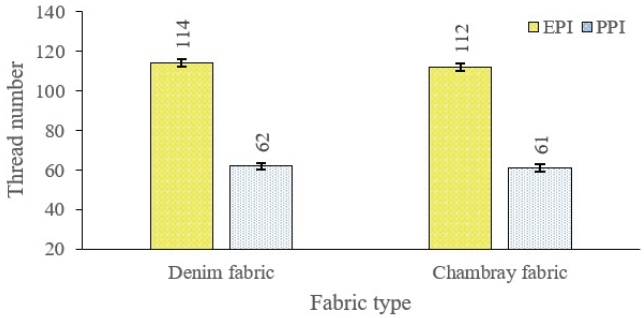

Fig. 1. Impacts of chambray and denim fabric on *EPI* and *PPI*.

Impacts of bio-polymer based chambray and denim fabric on GSM

Compared to 100 % bio-polymeric cotton chambray, 100 % bio-polymeric cotton denim has a higher *GSM* as shown in Fig. 2. *GSM* is a straightforward metric way to measure a fabric's weight. The higher *GSM* of denim fabric is due to the fact that, despite having similar yarn counts to chambray fabric, denim fabric contains two more warp yarns and one more weft yarn per inch. Denim with a higher *GSM* of 163.50 is less breathable than chambray which is 153.75. Studies show that an off-white 3/1 "Z" twill cotton-spandex fabric (97.8 % cotton, 2.2 % spandex) has *GSM* of 345.[17] As a result, chambray can be preferred for light dresses and denim for rough denim.

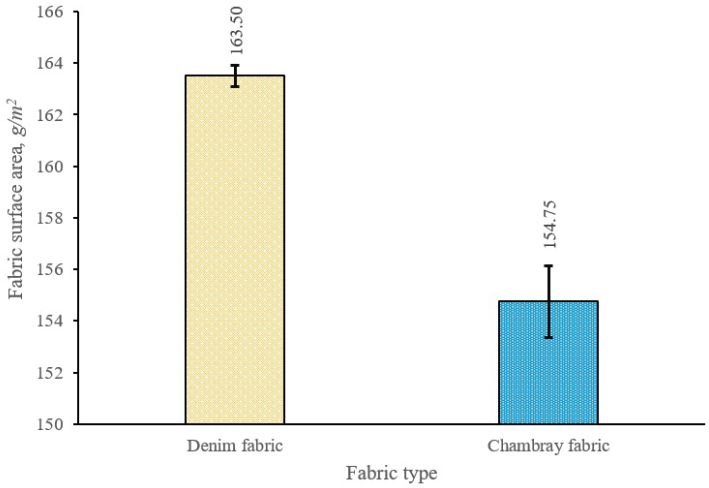

Fig. 2. Analysis of *GSM* of chambray and denim fabrics.

Impacts of bio-polymer based chambray and denim fabric on tensile strength

Denim has a greater tensile strength in the warp direction than bio-polymer based chambray, as shown in Fig. 3a and b. Results were better with twill-structured denim fabric with a mean maximum force of 421.75 N than with chambray fabric with 364.5 N because of the higher ends per inch. Less porosity, a high interlacement point, and a high cross over point are the three factors that contribute to a higher tensile strength. These mentioned factors are higher for plain structured fabric than for denim due to the higher *EPI* in denim. Therefore, denim with a 3/1 twill structure is stronger with an elongation of 18.14 % in the warp direction than chambray about 16.61 %, which has lower tensile strength. Previous study shows that the polyester denim sample exhibited the highest tensile strength (378.06 N in the warp direction, 371.28 N in the weft direction) due to its higher crystallinity, while the cotton denim sample had the lowest (321.03 N in the warp direction, 201.9 N in the weft direction). The CVC denim and PC denim samples showed similar strengths (304.25 N and 317.47 N).[16]

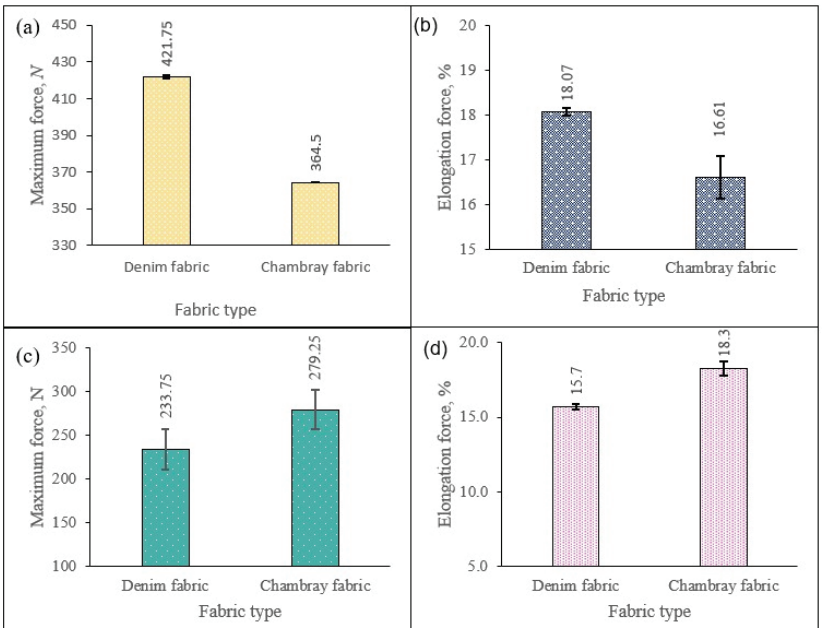

Fig. 3. Warp wise tensile strength: a) maximum force and b) elongation force and weft wise tensile strength; c) maximum force and d) mean elongation force of chambray and denim fabric.

Bio-polymeric denim has a lower weft-direction tensile strength than bio--polymer based chambray, as shown in Fig. 3c and d. In *PPI*, the weft threads are not subjected to a sizing process or other specialized chemical treatment to boost strength. Instead, those are used in smaller quantities. Chambray and denim both

have the same warp and weft counts and a comparable quantity of weft yarn. Chambray outshines denim in weft direction tensile strength with a mean maximum force of almost 280 N due to its lower porosity, higher interlacement point, and higher cross over point. The weft-direction tensile strength of chambray--woven fabrics is higher which is 18.29 % than denim-woven fabrics which is 15.73 % with the same percentage of cellulosic fibers.

Impacts of bio-polymer based chambray and denim fabric on tear strength

Fig. 4 shows that compared to denim, chambray has a greater tear strength in both the warp about 18.42 N and weft directions about 21.27 N whereas denim fabric warp and weft tear strength is 12.68 and 11.93 N, respectively. A study showed that denim is composed of 100 % cotton and features a 3/1 twill weave structure. It has undergone a normal wash process. The warp yarn strength is measured at 16.00 N, while the weft yarn strength is 9.86 N. For performance under heavy loads, a higher tear strength is necessary. It is making sure that holes in the fabric don't get bigger too quickly. On the other hand, chambray is denser and thicker than 3/1 plain weave denim due to its 1/1 twill structure. The lower tear strength of chambray compared to denim is a result of its less compactness and interlacement. The fabric's tear strength allows it to withstand continuous friction.

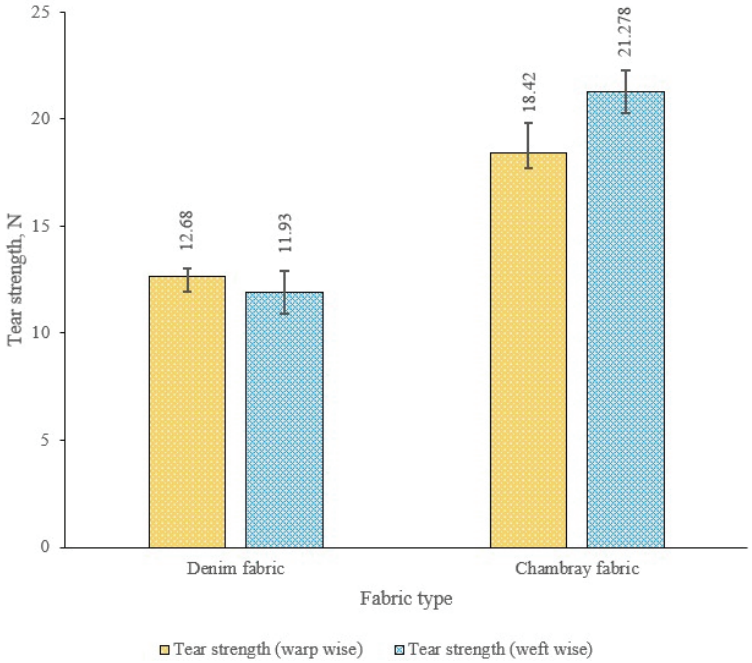

Fig. 4. Analysis of tear strength of chambray and denim fabrics.

Impacts of bio-polymer based chambray and denim fabric on pilling resistance

Table I shows that compared to denim made entirely of cotton, 100 % bio--polymeric cotton chambray resists pilling better. On the front side of the material, pilling occurred. Variations in denim and chambray are graded using a pilling assessment replica after they undergo rotational rubbing action on their faces. Denim exhibits a moderate to severe degree of pilling after 200 cycles, while chambray displays an extremely fine degree of pilling, according to the pilling replica. The study shows that the raw denim exhibited a fabric weight of 163.7 g/m^2 and demonstrated a pilling value of 5.[18] With 500 cycles, denim fabric grades start to show signs of slight pilling, while chambray grades show signs of slight to very slight pilling. After the 2000 cycle, the quality of denim drops to a 3 or 4 (moderate to slight pilling), while the quality of chambray fabric stays the same. As a result, denim's quality declines sharply after 250, 500 or 2000 cycles, while chambray's quality changes slightly. Therefore, chambray outperforms denim in terms of pilling resistance.

TABLE I. Pilling resistance of chambray and denim fabrics

Sample Identity	Cycle	Grade	Comment
100 % Cotton denim fabric	250	4–5	Slight pilling to very slight pilling
	500	4	Slight pilling
	2000	3–4	Moderate pilling to slight pilling
100 % Cotton chambray fabric	250	5	Very slight pilling
	500	4–5	Slight pilling to very slight pilling
	2000	4–5	Slight pilling to very slight pilling

Impacts of bio-polymer based chambray and denim fabrics on abrasion resistance

The mass loss percentage is higher for 100 % cotton denim than for 100% cotton chambray, as illustrated in Fig. 5. The fabric's face surface is the one that gets abrasive. Increased *GSM* and fabric friction led to mass loss. Despite having comparable thread counts, denim boasts two more warp threads and one more weft thread per inch than chambray. This increases the friction, contact surface area, and *GSM* of denim. Compared to chambray, which has a lower *EPI* and *PPI* as well as a smaller surface contact area the reason for its low friction and lower mass loss percentage results in more mass loss per cycle for denim. One of the factors that affects mass loss (%) is the weave structure. Comparing denim and chambray, it is found that denim's 3/1 twill structure makes it more compact and has a higher *GSM* with an average mass loss percentage of 2.471, while chambray's 1/1 plain or poplin structure makes it less compact and has a lower mass loss percentage. According to a study, the abrasion resistance of 100 % cotton denim fabric with a 3/1 Z twill weave decreased by approximately 9.3 % after successive abrasion cycles. This reduction highlights the impact of prolonged mechanical stress on the

fabric's durability.[19] Chambray is more comfortable than denim despite having less abrasion resistance.

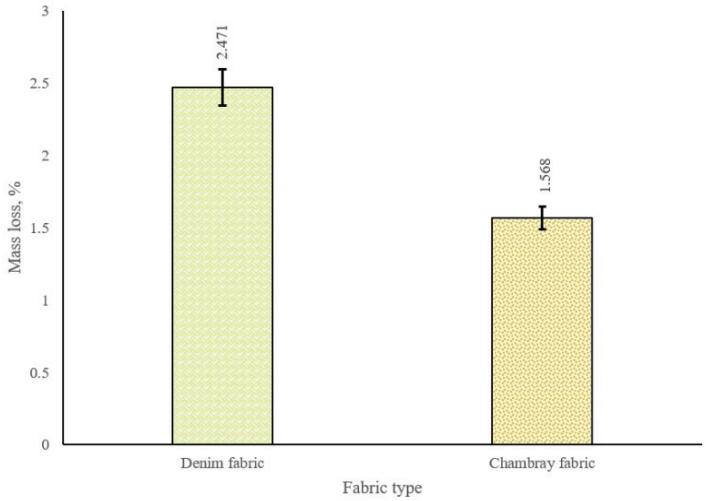

Fig. 5. Analysis of abrasion resistance of chambray and denim fabrics.

Impacts of bio-polymer based chambray and denim fabrics on bursting strength

Fig. 6 clearly shows that denim fabric outperforms chambray fabric in terms of bursting strength with 825 kPa. The fabric's bursting strength indicates the environmental factors that could lead to a rupture. Due to its higher *EPI* and *PPI*, denim can cover the porosity between its yarns, making the fabric better. Due to the reduced number of *EPI* and *PPI*, the bursting strength of chambray fabric is lower which is 695 kPa. However, the plain weave fabric with a warp density of 17 and weft density of 12 demonstrates a bursting strength of 113.06 kPa.[20] Increased bursting strength is another benefit of the weave structure, which supports the fiber. The bursting strength is directly proportional to the structure thickness as a result thinner structure has a lower bursting strength. Hence, compared to chambray fabric with a 1/1 plain weave, denim with a 3/1 twill structure is stronger.

Fastness properties of bio-polymer based denim and chambray fabric

Samples of 100 % cotton denim were subjected to color fastness testing in dry conditions. The results are displayed in Table II. Colorfastness is likely indicated by the intensity or level in the "Dry" column, which ranges from 4 to 5. These ratings are accompanied by qualitative descriptions in the "Comment" column. A rating of 4 was given to most of the samples, which means good color fastness. One sample's color fastness was rated as good to excellent, with a range of 4 to 5. According to these results, the denim samples show good color fastness when it is dry, and some of them may even be very resistant to color bleeding and fading.

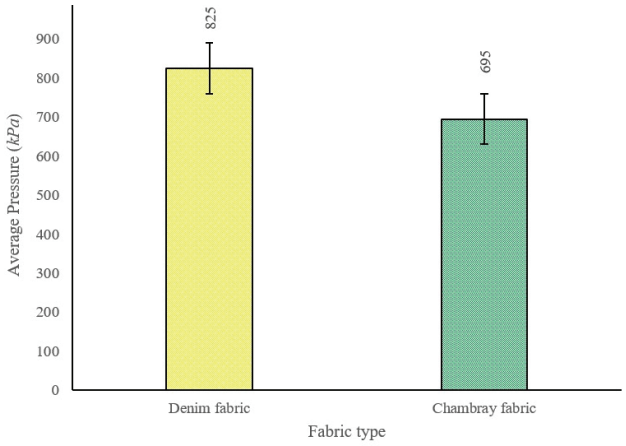

Fig. 6. Analysis of bursting strength of chambray and denim fabrics.

Results from wet-condition color fastness tests on denim samples made of 100% cotton are shown in Table II. A rating of 1 was given to most of the samples, meaning these samples could not hold color well when exposed to water. A colorfastness rating of 1–2 for one sample indicates a very poor to poor quality. All samples showed inadequate performance in resisting color bleeding and fading when exposed to moisture, highlighting a major challenge with color retention in wet conditions.

Table II also presents the findings of color fastness testing conducted on chambray fabric samples in dry conditions. Two samples were rated 4-5, indicating that their color fastness ranged from good to excellent. In addition, one sample attained a rating of 4, indicating satisfactory color fastness, while another sample obtained a rating of 5, indicating exceptional color fastness. The dataset indicates that most of the chambray samples show satisfactory to excellent color retention when exposed to dry conditions. Additionally, certain samples display exceptionally high resistance to color fading or bleeding. TABLE II presents the outcomes of color fastness testing carried out on chambray samples in wet conditions. Two samples were rated 1-2, indicating that color fastness ranged from very poor to poor. In addition, two additional samples were given a rating of 1, indicating extremely low color fastness when exposed to wet conditions.

TABLE II. Rubbing fastness of denim and chambray fabrics in dry and wet conditions

Fabric type	No. of obs.	Grade	Evaluation
	Dry rubbing		
Denim fabric	1	4	Good
	2	4	Good
	3	4–5	Good to excellent
	4	4	Good

TABLE II. Continued

Fabric type	No. of obs.	Grade	Evaluation
	Wet rubbing		
Denim fabric	1	1	Very poor
	2	1–2	Very poor to poor
	3	1	Very poor
	4	1	Very poor
	Dry rubbing		
Chambray fabric	1	4–5	Good to excellent
	2	4	Good
	3	5	Excellent
	4	4–5	Good to excellent
	Wet rubbing		
Chambray fabric	1	1–2	Very poor to poor
	2	1–2	Very poor to poor
	3	1	Very poor
	4	1	Very poor

CONCLUSION

The research work is an approach towards demonstrating the comparison of mechanical and physical properties of bio-polymer based materials such as 3/1 twill denim and 1/1 plain chambray fabric. Though the yarn count and fabric appearances are similar for both fabrics, the mechanical properties like tensile strength, tearing strength, mass loss percentage, abrasion and pilling behavior show different results. According to the results obtained from various tests in this research work, it has been found that the tensile strength of denim fabric in the warp direction is higher than chambray fabric. Which results in less porosity and high interlacement points in bio-polymer based chambray fabric. On the other hand, bio-polymer based denim has higher *EPI* than chambray, it has a higher porosity and a higher crossover point than the 1/1 plain chambray fabric. So, 3/1 twill denim fabric shows higher strength in the warp direction. But on the other hand, chambray fabric has a higher tensile strength in the weft direction than denim. As a result, chambray aids in the design process. Denim has higher tear strength in both warp and weft direction than chambray, bio-polymer based chambray fabric shows better pilling quality than denim fabric. Also, abrasion resistance and bursting strength were higher in denim fabric. The results obtained were classified according to the finished constructions of both types of fabrics and the properties of the yarn. According to the findings from different test results, it will be helpful to decide the suitability of bio-polymer based materials such as denim and chambray fabric for specific end-use.

Acknowledgement. Technical supports from the “ZR Research Institute for Advanced Materials”, Sherpur-2100, Bangladesh are gratefully acknowledged.

ИЗВОД

ИСТРАЖИВАЊЕ ИСТАКНУТИХ ФИЗИЧКО-МЕХАНИЧКИХ КАРАКТЕРИСТИКА БИО-ПОЛИМЕРА НА БАЗИ ЧАМБРЕ ТКАНИНЕ

NASRIN AKTER[1], MD. REAZUDDIN REPON[2], ARNOB D. PRANTA[3,4], MD. RUHUL AMIN[1], NURZOD YUNUSOV[5] и SALIM M. OTAJONOV[5]

[1]Department of Textile Engineering, Ahsanullah University of Science and Technology, Tejgaon I/A, Dhaka-1208, Bangladesh, [2]Department of Bioproducts and Biosystems, School of Chemical Engineering, Aalto University, Vuorimiehentie 1, 02150 Espoo, Finland, [3]ZR Research Institute for Advanced Materials", Sherpur-2100, Bangladesh, [4]Department of Textile Engineering, Mawlana Bhashani Science and Technology University, Santosh, Tangail, 1902, Bangladesh u [5]Department of Technological Education, Fergana State University, Fergana 150100, Uzbekistan

Тексас је познат по својој снази и дуговечности, док је чамбре мекши, удобнији и често се користи за одеће у тренду. Овај истраживачки рад упоређује физичке и механичке особине био-полимера на бази органског памука (100 %) тексаса и органског памука (100 %) чамбре тканине. Док су обе тканине имале идентичне основе и потке, тексас је имао већи *EPI* и *PPI* упркос томе што има упоредиву конструкцију. Тексас има више (5,65 %) грама по квадратном метру (*GSM*) него чамбре што заузврат омогућава већу апсорпцију боје. Док је чамбре имао нижу затезну чврстоћу и чврстоћу на пуцање од 100 % памучног тексаса на бази био-полимера у правцу основе, у смеру потке је било обрнуто. Поред тога, тексас је био много бољи у тесту чврстоће на кидање (6,29 %). Чамбре тканина, с друге стране, показала је мање пилинг понашања. Тест отпорности на абразију дао је одличне резултате за чамбре тканине. Резултати показују да је тексас јачи, компактнији и издржљивији, што га чини погоднијим за тешке услове. Насупрот томе, чамбре нуди мекши осећај, бољу прозрачност и већу удобност током лета, заједно са посебним изгледом за обојеност.

(Примљено 18. јуна, ревидирано 7. јула, прихваћено 3. октобра 2025)

REFERENCES

1. H. S. Yoon, L. G. Occeña, *Int. J. Inf. Manage.* **35** (2015) 352 (https://doi.org/10.1016/J.IJINFOMGT.2015.02.003)
2. A. L. Roggeveen, D. Grewal, J. Karsberg, S. M. Noble, J. Nordfält, V. M. Patrick, E. Schweiger, G. Soysal, A. Dillard, N. Cooper, R. Olson, *J. Retailing* **97** (2021) 81 (https://doi.org/10.1016/J.JRETAI.2020.11.006)
3. A. R. Gwosdow, J. C. Stevens, L. G. Berglund, J. A. J. Stolwijk, *Textile Res. J.* **56** (1986) 574 (https://doi.org/10.1177/004051758605600909)
4. L. Y. Mwaikambo, E. T. N. Bisanda, *Polym. Test.* **18** (1999) 181 (https://doi.org/10.1016/S0142-9418(98)00017-8)
5. A. Ivanovska, M. Reljic, M. Kostic, K. Asanovic, B. Mangovska, *J. Nat. Fibers* **19** (2022) 5465 (https://doi.org/10.1080/15440478.2021.1875383)
6. K. K. Leonas, E. P. Easter, J. O. Dejonge, *Bull. Environ. Contam. Toxicol.* **43** (1989) 231 (https://doi.org/10.1007/BF01701753)
7. M. P. Todor, I. Kiss, V. G. Cioata, *Mater. Today Proc.* **45** (2021) 4150 (https://doi.org/10.1016/J.MATPR.2020.11.927)
8. A. P. Periyasamy, S. Periyasami, *ACS Omega* **8** (2023) 4472 (https://doi.org/10.1021/acsomega.2c06374)

9. K. Z. M. A. Motaleb, A. D. Pranta, F.-E.- Karim, M. R. Islam, S. Islam, J. Janutėnienė, *Funct. Comp. Struct.* **7** (2025) 022002 (https://doi.org/10.1088/2631-6331/add9e0)
10. S. Ahmed, Md. R. Repon, A. D. Pranta, A. Haji, J. Y. Al-Humaidi, M. M. Rahman, *Polym. Eng. Sci.* **65** (2025) 1474 (https://doi.org/10.1002/pen.27102)
11. A. D. Pranta, Md. Tareque Rahaman, Md. Reazuddin Repon, A. A. R. Shikder, *J. Open Innov.: Technol. Market Complex.* **10** (2024) 100357 (https://doi.org/10.1016/j.joitmc.2024.100357)
12. A. Dutta, B. Chatterjee, *Res. J. Text. Apparel* **24** (2020) 53 (https://doi.org/10.1108/RJTA-07-2019-0033)
13. Z. A. Malik, M. H. Malik, T. Hussain, F. A. Arain, *J. Eng. Fiber Fabr.* **6** (2011) (https://doi.org/10.1177/155892501100600407)
14. M.-A. Bueno, B. Lamy, M. Renner, *Wear* **253** (2002) 448 (https://doi.org/10.1016/S0043-1648(02)00146-1)
15. Z. Degirmenci, N. Çelik, *Fibres Text. East. Europe* **24** (2016) 101 (https://doi.org/10.5604/12303666.1170265)
16. N. Akter, Md. R. Repon, A. D. Pranta, S. Islam, A. A. Khan, A. Malik, *SPE Polymers* **5** (2024) 557–567 (https://doi.org/10.1002/pls2.10141)
17. Md. Tareque Rahaman, S. Akter, A. Dhar Pranta, *Int. J. Ind. Manuf. Sys. Eng.* **10** (2021) 10 (https://doi.org/10.11648/j.ijimse.20210601.13)
18. Md. Zayedul Hasan, Md. Tareque Rahaman, T. Islam, A. Dhar Pranta, *Int. J. Ind. Manuf. Sys. Eng.* **6** (2021) 20 (https://doi.org/10.11648/j.ijimse.20210602.11)
19. G. Ren, Y. Song, X. Li, B. Wang, Y. Zhou, Y. Wang, B. Ge, X. Zhu, *J. Coll. Interf. Sci.* **522** (2018) 57 (https://doi.org/10.1016/j.jcis.2018.03.038)
20. H. Özdemir, E. Mert, *J. Text. Inst.* **104** (2013) 330 (https://doi.org/10.1080/00405000.2012.725521).

Journal of the Serbian Chemical Society
JSCS-info@shd.org.rs • www.shd.org.rs/JSCS
J. Serb. Chem. Soc. *91* (2) 195–212 (2026)
JSCS–5486
Original scientific paper
Published 12 February, 2026

Composite materials based on biochar from coffee husk origin and nano zero-valent type Fe/Cu: Potential for treatment of water sources contaminated with As(V)

NGOC TOAN VU[1]*, ANH PHU NGUYEN[2], HONG SON NGUYEN[1], VIET ANH PHAM[1], DINH THAO VU[2] and QUANG MINH LE[3]

[1]*Institute of New Technology, 17, Hoang Sam, Nghia Do, Cau Giay, Hanoi, Vietnam,* [2]*Military Technical Academy, 236, Hoang Quoc Viet, Bac Tu Liem, Hanoi, Vietnam and* [3]*Hanoi–Amsterdam High School for the Gifted, 1, Hoang Minh Giam, Trung Hoa, Cau Giay, Hanoi, Vietnam*

(Received 5 February, revised 6 March, accepted 27 April 2025)

Abstract: In this study, a composite material, Gr–Fe/Cu@BC (CPS), was synthesized using biochar derived from coffee husks and Fe/Cu bimetallic zero-valent nanoparticles for the treatment of water contaminated with As(V). The Fe/Cu bimetallic zero-valent nanoparticles were synthesized *via* a green chemical method employing concentrated *Camellia sinensis* extract as a reducing agent for metal salts. A Box–Behnken experimental design identified optimal conditions for As(V) removal, including a pH range of 5–7, metal/C ratio of approximately 12–13 %, CPS/As mass ratio from 1000 to 1250 and reaction time of around 180 min. The maximum As(V) removal efficiency reached 91.64 % with a maximum adsorption capacity (q_{max}) of 2.86 mg g^{-1}. The adsorption kinetics of As(V) on CPS followed a pseudo-second-order model, with a rate constant (K_2) of 5.96 g mg^{-1} h^{-1}. Furthermore, the structural and surface properties of CPS were characterized using advanced analytical techniques such as SEM, TEM, BET, XRD and EDS, confirming the successful integration of Fe/Cu nanoparticles onto the biochar matrix *via* complexation bonds. These findings highlight the potential of CPS as an environmentally friendly, cost-effective material for the treatment of As(V)-contaminated water and other heavy metal pollutants.

Keywords bimetallic; nanoparticles; water contaminated.

INTRODUCTION

Water contamination by toxic heavy metals, particularly arsenic, has become a significant concern for both environmental safety and human health.[1–3] Arsenic is a toxic element that, upon prolonged exposure, can cause adverse effects on the

* Corresponding author. E-mail: vntoanchem@email.com
https://doi.org/10.2298/JSC250205033V

nervous system, cardiovascular health, dermatological conditions, and liver function.[4,5] Arsenic pollution is now recognized as a global issue, with 21 countries currently facing alarming levels of contamination.[6,7] In particular, regions with naturally elevated geogenic arsenic levels or influenced by anthropogenic activities, such as the Chaco-Pampean plain (Argentina), West Bengal (India), Bangladesh, various parts of Southeast Asia and Limousin (France), have reported serious arsenic contamination in both soil and groundwater sources.[8,9] Inorganic forms of arsenic commonly found in water include As(III) and As(V),[10] with As(V) being highly soluble and mobile in aquatic environments[11] posing substantial challenges to the development of effective remediation technologies. Several conventional methods for arsenic removal have been employed, including ion exchange, coagulation, membrane technologies and adsorption.[1,12–14] Among these, adsorption-based technologies for treating As(V)-contaminated water are widely utilized due to their advantages, such as high removal efficiency, low cost and operational simplicity.[15]

Natural materials have attracted increasing interest as fillers in composite materials due to their widespread availability, cost-effectiveness, straightforward production processes and environmentally friendly nature.[16,17] Coffee husks, a major agricultural by-product of coffee production, represent approximately 30––50 % of the total weight of processed coffee.[18] Vietnam produces approximately 1.47 million tons of coffee annually (2023–2024), generating an estimated 600,000 to 735,000 tons of coffee husks. However, these husks are often underutilized, and their disposal poses environmental challenges.[19] Recent research highlights that composites produced from waste coffee husks exhibit strong potential as adsorbents for removing pollutants from wastewater.[20]

Bimetallic zero-valent nanoparticle systems have emerged as a focal point in environmental remediation research due to their remarkable efficacy in addressing heavy metal contamination.[21–23] Among these, Fe-based bimetallic nanoparticles are particularly noteworthy, offering distinct advantages such as cost-effectiveness, facile synthesis and high catalytic activity. A growing body of evidence underscores that bimetallic zero-valent nanoparticles exhibit superior catalytic performance and enhanced pollutant removal efficiency compared to their monometallic counterparts.[24,25] In recent years, the integration of bimetallic nanoparticles into bio-based matrices has gained prominence as an innovative strategy for nanocomposite synthesis. This approach not only mitigates nanoparticle aggregation but also capitalizes on renewable biomass resources. Shen *et al.*[26] synthesized Fe/Cu bimetallic catalysts supported on biochar derived from paper mill waste, achieving efficient removal of rhodamine B dye. Similarly, Ahmed *et al.*[27] fabricated green Fe/Cu composites using alginate and limestone as substrates for dye degradation in aqueous systems. Additionally, Hoa *et al.*[28] developed Fe/ /Cu@MCM-41 nanomaterials and demonstrated their efficacy in treating reactive

red 195 dye. Collectively, these studies underscore the potential of bimetallic nanocomposites as advanced materials for water treatment applications while highlighting their broader applicability in modern environmental remediation technologies.

This study aims to establish a synthesis protocol for composite materials based on biochar (BC) derived from coffee husks and bimetallic zero-valent nanoparticles Gr–Fe/Cu@BC (CPS). In this process, metal salts react with a concentrated green tea extract (*Camellia sinensis*) as a reducing agent to generate nanoparticles anchored onto the BC matrix. The removal of As(V) from water using CPS was systematically investigated by evaluating key influencing factors, including pH, component ratios and reaction time. Optimal conditions were determined using a response surface methodology approach. The findings of this study provide a foundation for harnessing the potential of CPS in wastewater treatment, particularly for the remediation of heavy metal contaminants.

EXPERIMENTAL

Materials

The chemicals utilized in this study include iron(III) chloride hexahydrate (≥99 %, Xilong, China), copper chloride dihydrate (≥ 99 %, Xilong, China) and concentrated green tea extract (~90 % polyphenols), which was synthesized in our previous study;[29] sodium hydrogen arsenate, $Na_2HAsO_4{\cdot}7H_2O$ (≥99 %, Xilong, China); coffee husks collected from the Đăk Lăk region of the Central Highlands, Vietnam (coordinates 13°06'15.1"N, 108°18'14.9"E), were employed. Other analytical-grade chemicals were used for pH adjustment and desorption processes as needed.

Synthesis of BC

BC was synthesized using a pyrolysis method. Coffee husks (or coffee shells) were thoroughly washed and dried. Approximately 100 g of the coffee husks were placed in a perforated metal container with holes in the lid. The material was then pyrolyzed at 450 °C for 60 min, with the temperature precisely controlled in an SX2-5-12 muffle furnace (China) and allowed to cool naturally. The resulting product was manually ground and sieved through a mesh with a pore size of 0.14 mm to obtain fine powder-form BC (Fig. 1).

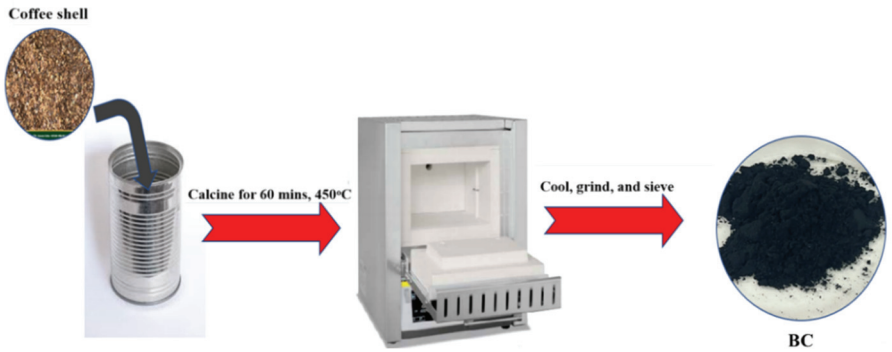

Fig. 1. Synthesis of carbon-based BC material from coffee husk.

Synthesis of CPS

A specified amount of BC was weighed into a 250 mL glass beaker, to which 70 mL of ultrapure water was added. The mixture was stirred at 300 rpm for 15 min at room temperature. A solution of $FeCl_3 \cdot 6H_2O$ and $CuCl_2 \cdot 2H_2O$ was then gradually added to the beaker. Subsequently, a green tea extract solution (green tea powder in water) was slowly introduced into the stirring mixture. The optimal ratio of metal salts and green tea solution was previously reported in our study.[29] The stirring speed was increased to approximately 600 rpm and maintained for 2 h. Afterward, the stirring was stopped and the solution was allowed to stabilize for 5–6 h. The solid product was then filtered, washed three times with 99 % ethanol and transferred to a desiccator for vacuum drying. The final product was left to dry naturally for 8––12 h. The resulting material exhibited a black color and high porosity. The process is schematically represented in Fig. 2.

Fig. 2. Synthesis process of CPS composite.

As(V) removal experiment

A measured quantity of 0.5 g of CPS adsorbent material was placed into a 250 mL Erlenmeyer flask. Subsequently, 100 mL of an As(V) solution with an initial concentration of 5 mg L^{-1} was added to the flask. The mixture was stirred using a magnetic stirrer at 300 rpm under controlled conditions for the designated reaction time. Upon completion of the reaction, the solution was filtered to separate the solid adsorbent and the residual As(V) concentration in the filtrate was analyzed using inductively coupled plasma mass spectrometry (ICP-MS, Agilent 7900, USA). To evaluate the comparative As(V) removal performance, identical experiments were conducted using BC and mono-metallic Gr–12 %Fe/C (containing 12 wt.% Fe) under the same experimental conditions. The removal efficiency of As(V) was calculated using the following formula:

$$R = 100\frac{c_0 - c_t}{c_0} \tag{1}$$

where c_0 (mg L^{-1}) is the initial concentration of As(V), c_t (mg L^{-1}) is the residual concentration of As(V) after treatment.

The post-reaction mixture was filtered to recover the solid material, which was then subjected to desorption by drying at 70 °C for 8 h. This process was repeated over five consecutive cycles to evaluate the reusability of the CPS material.

The setting parameters for the ICP-MS analysis are presented in Table I.

The response surface methodology (RSM) was employed to evaluate the influence of various parameters and optimize the removal efficiency of As(V) from water. A Box–Behnken

experimental design was utilized, involving four independent variables and a fourth-order regression model. The design comprised 30 randomized experimental runs, including five replicates at the center point to ensure statistical reliability. Preliminary exploratory experiments helped define the independent variables and their ranges for the optimization study: pH (X_1, 3––11), reaction time (X_2, 20–180 min), CPS/As mass ratio (X_3, 500–1500), metal/C ratio (X_4, 11––15 %). These variables were coded according to:

$$Y = \beta_0 + \sum_{i-1}^{4} \beta_i X_i + \sum_{i-1}^{4} \beta_{ii} X_i^2 + \sum_{i-1}^{4} \sum_{j-i+1}^{4} \beta_{ij} X_i X_j \quad (2)$$

where Y is the predicted response, X_i and X_j are the coded levels of the independent variables, β_0 is a constant, β_i, β_{ii} and β_{ij} are the model coefficients representing linear, quadratic and interaction effects of variables.

TABLE I. Parameters of ICP-MS setting

Parameter	Value
Forward power	1550 W
Plasma gas	15 L min^{-1}
Kinetic energy discrimination (KED)	3 V
Helium collision gas	No gas
Integration time/point	0.2 s
Replicates	3

Based on Design Expert 13 software, an experimental plan was developed based on the parameters listed in Table II.

TABLE II. Scope of experimental planning of 4 factors

Factor	Unit	Signal	Level				
			–2	–1	0	1	2
A: pH	–	X_1	3	5	7	9	11
B: Reaction time	min	X_2	20	60	100	140	180
C: CPS/As	–	X_3	500	750	1000	1250	1500
D: Metal/C	%	X_4	11	12	13	14	15

Characterization of CPS

The CPS material with the highest As(V) removal efficiency was subjected to comprehensive characterization to assess its structural and compositional properties. The surface morphology of the CPS was analyzed using a scanning electron microscope (SEM, Hitachi S-4800, Japan) and high-resolution transmission electron microscopy (HR-TEM, JEM-2100, Japan). The specific surface area and pore size distribution were determined through Brunauer––Emmett–Teller (BET) analysis (TriStar II 3020, UK). Elemental composition was measured using energy-dispersive X-ray spectroscopy (EDX, Shimadzu EDX-8000, Japan). Additionally, X-ray diffraction (XRD, Panalytical, the Netherlands) was employed to examine the crystalline structure and confirm the formation of crystal phases in the CPS material.

RESULTS AND DISCUSSION

Optimization of As(V) removal conditions using CPS

The efficiency of As(V) removal from aqueous solutions was optimized using a Box–Behnken experimental design. The removal efficiencies obtained under various experimental conditions are presented in Table S-I of the Supplementary material to this paper, ranging from 20.12 to 91.64 %. The highest removal efficiency of 91.64 % was achieved under the conditions of pH 5, reaction time of 140 min, CPS/As mass ratio of 1250 and Fe/Cu ratio of 12 %. By applying multiple regression analysis to the experimental data, the relationship between the response variable (removal efficiency) and the independent variables was modeled using the following second-order polynomial:

$$\begin{aligned} Y = &-229.91782 - 6.45998X_1 + 1.56629X_2 + 0.182551X_3 + 23.76856X_4 - \\ &-0.000952X_1X_2 - 0.000510X_1X_3 + 2.38515X_1X_4 - 0.000193X_2X_3 - \\ &-0.054175X_2X_4 + 0.006548X_3X_4 - 2.12070X_1^2 - 0.001970X_2^2 - \\ &-0.000099X_3^2 - 1.65733X_4^2 \end{aligned} \quad (3)$$

Table III presents the results of the analysis of variance (ANOVA) for the quadratic model. The model exhibited an overall F-value = 17.23 and p-value < 0.0001, indicating its statistical significance at a high confidence level. However, the lack of fit test yielded F-value = 12.93 and p-value = 0.0056, suggesting some discrepancies between the model predictions and the observed data. The analysis of individual factors revealed that pH, reaction time and the CPS/As ratio were the most influential variables on the As(V) removal efficiency, with p-values < 0.0001.

TABLE III. Analysis of variance (ANOVA) for the regression equation

Source	Sum of squares	*df*	Mean square	*F*-value	*p*-value
Model	15112.48	14	1079.46	17.23	< 0.0001
X_1-pH	4124.36	1	4124.36	65.84	< 0.0001
X_2-Time	2762.84	1	2762.84	44.11	< 0.0001
X_3-VL/As	3889.84	1	3889.84	62.10	< 0.0001
X_4-%Fe/Cu	53.67	1	53.67	0.8569	0.3693
X_1X_2	0.0928	1	0.0928	0.0015	0.9698
X_1X_3	1.04	1	1.04	0.0166	0.8992
X_1X_4	364.09	1	364.09	5.81	0.0292
X_2X_3	59.65	1	59.65	0.9523	0.3446
X_2X_4	75.14	1	75.14	1.20	0.2907
X_3X_4	42.88	1	42.88	0.6845	0.4210
Residual	939.60	15	62.64		
Lack of fit	904.62	10	90.46	12.93	0.0056
Pure Eerror	34.98	5	7.00		
Cor total	16052.08	29			

Among these, pH was identified as the most significant factor, exhibiting the highest F-value = 65.84. Conversely, the Metal/C ratio demonstrated a comparatively lower influence, with p-value = 0.3693. The interaction between X_1 and X_4 was found to be statistically significant ($F = 5.81$, $p = 0.0292$), indicating that their combined effect contributed to the efficiency. However, this interaction was less impactful compared to the primary effects of pH and reaction time. Other interactions, including X_1X_2, X_1X_3, X_2X_3, X_2X_4, and X_3X_4 were not statistically significant ($p > 0.05$), suggesting that these factors largely influenced the response independently rather than through synergistic interactions.

Fig. 3a–d presents the 3D response surface plots illustrating the interactive effects of input factors on the removal efficiency of As(V). In Fig. 3a, the interaction between the metal/C ratio and pH indicates that the removal efficiency is highest at a near-neutral pH (5–7). This aligns with the optimal condition to prevent excessive agglomeration of Fe/Cu nanoparticles or reduced material activity in strongly acidic or alkaline environments. Fig. 3b depicts the relationship between CPS/As and pH, showing that increasing CPS concentration under neutral pH conditions significantly enhances removal efficiency due to stronger adsorption capacity. Fig. 3c highlights the combined effect of metal/C and CPS/As, where the removal efficiency peaks at an optimal metal/C ratio of approximately 12–13 %. This is consistent with the uniform surface structure and the enhanced catalytic activity of CPS. The influence of pH and reaction time, as shown in Fig. 3d, indicates that an optimal reaction time of approximately 180 min provides ideal conditions for efficient adsorption and reduction reactions. Fig. 3e shows the correlation between experimental and predicted values of As(V) removal efficiency. The data points are closely aligned along the diagonal, demonstrating the high accuracy of the regression model in predicting outcomes. Finally, the residuals plot (Fig. 3f) reveals that residuals are randomly distributed around zero, with no systematic deviation or trend. This ensures the validity of the statistical model and confirms that the selected input variables are appropriately controlled. In conclusion, the optimization results indicate that CPS performs most effectively under neutral pH (5–7), a metal/C ratio of approximately 12–13 %, CPS/As from 1000 to 1250 and a reaction time of around 180 min. These findings demonstrate the material's potential as a promising solution for As(V) remediation in water.

Adsorption kinetics

The adsorption kinetics model was employed to describe the process of As(V) adsorption onto the surface of CPS. Experimental data were utilized to evaluate the applicability of different kinetic models, including the pseudo-first-order and pseudo-second-order models. These models are mathematically expressed by the following equations:

$$\text{Pseudo-first-order: } \ln(q_e - q_t) = \ln q_e - K_1 t \quad (4)$$

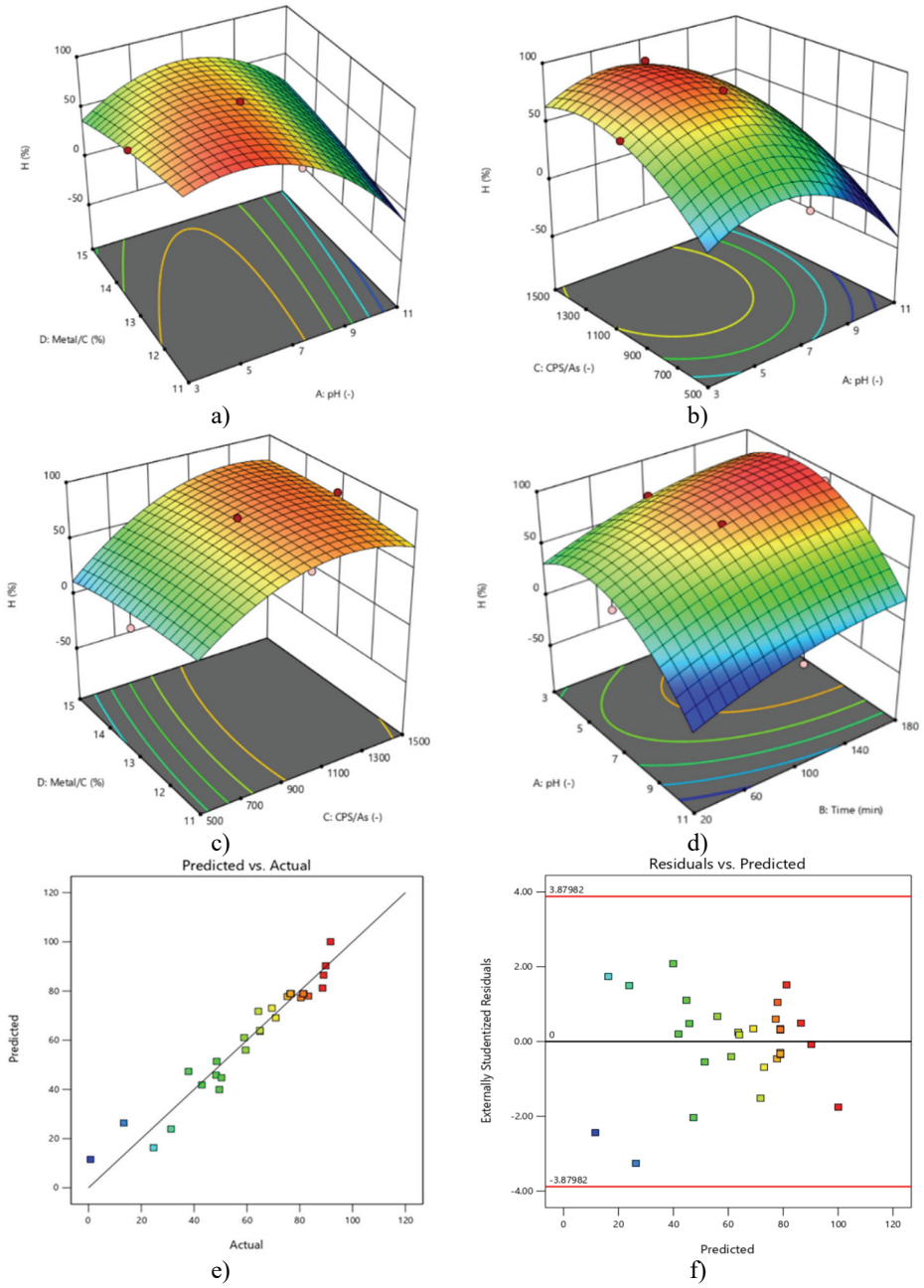

Fig. 3. a–d) RSM model evaluates the influence of factors on As(V) treatment efficiency; e–f) difference between standard data and experimental data.

$$\text{Pseudo-second-order: } \frac{t}{q_t} = \frac{1}{K_2 q_e^2} + \frac{1}{q_e} t \quad (5)$$

where q_e and q_t represent the amount of As(V) adsorbed at equilibrium and at time t, respectively (mg g^{-1}). K_1 and K_2 are the equilibrium rate constants for the pseudo-first-order and pseudo-second-order kinetic models, respectively.

The results depicted in Fig. 4 indicate that the pseudo-second-order kinetic model provides a better fit to the experimental data. This suggests that the adsorption efficiency is influenced by both the concentration of As(V) and the availability of adsorption sites on the material's surface. The kinetic constants and half-adsorption times determined for the studied system are summarized in Table IV.

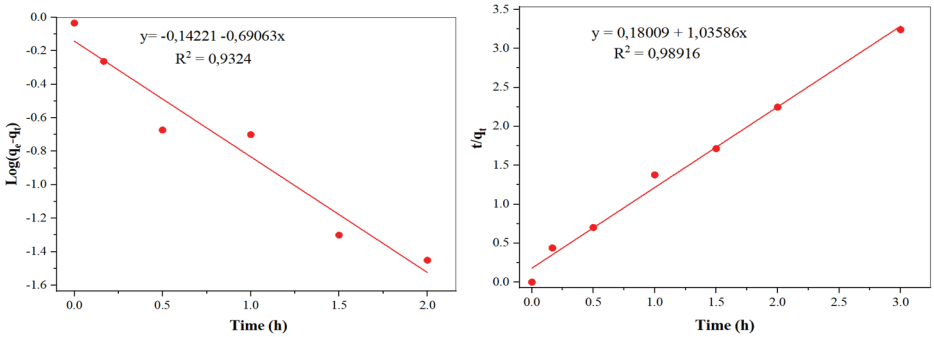

(a) (b)

Fig. 4. a) Pseudo-first-order; b) pseudo-second-order kinetics.

The suitability of the pseudo-second-order model also indicates strong interactions between As(V) ions and the surface of the adsorbent, consistent with a chemisorption mechanism. This suggests that chemical adsorption is the dominant process, overcoming the electrostatic repulsion barrier arising from the electrostatic forces between the composite and As(V) ions.[30] The chemisorption mechanism has been attributed to the formation of surface complexes, where most As(V) ions replace two singly coordinated surface OH groups to form binuclear bridging complexes, specifically Fe–O–AsO(OH)–O–Fe.[31,32]

TABLE IV. Kinetic parameters of As(V) adsorption reaction on CPS

Kinetic model	$K_{1,2}$	$t_{1/2}$	R^2
Pseudo-first-order	0.6906	~1 h	0.9324
Pseudo-second-order	5.96 g mg^{-1} h^{-1}	10.44 min	0.9892

The adsorption isotherms serve to describe the interactions between CPS and the adsorbed species, As(V), at equilibrium. In this study, equilibrium adsorption data for As(V) onto CPS were analyzed using two widely employed two-parameter

isotherm models, Langmuir and Freundlich. These models are mathematically expressed as follows:

$$\text{Langmuir isotherm: } \frac{1}{q_e} = \frac{1}{q_{max} K_L c_e} + \frac{1}{q_{max}} \quad (6)$$

$$\text{Freundlich isotherm: } \ln q_e = \frac{1}{n} \ln c_e + \ln K_F \quad (7)$$

where q_{max} represents the maximum adsorption capacity (mg g^{-1}), K_L is the Langmuir adsorption constant (L mg^{-1}), K_F denotes the Freundlich adsorption constant, and n is the empirical parameter indicative of the adsorption intensity.

The results presented in Fig. 5 demonstrate that the adsorption of As(V) onto CPS follows the Langmuir isotherm model, with a correlation coefficient R^2 = = 0.978, indicating that the predominant adsorption mechanism is monolayer adsorption. The maximum adsorption capacity q_{max} = 2.86 mg g^{-1}, while the Langmuir adsorption constant K_L = 0.82 L mg^{-1}, reflecting the affinity of CPS for As(V). These findings suggest that the adsorption of As(V) occurs on a homogeneous surface of CPS, and the interaction between adsorbed molecules is negligible.

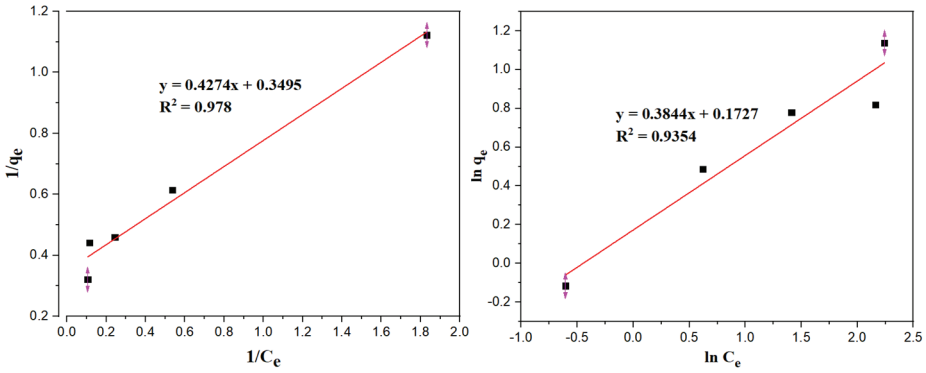

Fig 5. Langmuir and Freundlich isotherm models.

Characterizations of CPS-12%

The BC and composite sample with metal/C = 12 % (CPS-12%) were synthesized and characterized to determine their surface properties. The results, shown in Fig. 6, illustrate the surface morphology of the materials. The BC, after calcination, exists in the form of flakes and relatively fine particles with an average size of approximately 200 nm. The surface of CPS-12% reveals the dispersion of nanoparticles with sizes < 50 nm, adhering to the BC substrate. The nanoparticle distribution on the BC substrate is non-uniform, with some areas showing agglomeration, likely due to the reaction between Fe^{2+}, Cu^{2+} and polyphenolic compounds in the concentrated green tea solution. Additionally, some regions exhibit large gaps between the particles. Analysis of the HR-TEM images of the CPS-12%

sample (Fig. 6c and d) reveals a well-defined crystalline structure with distinct lattice fringes, confirming the successful formation of Fe/Cu nanoparticles. The presence of slightly disordered stacking layers (Fig. 6d) indicates a partially amorphous graphitic carbon support, which is commonly observed in high-surface-area carbon-based materials. The absence of detectable impurity phases suggests that the synthesis method effectively yielded a clean Fe/Cu bimetallic phase uniformly dispersed on the carbon matrix, highlighting its potential for applications in energy storage and catalytic processes. The agglomeration phenomenon in CPS-12% is significantly reduced compared to nanoparticles synthesized via green methods in previous studies by Fang *et al.* [33], and Peili *et al.*[34]

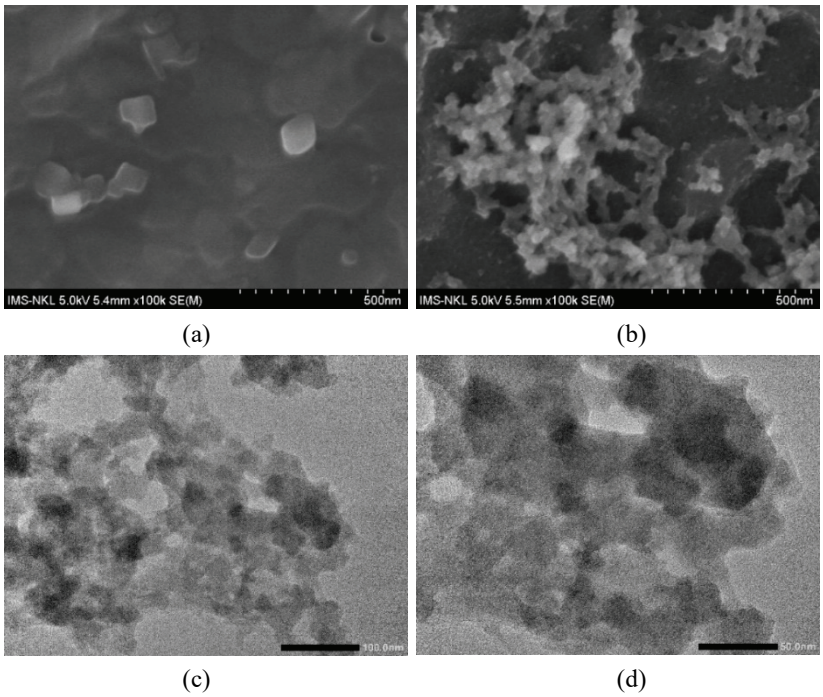

Fig. 6. SEM images of: a) BC from coffee grounds, b) CPS-12%; c,d) HR-TEM images of CPS-12%.

The EDS spectrum results presented in Fig. 7a indicate that the main component of the BC sample is carbon, with a content of 69.88 %, which reflects the carbon-rich nature of the BC. Oxygen constitutes 20.48 %, suggesting the presence of oxidized functional groups on the surface. Elements such as potassium account for 5.08 %, while silicon, phosphorus and sulfur appear at trace levels (< 0.2 %), which may originate from the biomass material or the thermal treatment process.

These characteristics confirm that BC is a stable carbon-based substrate, with surface chemical properties suitable for anchoring metal nanoparticles. The EDS spectrum of the CPS-12 % sample, shown in Fig. 7b, reveals a significant change in composition. The presence of Fe (4.36 %) and Cu (0.37 %) confirms the successful attachment of Fe/Cu nanoparticles onto the BC. Additionally, elements such as P and chlorine (Cl) are detected at low levels, which may be related to impurities or side reactions during the synthesis process.

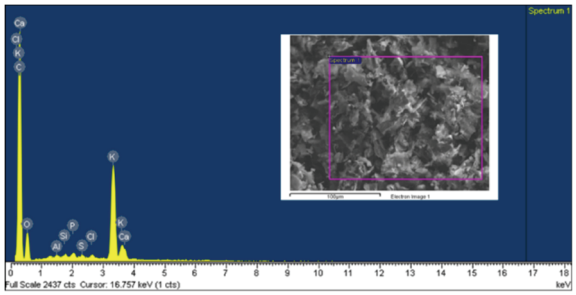

a)

Element	Weight%	Atomic%
C	69.88	79.15
O	20.48	17.41
Al	0.15	0.07
Si	0.18	0.09
P	0.28	0.12
S	0.15	0.06
Cl	0.22	0.08
K	8.08	2.81
Ca	0.58	0.20
Totals	100.00	

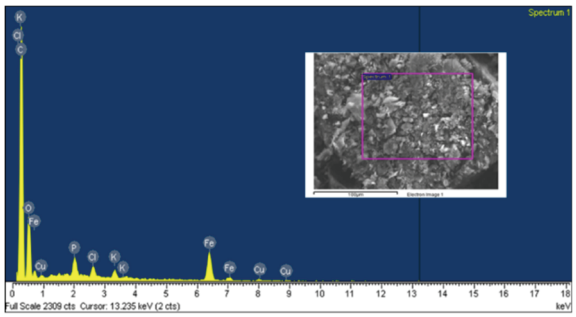

b)

Element	Weight%	Atomic%
C	67.05	75.75
O	26.37	22.37
P	0.87	0.38
Cl	0.53	0.20
K	0.45	0.15
Fe	4.36	1.06
Cu	0.37	0.08
Totals	100.00	

Fig. 7. EDS spectra of: a) BC; b) CPS-12%.

The BET data presented in Fig. 8a–c demonstrate that both BC and CPS-12% exhibit Type IV isotherms, characteristic of mesoporous materials. However, when comparing the two samples, the incorporation of Fe/Cu onto the carbon substrate leads to a slight decrease in specific surface area (from 118.32 to 115.26 $m^2 g^{-1}$), while the pore volume increases (from 0.1026 to 0.1177 $cm^3 g^{-1}$). This can be attributed to the deposition of Fe/Cu nanoparticles within the pores, which reduces the average pore size from 50.94 to 44.80 Å, while enhancing pore formation and maintaining the porous structure. Despite these changes, the variation in specific surface area between the two samples is minimal, indicating that the Fe/Cu nanoparticles deposited on the BC surface do not cause significant structural changes. These alterations contribute to an increased surface interaction and enhanced catalytic efficiency of CPS-12%.

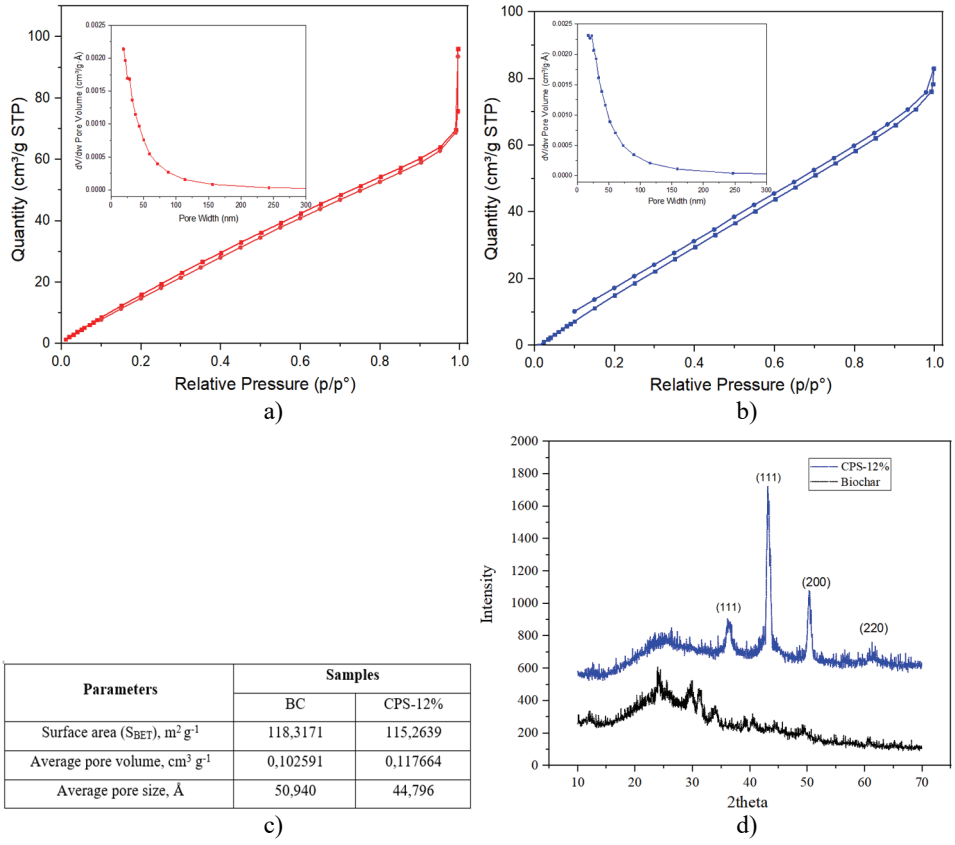

Parameters	Samples	
	BC	CPS-12%
Surface area (S_{BET}), $m^2 g^{-1}$	118,3171	115,2639
Average pore volume, $cm^3 g^{-1}$	0,102591	0,117664
Average pore size, Å	50,940	44,796

Fig. 8. BET isotherms of: a) BC and b) CPS-12%; c) BET characteristic parameters of BC and CPS-12%; d) XRD of BC and CPS-12%.

As shown in Fig. 8d, the XRD pattern of the initial BC exhibits a broad peak, indicating the amorphous nature of the carbon phase, with characteristic peaks primarily representing the presence of lignocellulose structures.[35,36] The XRD pattern of CPS-12% reveals sharp diffraction peaks. The peak at 2θ 36.1° corresponds to Cu(I) crystals, while the presence of Cu(0) is indicated by peaks at 2θ 43.1 and 50.4°.[37,38] A faint and broad peak at approximately 2θ 44–45° suggests the presence of Fe(0). Additionally, the peak at 2θ 61.2° likely represents the Fe_3C crystals (JCPDS 35-0772),[39] formed due to the interaction between Fe and carbon in the BC substrate.

Comparison of As(V) removal efficiency and reusability of CPS

The results presented in Fig. 9a reflect the As(V) removal efficiency of three samples: BC, Gr–12%Fe@BC and CPS-12%. The As(V) concentration remained almost unchanged when using the pristine BC due to its limited properties, such as

small pore size and low surface functionality. Pristine BC encountered performance limitations when not surface-modified.[40] Surface modification of BC with single-metal Fe nanoparticles, as seen in Gr–12%Fe@BC, led to approximately 60 % As(V) removal at equilibrium. A notable increase in As(V) removal efficiency was observed upon the incorporation of the transition metal Cu to form the Fe/Cu bimetallic system. This enhancement can be attributed to the synergistic effect between Fe and Cu. Pamela *et al.*[41] assume the existence of Cu facilitated electron transfer among Fe, Cu and As, which increased the adsorption rate, capacity and intensity. O'Carrol *et al.*[42] stated that the second metal, in this case Cu, acts as an electronic mediator that catalyzes and increases the removal rates by bimetallic nanoparticles by decreasing the activation energy of the reaction.

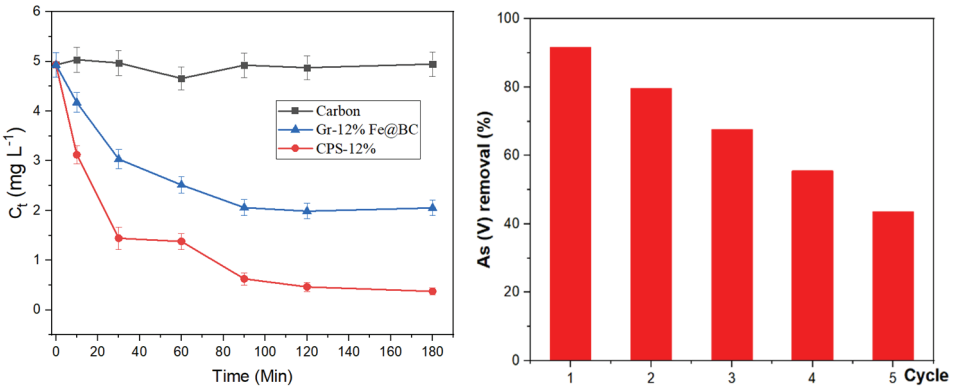

Fig. 9. a) Comparison of As(V) removal efficiency by BC, Gr–12%Fe@BC and CPS-12%; b) As(V) removal efficiency of CPS-12% over 5 reuse cycles.

The decline in As(V) removal efficiency from 91.64 to 45.52 % after five reuse cycles of CPS-12% is depicted in Fig. 9b. Catalytic activity declines primarily due to oxide and hydroxide layers forming on the CPS surface after each treatment cycle, which block Fe–O–As complex formation. Furthermore, partial dissolution of Cu in the CPS under pH conditions of 5–7 ($Cu + 2H^+ \rightarrow Cu^{2+} + + H_2$). The depletion of Cu content reduces the electron transfer rate between Fe and Cu, thereby diminishing the efficiency of the reductive reactions responsible for As(V) removal.[43]

Comparison of As(V) removal efficiency with some other materials

The results in Table V demonstrate a range of removal efficiencies for arsenic and other heavy metals using different materials under varying pH conditions. Most materials achieved moderate efficiencies between 70 and 90 %, often requiring acidic or slightly alkaline environments to perform optimally. In contrast, the CPS material developed in this study exhibited a notably higher As(V) removal

efficiency of 91.64 % at neutral pH, suggesting its superior potential for practical water treatment applications without the need for extensive pH adjustment. This highlights CPS as a promising and efficient alternative among existing materials.

TABLE V. Comparison of heavy metal removal efficiency by materials

No.	Material	Pollutants	Removal efficiency	Ref.
1	Fe_3O_4/AC	As	70 % at pH 8	Joshi *et al.*[44]
2	Bimetallic $Fe_{0.9}Cu_{0.1}$	As(V)	75.223 %	Sepúlveda *et al.*[41]
3	Nano carbon with zirconium	As	70–75 % at pH 2–3	Mahanta *et al.*[45]
4	Carbon/$Fe_3(Mn^{2+})O_4$	As(V)	70–90 % at pH 3	Gallios *et al.*[46]
5	Nano bimetallic Cu–Ni	Cd (II)	70 % at pH 7	Harikumar *et al.*[47]
6	CPS	As (V)	91.64 % at pH 7	This study

CONCLUSION

This study successfully demonstrated the green chemical synthesis of a composite material, CPS, utilizing biochar derived from coffee husks and bimetallic Fe/Cu nanoparticles. The adsorption kinetics were well-fitted to a pseudo-second-order kinetic model, indicating stable and rapid As(V) removal capabilities. Structural analysis confirmed the formation of Fe/Cu nanoparticles with sizes smaller than 50 nm dispersed on the BC matrix. The optimization outcomes further revealed that CPS performs most effectively under near-neutral pH conditions (5–7), with a metal/carbon mass ratio of 0.12–0.13, a CPS/arsenic mass ratio between 1000 and 1250, and a reaction time of approximately 180 min. These findings highlight CPS as a low-cost, environmentally friendly adsorbent with significant potential for applications in the treatment of As(V)-contaminated wastewater. With its sustainability, high efficiency, and reusability over multiple cycles, this research provides valuable insights into the development of advanced adsorbent materials based on renewable resources and green technologies for environmental remediation.

SUPPLEMENTARY MATERIAL

Additional data and information are available electronically at the pages of journal website: https://www.shd-pub.org.rs/index.php/JSCS/article/view/13238, or from the corresponding author on request.

Acknowledgement. The authors acknowledge the facilities and the scientific and technical assistance at the Institute of New Technology/Vietnam.

ИЗВОД

КОМПОЗИТНИ МАТЕРИЈАЛИ НА БАЗИ БИОУГЉА ДОБИЈЕНОГ ОД ЉУСКЕ КАФЕ И НАНО Fe/Cu ЧЕСТИЦА НУЛТОГ ВАЛЕНТНОГ СТАЊА: ПОТЕНЦИЈАЛ ЗА ТРЕТМАН ВОДА КОНТАМИНИРАНИХ АРСЕНОМ(V)

NGOC TOAN VU[1], ANH PHU NGUYEN[2], HONG SON NGUYEN[1], VIET ANH PHAM[1], DINH THAO VU[2] и QUANG MINH LE[3]

[1]Institute of New Technology, 17, Hoang Sam, Nghia Do, Cau Giay, Hanoi, Vietnam, [2]Military Technical Academy, 236, Hoang Quoc Viet, Bac Tu Liem, Hanoi, Vietnam u [3]Hanoi–Amsterdam High School for the Gifted, 1, Hoang Minh Giam, Trung Hoa, Cau Giay, Hanoi, Vietnam

У овом истраживању синтетизован је композитни материјал Gr–Fe/Cu@BC (CPS) употребом биоугља добијеног од љуски кафе и биметалних нултовалентних наночестица Fe/Cu за третман воде контаминиране арсеном(V). Биметалне нултовалентне наночестице Fe/Cu синтетизоване су применом методе "зелене" хемије, користећи концентровани екстракт *Camellia sinensis* као редукционо средство за металне соли. Дизајн експеримента по Box–Behnken моделу идентификовао је оптималне услове за уклањање As(V), укључујући pH у опсегу од 5 до 7, масени однос метал/угљеник од приближно 0,12–0,13, масени однос CPS/As у распону од 1000 до 1250 и време реакције око 180 min. Максимална ефикасност уклањања As(V) достигла је 91,64 %, уз максимални адсорпциони капацитет (q_{max}) од 2,86 mg g^{-1}. Кинетика адсорпције As(V) на CPS пратила је модел псеудо-другог реда, са константом брзине (K_2) од 5,96 g mg^{-1} h^{-1}. Структурне и површинске карактеристике CPS материјала окарактерисане су напредним аналитичким техникама као што су SEM, TEM, BET, XRD и EDS, чиме је потврђена успешна интеграција наночестица Fe/Cu у матрицу биоугља путем координационих веза. Ови резултати указују на потенцијал CPS материјала као еколошки прихватљивог и економичног решења за третман воде контаминиране As(V), као и других загађивача тешким металима.

(Примљено 5. фебруара, ревидирано 6. марта, прихваћено 27. априла 2025)

REFERENCES

1. M. Chiban, G. Carja, G. Lehutu, F. Sinan, *Arab. J. Chem.* **9** (2016) 988 (https://doi.org/10.1016/j.arabjc.2011.10.002)
2. H. Alalwan, A. Alminshid, M. Mohammed, M. Mohammed, M. Shadhar, *Nanomaterials* **8** (2022) 995 (https://doi.org/10.22059/POLL.2022.337436.1329)
3. S. O. Kazantsev, K. V. Suliz, N. G. Rodkevich, A. S. Lozhkomoev, *Materials* **16** (2023) 6057 (https://doi.org/10.3390/ma16176057)
4. K. S. Patel, P. K. Pandey, P. Martín-Ramos, W. T. Corns, S. Varol, P. Bhattacharya, Y. Zhu, *RSC Adv.* **13** (2023) 8803 (10.1039/d3ra00789h)
5. R. N. Ratnaike, *Postgrad. Med. J.* **79** (2003) 391 (https://doi.org/10.1136/pmj.79.933.391)
6. P. Bhattacharyya, Md. M. Alam, in *Contaminants in Agriculture: Sources, Impacts and Management*, M. Naeem, A. A. Ansari, S. Singh Gill, Eds., Springer, Berlin, 2020, pp. 327–337 (https://doi.org/10.1007/978-3-030-41552-5_16)
7. A. Shrivastava, A. Barla, S. Singh, S. Mandraha, S. Bose, *J. Hazard. Mater.* **324** (2017) 526 (https://doi.org/10.1016/j.jhazmat.2016.11.022)
8. V. Antoni, N. Saby, D. Arrouays, C. Jolivet, L. Boulonne, C. Ratie, A. Bispo, T. Eglin, A. Pierart, A. Gay, J.-L. Perrin, I. Joassard, 2019, available at https://www.researchgate.net/publication/331648803_Arsenic_et_mercure_dans_les_sols_francais_pollutions_diffuses_et_ponctuelles

9. R. Singh, S. Singh, P. Parihar, V. P. Singh, S. M. Prasad, *Ecotoxicol. Environ. Saf.* **112** (2015) 247 (https://doi.org/10.1016/j.ecoenv.2014.10.009)
10. X. Ren, H. Feng, M. Zhao, X. Zhou, X. Zhu, X. Ouyang, J. Tang, C. Li, J. Wang, W. Tang, L. Tang, *Int. J. Environ. Res. Pub. Health* **20** (2023) 3829 (https://doi.org/10.3390/ijerph20053829)
11. K. Wrighton-Araneda, D. Cortés-Arriagada, *Chem. Eng. J.* **426** (2021) 131471 (https://doi.org/10.1016/j.cej.2021.131471)
12. H. Saitua, R. Gil, A. P. Padilla, *Desalination* **274** (2011) 1 (https://doi.org/10.1016/j.desal.2011.02.044)
13. L. A. Zemskova, A. V. Voit, D. K. Shlyk, N. N. Barinov, *Russ. J. Appl. Chem.* **89** (2016) 727 (https://doi.org/10.1134/S1070427216050074)
14. G. Zhang, X. Li, S. Wu, P. Gu, *Environ. Earth Sci.* **66** (2012) 1269 (https://doi.org/10.1007/s12665-012-1549-7)
15. Z. Moradi, A. Alihosseini, A. Ghadami, *Res. Mat.* **17** (2023) 100378 (https://doi.org/10.1016/j.rinma.2023.100378)
16. A. Fouly, H. S. Abdo, A. H. Seikh, K. Alluhydan, H. I. Alkhammash, I. A. Alnaser, M. S. Abdo, *Polymers* **13** (2021) 4407 (https://doi.org/10.3390/polym13244407)
17. A. Fouly, I. A. Alnaser, A. K. Assaifan, H. S. Abdo, *Polymers* **14** (2022) 3321 (https://doi.org/10.3390/polym14163321)
18. S. Ponte, *World Develop.* **30** (2002) 1099 (https://doi.org/10.1016/S0305-750X(02)00032-3)
19. P. Murthy, M. Naidu, *Res. Conser. Recyc.* **66** (2012) 45 (https://doi.org/10.1016/j.resconrec.2012.06.005)
20. L.-L. Kang, Y.-N. Zeng, Y.-T. Wang, J.-G. Li, F.-P. Wang, Y.-J. Wang, Q. Yu, X.-M. Wang, R. Ji, D. Gao, Z. Fang, *J. Water Proc. Eng.* **49** (2022) 103178 (https://doi.org/10.1016/j.jwpe.2022.103178)
21. W. S. Abo El-Yazeed, Y. G. Abou El-eash, L. A. Elatwy, A. I. Ahmed, *RSC Adv.* **10** (2020) 9693 (https://doi.org/10.1039/C9RA10300G)
22. S. Cheng, W. Meng, B. Xing, C. Shi, Q. Wang, D. Xia, Y. Nie, G. Yi, C. Zhang, H. Xia, *J. Clean. Prod.* **403** (2023) 136821 (https://doi.org/10.1016/j.jclepro.2023.136821)
23. M. Ajmal, M. Siddiq, N. Aktas, N. Sahiner, *RSC Adv.* **5** (2015) 43873 (https://doi.org/10.1039/C5RA05785J)
24. S. Zhou, Y. Li, J. Chen, Z. Liu, Z. Wang, P. Na, *RSC Adv.* **4** (2014) 50699 (https://doi.org/10.1039/C4RA08754B)
25. A. Behera, B. Mittu, S. Padhi, N. Patra, J. Singh, in *Multifunctional Hybrid Nanomaterials for Sustainable Agri-Food and Ecosystems*, K. A. Abd-Elsalam, Ed., Elsevier Inc., Amsterdam, 2020, pp. 639-–682 (https://doi.org/10.1016/B978-0-12-821354-4.00025-X)
26. Y. Shen, Y. Xiao, H. Zhang, H. Fan, Y. Li, Z. Yan, WH. Zhang, *Chem. Eng. J.* **477** (2023) 146823 (https://doi.org/10.1016/j.cej.2023.146823)
27. I. A. Ahmed, H. S. Hussein, Z. A. Alothman, A. G. Alanazi, N. S. Alsaiari, A. Khalid, *Polymers* **15** (2023) 1221 (https://doi.org/10.3390/polym15051221)
28. T. T. Hoa, L. V. Dung, L. H. Ha, N. B. Manh, *Vietnam J. Cat. Ads.* **9** (2020) 28 (https://doi.org/10.51316/jca.2020.025)
29. N. H. Son, V. H. Nguyen, T. T. H. Nguyen, N. T. Vu, N. H. Le, *Nano Express* **5** (2024) 025026 (https://doi.org/10.1088/2632-959X/ad5221)
30. Y. Lin, X. Jin, N. I. Khan, G. Owens, Z. Chen, *J. Environ. Manage.* **301** (2022) 113838 (https://doi.org/10.1016/j.jenvman.2021.113838)

31. Z. Wu, X. Su, Z. Lin, G. Owens, Z. Chen, *J. Hazard. Mat.* **379** (2019) 120811 (https://doi.org/10.1016/j.jhazmat.2019.120811)
32. J. Zhou, X. Zhou, K. Yang, Z. Cao, Z. Wang, C. Zhou, S. A. Baig, X. Xu, *J. Hazard. Mat.* **384** (2020) 121229 (https://doi.org/10.1016/j.jhazmat.2019.121229)
33. F. Zhu, S. Ma, T. Liu, X. Deng, *J. Clean. Prod.* **174** (2017) 184 (https://doi.org/10.1016/j.jclepro.2017.10.302)
34. P. Ma, Q. Liu, P. Liu, H. Li, X. Han, L. Liu, W. Zou, *J. Disp. Sci. Technol.* **42** (2021) 1350 (https://doi.org/10.1080/01932691.2020.1764367)
35. T. H. Tran, N. T. Vu, P. H. Thien, N. D. Thanh, P. D. Tuan, *Vietnam J. Sci. Tech.* **55** (2017) 516 (https://doi.org/10.15625/2525-2518/55/4/9016)
36. T. S. Andrade, J. Vakros, D. Mantzavinos, P. Lianos, *Chem. Eng. J. Adv.* **4** (2020) 100061 (https://doi.org/10.1016/j.ceja.2020.100061)
37. Z. Xiong, B Lai, P. Yang, *IOP Conf. Ser.: Earth Environ. Sci.* **167** (2018) 012007 (https://doi.org/10.1088/1755-1315/167/1/012007)
38. S.-S. Zhang, N. Yang, S.-Q. Ni, V. Natarajan, H. A. Ahmad, S. Xu, X. Fang, J. Zhan, *RSC Adv.* **8** (2018) 26469 (https://doi.org/10.1039/C8RA04426K)
39. Y. Chen, X.-F. Zhang, A.-J. Wang, Q.-L. Zhang, H. Huang, J.-J. Feng, *Microchim. Acta* **186** (2019) 660 (https://doi.org/10.1007/s00604-019-3769-y)
40. G. Murtaza, Z. Ahmed, D.-Q. Dai, R. Iqbal, S. Bawazeer, M. Usman, M. Rizwan, J. Iqbal, M. I. Akram, A. S. Althubiani, A. Tariq, I. Ali, *Fron. Environ. Sci.* **10** (2022) 1035865 (https://doi.org/10.3389/fenvs.2022.1035865)
41. P. Sepúlveda, M. A. Rubio, S. E. Baltazar, J. Rojas-Nunez, J. L. Sánchez Llamazares, A. G. Garcia, N. Arancibia-Miranda, *J. Coll. Interf. Sci.* **524** (2018) 177 (https://doi.org/10.1016/j.jcis.2018.03.113)
42. D. O'Carroll, B. Sleep, M. Krol, H. Boparai, C. Kocur, *Adv. Water Res.* **51** (2013) 104 (https://doi.org/10.1016/j.advwatres.2012.02.005)
43. C. Settimi, D. Zingaretti, S. Sanna, I. Verginelli, I. Luisetto, A. Tebano, R. Baciocchi, *Sustainability* **14** (2022) 7760 (https://doi.org/10.3390/su14137760)
44. S. Joshi, M. Sharma, A. Kumari, S. Shrestha, B. Shrestha, *Appl. Sci.* **9** (2019) 3732 (https://doi.org/10.3390/app9183732)
45. N. Mahanta, J. P. Chen, *J. Mat. Chem., A* **1** (2013) 8636 (https://doi.org/10.1039/C3TA10858A)
46. G. P. Gallios, A. K. Tolkou, I. A. Katsoyiannis, K. Stefusova, M. Vaclavikova, E. A. Deliyanni, *Sustainability* **9** (2017) 1684 (https://doi.org/10.3390/su9101684)
47. P. S. Harikumar, T.K. Hridya, *Int. J. Environ. Anal. Chem.***101** (2021) 869 (https://doi.org/10.1080/03067319.2019.1673383).

Journal of the Serbian Chemical Society
JSCS-info@shd.org.rs • www.shd.org.rs/JSCS
J. Serb. Chem. Soc. 91 (2) S64–S65 (2026) *Supplementary material*

SUPPLEMENTARY MATERIAL TO

Composite materials based on biochar from coffee husk origin and nano zero-valent type Fe/Cu: Potential for treatment of water sources contaminated with As(V)

NGOC TOAN VU[1]*, ANH PHU NGUYEN[2], HONG SON NGUYEN[1], VIET ANH PHAM[1], DINH THAO VU[2] and QUANG MINH LE[3]

[1]*Institute of New Technology, 17, Hoang Sam, Nghia Do, Cau Giay, Hanoi, Vietnam,* [2]*Military Technical Academy, 236, Hoang Quoc Viet, Bac Tu Liem, Hanoi, Vietnam and* [3]*Hanoi–Amsterdam High School for the Gifted, 1, Hoang Minh Giam, Trung Hoa, Cau Giay, Hanoi, Vietnam*

J. Serb. Chem. Soc. 91 (2) (2026) 195–212

TABLE S-I. Results of experimental design using Box-Behnken

Run	Factor				As(V) removal efficiency
	X_1: pH	X_2: Time	X_3: CPS/As	X_4: %Metal/C	
	-	min	-	%	H (%)
1	3	100	1000	13	64.93
2	5	140	1250	14	89.04
3	5	60	1250	12	83.29
4	5	140	1250	12	91.64
5	5	140	750	12	88.64
6	5	140	750	14	58.94
7	5	60	750	14	49.55
8	5	60	1250	14	69.46
9	5	60	750	12	48.54
10	7	100	1000	13	81.34
11	7	100	1000	13	81.23
12	7	100	1000	15	64.33
13	7	100	1000	13	76.51
14	7	20	1000	13	37.87
15	7	100	1000	11	75.32
16	7	180	1000	13	89.82
17	7	100	1000	13	76.36
18	7	100	1000	13	76.76
19	7	100	1000	13	81.51
20	7	100	500	13	23.21

* Corresponding author. E-mail: vntoanchem@email.com

21	7	100	1500	13	80.41
22	9	140	1250	12	76.16
23	9	60	750	12	24.64
24	9	140	750	12	48.32
25	9	140	1250	14	70.91
26	9	60	750	14	31.26
27	9	140	750	14	50.34
28	9	60	1250	12	42.91
29	9	60	1250	14	59.5
30	11	100	1000	13	20.12